



## Dissertation

Lin Yang

# Quantification of Brain Oxygen based on Time and Space Optimization of Diffuse Optics: Monte-Carlo Inversion of Infrared Spectroscopy on Phantoms



ISSN 0341-6712  
ISBN 978-3-95606-664-1



# Physikalisch-Technische Bundesanstalt

Optik

PTB-Opt-96

Braunschweig, Januar 2022

Lin Yang

**Quantification of Brain Oxygen based on  
Time and Space Optimization of Diffuse Optics:  
Monte-Carlo Inversion of  
Infrared Spectroscopy on Phantoms**

ISSN 0341-6712

ISBN 978-3-95606-664-1

**Herausgeber:**

Physikalisch-Technische Bundesanstalt

ISNI: 0000 0001 2186 1887

Presse und Öffentlichkeitsarbeit

Bundesallee 100

38116 Braunschweig

Telefon: (05 31) 592-93 21

Telefax: (05 31) 592-92 92

[www.ptb.de](http://www.ptb.de)

Zugl.: Berlin, Technische Universität, Diss.,2022



---

QUANTIFICATION OF BRAIN OXYGEN BASED  
ON TIME AND SPACE OPTIMIZATION OF  
DIFFUSE OPTICS: MONTE-CARLO INVERSION  
OF INFRARED SPECTROSCOPY ON PHANTOMS

---

Lin Yang



OCTOBER, 2021

FACULTY II - MATHEMATICS AND NATURAL SCIENCES  
Technische Universität Berlin



# **Quantification of Brain Oxygen based on Time and Space Optimization of Diffuse Optics: Monte-Carlo Inversion of Infrared Spectroscopy on Phantoms**

vorgelegt von

M. Eng.

Lin Yang

ORCID: 0000-0003-3266-6061

an der Fakultät II - Mathematik und Naturwissenschaften  
der Technischen Universität Berlin  
zur Erlangung des akademischen Grades

Doktor der Ingenieurwissenschaften

Dr.-Ing.

genehmigte Dissertation

Promotionsausschuss:

Vorsitzender: Prof. Dr. Holger Stark

Gutachterin: Prof. Dr. Ulrike Woggon

Gutachter: Prof. Dr. Hamid Dehghani

Gutachter: Prof. Dr. Sergio Fantini

Gutachter: apl. Prof. Dr. Rainer Macdonald

Tag der wissenschaftlichen Aussprache: 21. Dezember 2021

Berlin 2022



# Zusammenfassung

---

---

Optische Spektroskopietechniken werden häufig zur quantitativen Analyse der Stoffzusammensetzung, der physikalischen Eigenschaften und der aus Energie-Materie-Wechselwirkungen hervorgegangenen Phänomene verwendet. Die Nahinfrarot-Absorptionsspektroskopie von menschlichem Gewebe ist von besonderem medizinischem Interesse wegen ihrer Fähigkeit mit Hilfe von Photonen, die nichtinvasiv durch Organe wie das Gehirn oder die Nieren propagiert sind, physiologische und neurologische Informationen selektiv über bestimmte Chromophore im menschlichen Körper zu erfassen. Die Umsetzung dieser Techniken stößt allerdings trotz vieler Forschungsaktivitäten auf diesem Gebiet vor allem aufgrund einer einfachen Tatsache immer noch auf massive Schwierigkeiten: Licht breitet sich in Gewebe nicht geradlinig aus, sondern breitet sich wegen der starken Streuung auf stochastischen Trajektorien aus. Der optische Streueffekt dominiert und ist gewissermaßen verschränkt sich mit der optischen Absorption in diesen Medien. Während sich die meisten quantitativen Analysen auf die Absorptionsspektroskopie stützen, ist die Analyse und Interpretation der somit erzielten Ergebnisse auf Grund dieser Verschränkung mit der Streuung schwierig und dieses Problem bislang nicht zufriedenstellend gelöst. Biomedizinische Anwendungen der Techniken werden durch die Geometrie und Heterogenität von Geweben auf fast jeder Längenskala weiter komplex, was dazu führt, dass die zur Lösung der dahinterstehenden inversen Probleme beim Abrufen der diagnostischen Informationen schlecht gestellt und deren Lösung in der Regel nicht eindeutig ist.

Die vorliegende Dissertation widmet sich der Entflechtung der Effekte von Absorption und Streuung im menschlichen Gehirn und schlägt einen innovativen Ansatz zur Quantifizierung der optischen Absorptions- und Streukoeffizienten mit verbesserter Genauigkeit vor. Insbesondere wird ein neues Konzept zur Integration unterschiedlicher Datentypen aus verschiedenen Messdomänen vorgeschlagen und verifiziert. Der Arbeit liegt eine grundlegende Tatsache zugrunde: Absorption und Streuung sind trotz starker Verschränkung im Kern unabhängig. Und die in den Messungen verschiedener Domänen codierte Komplementarität kann vorteilhaft verwendet werden, um die Wiedergewinnungsgenauigkeit der Unbekannten zu erhöhen und die Komplexität der Inversion zu reduzieren.

Die Arbeit setzt das Konzept im Begriff der räumlich erweiterten Zeitbereichs-Diffusionsoptik um. Durch den Einsatz eines Pikosekunden Pulslasers und einer zeitkorrelierten Einzelphotonenzähltechnik wird der Ansatz an homogenen festen und

zweischichtigen flüssigen Phantomen validiert, die die optischen Eigenschaften des menschlichen Gehirns nachahmen. Monte-Carlo-Simulationen werden angewendet, um den zufälligen Photonentransport in trüben Medien zu imitieren und fließen in die räumlich-zeitliche Optimierung des Inversionsverfahrens ein. Die Schätzgenauigkeit der Absorptions- und Streukoeffizienten wird mit einem Niveau von 5 % nachgewiesen. Das untersuchte und hier vorgestellte Konzept und die Berechnungsmethode haben das Potenzial, die Herausforderungen des inversen Problems in der diffusen Optik wie Lösungsuneindeutigkeit und Tiefenstreuungsneutralität zu überwinden.

Schlagwörter:

Pikosekunden diffuse Optik, Nahinfrarotspektroskopie, Monte-Carlo-Gehirnsimulation, räumlich-zeitliche Optimierung, zeitkorrelierte Einzelphotonenzählung.

# Abstract

---

---

Optical spectroscopy techniques are frequently used for the quantitative analysis of substance composition, physical properties, and the phenomena risen from energy-matter interactions. Near-infrared absorption spectroscopy of human tissues is particularly of medical interests for its ability to selectively acquire physiological and neurological information of certain chromophores in the human body, with the help of photons that are non-invasively propagated through organs such as brain or kidney. The implementation of these techniques, despite many research activities in this area, still encounters massive difficulties primarily due to one simple fact: Light no longer travels in a straight line in tissues but rather spreads on stochastic trajectories due to the strong scattering. The optical scattering effect dominates in these media and to some extent is entangled with the optical absorption. While the optical absorption spectroscopy is what most quantitative analyses rely on, the interpretation and analysis of the results are difficult due to this entanglement with scattering and this problem has not yet been satisfactorily solved. Biomedical applications of the techniques are further complex by the geometry and heterogeneity of tissues at almost every length scale, which results in the ill-posedness of solving the underlying inverse problem and thereafter usually the solution's non-uniqueness when retrieving the diagnostical information.

The present thesis is devoted to disentangle the effects from absorption and scattering in human brain and purpose an innovative approach on quantifying the optical absorption and scattering coefficients with improved accuracy. Especially, a new concept of integrating disparate data types from various measurement domains is proposed and verified. The work is based on a fundamental fact: The absorption and scattering, despite heavily entangled, are essentially independent. And the complementarity encoded in the measurements of different domains can be advantageously used to increase the retrieval accuracy of the unknowns and reduce the complexity of the inversion.

The thesis realizes the concept in the term of spatial-enhanced time domain diffuse optics. By deploying picosecond pulse laser and time-correlated single photon counting technique, the approach is validated on homogeneous solid and two-layered liquid phantoms mimicking human brain's optical properties. Monte-Carlo simulations are applied to imitate photon random transport in turbid media and are incorporated into the spatio-temporal optimization of the inversion process. The estimation accuracy of absorption and scattering coefficients is demonstrated at level of 5%. The examined and presented concept and computational method

have the potential to overcome the challenges of the inverse problem in diffuse optics such as solution's non-uniqueness and deep scattering neutrality.

Keywords:

picosecond diffuse optics, Near infrared spectroscopy, Monte-Carlo brain simulation, Spatio-temporal optimization, time-correlated single photon counting

In memory of my grandmother 1936 – 2021

纪念我的姥姥 1936 - 2021



# Acknowledgements

---

---

The successful completion of this thesis would not have been possible without professional and personal support from colleagues, friends and family.

I would like to first express my deep gratitude to my supervisor Prof. Dr. Rainer Macdonald for his generous support and continuous guide in these years. Thank him for giving me the opportunity and freedom in working in his department and choosing the research direction.

Warmest thanks also to my mentor, Dr. Heidrun Wabnitz. Studying and living in Germany is like an adventure to me, and without her kind cares I would probably not survive. Her critical suggestions to me also lead to a lot of fruitful inspirations in my study.

I am also very grateful for the supports from Dr. Dirk Grosenick, for his profound knowledge and research skills. His rigorous research style and discipline impressed me as a model. Dr. Thomas Gladytz for his always-optimistic attitude, insight and helps to me also deserve a big thanks. I would also like to express my appreciation to many other colleagues in PTB.

I had the fortune to study in the EU Marie-Curie scholarship project, where I have great pleasure to collaborate with the great scientists and researchers in the diffuse optics community around the world. I had many great times with other PhD students of the project during the collaborations and the spare time.

In the end, I would like to deliver my deepest gratitude to my friends and family. Without their unconditional love and enormous support over the years I would have never been able to even start my doctoral study. Their trust and encouragement always empower me along this path.

Lin Yang  
2021.9, Berlin



# Table of Content

---

---

<b>Zusammenfassung</b> .....	<b>I</b>
<b>Abstract</b> .....	<b>III</b>
<b>Acknowledgements</b> .....	<b>VII</b>
<b>Table of Content</b> .....	<b>IX</b>
<b>Abbreviations</b> .....	<b>XIII</b>
<b>Symbols</b> .....	<b>XVII</b>
<b>1 Introduction</b> .....	<b>1</b>
1.1 Project background and significance.....	1
1.2 Challenges and recent advances .....	2
1.3 Thesis aim and structure .....	3
<b>2 Principles and models of Diffuse Optics</b> .....	<b>7</b>
2.1 Theoretical fundamentals .....	7
2.2 The optical properties of biological tissues and brain oxygenation .....	8
2.3 Forward and inverse problems in diffuse optics.....	13
2.4 Monte-Carlo modelling of light transport in tissues.....	19
<b>3 Method and instrumentation for tissue diagnosis</b> .....	<b>25</b>
3.1 Modalities of NIRS system .....	25
3.2 Integration of time and space domain NIRS .....	30
3.3 Instrumentation.....	40
3.4 Phantoms .....	45
<b>4 Space-enhanced time-domain diffuse optics in homogeneous structures</b> .....	<b>49</b>
4.1 Abstract.....	50
4.2 Introduction .....	50
4.3 Theory .....	52
4.3.1 Positive correlation in time domain.....	52
4.3.2 Negative correlation in space domain.....	53
4.3.3 Spatially enhanced time domain NIRS.....	54
4.4 Methods and materials.....	58
4.4.1 Phantoms .....	58
4.4.2 Experimental setup .....	58
4.4.3 Monte-Carlo simulations and forward model.....	61
4.4.4 $\chi^2$ objective function and inverse models .....	61

4.5 Results .....	62
4.6 Analysis of uncertainty, robustness, and uniqueness .....	66
4.6.1 Uncertainty .....	66
4.6.2 Uniqueness.....	67
4.6.3 Stability.....	68
4.7 Conclusion.....	69
4.8 Funding and Acknowledgement.....	70
<b>5 Space-enhanced time-domain diffuse optics in layered structures</b> .....	<b>71</b>
5.1 Abstract.....	72
5.2 Introduction .....	72
5.3 Concept of space-enhanced time domain method .....	74
5.4 Methods and materials.....	77
5.4.1 Experimental setup .....	77
5.4.2 Preparation and characterization of the layered phantom.....	79
5.4.3 Monte-Carlo simulations and forward model.....	81
5.4.4 Measurement method and inverse procedure .....	82
5.5 Results .....	84
5.5.1 Measured data and results of the first layer .....	85
5.5.2 Results of the second layer based on different methods.....	87
5.6 Performance Metrics .....	91
5.7 Discussion.....	93
5.8 Conclusion.....	96
<b>6 Current Limitations.....</b>	<b>97</b>
6.1 Methodological limitations.....	97
6.2 Instrumental limitations.....	98
<b>7 Conclusion and Prospect.....</b>	<b>99</b>
<b>List of Publications .....</b>	<b>103</b>
<b>Reference .....</b>	<b>107</b>





# Abbreviations

---

---

ADC	Analog-to-digital converter
AOTF	Acousto-optic tunable filter
AR	Albedo-rejection
ASPR	Absorption-scattering pathlength rejection
AW	Albedo-weight
CFD	Constant-fraction discriminator
CSF	Cerebrospinal fluid
CUDA	Compute unified device architecture
CW	Continuous wave
DE	Diffusion equation
DNL	Differential nonlinearity
DOT	Diffuse optical tomography
DTOF	Distributions of time-of-flight
EBC	Extrapolated boundary condition
EEG	Electroencephalogram
FD	Frequency domain
FEM	Finite volume method
fNIRS	functional Near infrared spectroscopy
FWHM	Full width at half maximum
GLF	Generalized Lagrangian Function
Hb	deoxyhemoglobin
HbO <sub>2</sub>	oxyhemoglobin
HPM	Hybrid Photomultiplier

IRF	Instrument response function
LUT	Look-up table
MC	Monte-Carlo
MPP	Mean partial pathlength
MRI	Magnetic resonance imaging
NA	Numerical aperture
NIRS	Near infrared spectroscopy
OCT	Optical coherence tomography
PDMS	Polydimethylsiloxane
PMT	Photomultiplier tube
RTE	Radiative transfer equation
SD	Space domain
SeTD	Space-enhanced time domain
SiPM	Silicon photomultiplier
SLM	Spatial light modulator
SPAD	Single-photon avalanche diode
SRAC	Space-resolved amplitude curve
SRS	Spatially resolved spectroscopy
ST	Spatio-temporal
TAC	Time-to-amplitude converter
TCSPC	Time-correlated single-photon counting
TD	Time domain
TDC	Time-to-digital converter
TTS	Transit time spread
VCSEL	Vertical cavity surface emitting laser

ZBC

Zero boundary condition



# Symbols

---

---

$\mu_a$	Optical absorption coefficient
$\mu_s$	Optical scattering coefficient
$\mu'_s$	Reduced Optical scattering coefficient
$\mu_{eff}$	Effective attenuation coefficient
$c$	Speed of light
$cHb$	Concentration of deoxyhemoglobin
$cHbO_2$	Concentration of oxyhemoglobin
$cHbT$	Concentration of total hemoglobins
$D$	Optical diffusion coefficient
$\mathcal{F}$	Forward model function
$g$	Anisotropy factor
$J$	Radiant flux
$R$	Optical reflectance
$SO_2$	Oxygen saturation
$V$	Variance, second central moment
$\kappa$	Molar extinction coefficient (absorptivity)
$\lambda$	Optical wavelength
$\rho$	Source-detector distance
$\sigma$	Standard deviation,
$\phi$	Photon fluence rate
$\Phi$	Photon density function
$\chi^2$	Residual Statistic of chi-squared distribution



# 1

## Introduction

This thesis is aiming to improve quantitative analyses of spectroscopy in highly scattering media like tissues, and particularly presenting an innovative concept on disentangling optical absorption and scattering effects in near infrared spectroscopy (NIRS) of the brain. The thesis will first describe the scientific and technical contexts that connects this work, and then provide a detailed introduction and description of the newly developed concept. The proof of principles and validations of the new approach are thereafter given by the experimental demonstrations on tissue-mimicking phantoms. Further discussions, conclusions and outlooks are shown in the end.

### 1.1 Project background and significance

In the last decades, many important discoveries in physics have been benefitting to the medical community, such as ultrasound, X-rays, magnetic resonance imaging (MRI), and positron emission tomography. Particularly in recent, optical physics has found very ubiquitous biomedical applications owing to the high accuracy, non-invasiveness, and high chromophores-selectivity after the invention of laser. Nowadays, optical methods are applied to many clinical treatments and therapeutical applications such as retina coagulation, photodynamic therapy, disruption of tumours, and laser refractive surgery. Meanwhile besides clinical treatments, optical methods are more increasingly applied to clinical diagnosis. Thanks to the extraordinary features of light and photons, optical endoscopes, optical coherence tomography (OCT) [1], photoacoustic imaging [2], diffuse correlation spectroscopy (DCS) [3], confocal microscopy [4], and diffuse optical tomography (DOT) [5,6] are all emerging in recent decades and are still rapidly developing. By light / photons, it is not only possible to obtain structural information in tissues, but also feasible to obtain functional signals that may be physiologically essential.

The human brain plays the central role of the nervous system functions; and as the most complicated organ, the neuronal activities and physiological mechanisms within the brain are

still largely open to further research. The outer cortical surfaces of the brain, where physical feelings and sensations generate, could usually be detected by electroencephalogram (EEG) and many other techniques. While many more physiologically critical mechanisms, such as addiction, anxiety, consciousness, depression, insomnia, memory loss, and some diseases like strokes and encephalopathy, are originated from deep brain regions. The light in the near-infrared spectrum can penetrate through skin and skull, with the high sensitivity to detect changes in optical properties arisen from physiological variations in cortical brain regions, and then bring relevant physiological information back. Hereby, as a completely non-invasive, chromophore-selective, and portable tool, light is ideal and unique for plenty of potential discoveries and explorations about brain in the future [7]. Currently, a remarkable new development in the field is that an increasingly sophisticated connection is being created between brain and computer by neurophotonics [8], through detecting and analyzing the absolute oxygen saturation and the changes in the levels of hemoglobins and other chromophores of brain.

If it is true to say that the techniques highly developed in the last century, representing by ultrasound, X-rays and MRI, opened up the new era of modern medical physics and led us start to examine corporeal structures of human in a physically straightforward way; then it is also not exaggerated to say that the technologies based on optical physics, are imminently paving the way to help us get more insight into incorporeal and intangible features of human, such as our emotion, cogitation and memories. Eventually, light may introduce a new way for us to understand our feelings, our thoughts, and finally our own.

## **1.2 Challenges and recent advances**

To apply light on investigating brain, many fundamental challenges remain to be overcome. First, the reliable quantification of brain chromophores depends on the determination of optical absorption, which is heavily hampered by the optical scattering. Unlike x-ray CT wherein scattering is neglectable, it is almost inevitable to quantify optical absorption and scattering together. Many efforts and progresses were poured into modelling complex diffusive propagation of light, in analytical or computational methods, and by deterministic or stochastic ideology [9]. But a method which can simultaneously retrieve absolute quantities of optical absorption and scattering with high accuracy still remains as a challenge.

Secondly, the basic light-matter interaction involves in solving the inverse problem of diffuse optics. Such inverse problem in diffuse optics is ill-posed and nonlinear, which means that there is no unique solution for the inversion and the results do not continuously depend on

measured information [10]. Plenty of research have focused on looking for the solutions based on finite element methods to avoid the troublesome raised from the intrinsic factors of the problem and successfully achieved fruitful outcomes. Nevertheless, by encountering those intrinsic factors and acknowledging the basics of light-matter interaction, such as the relation of effects originated from absorption and scattering, an innovative idea that could effectively circumvent the limitations of the approaches on solving the inverse problem is in need

The third challenge is about the brain geometry's complexity for modelling light propagation. The information from superficial compartments of brain will always mask the brain activations from deep brain regions. Separating superficial and cortical signals is critical on the result accuracy. The assumption of homogeneity has been adopted by many research groups and succeed in infant and small animal studies. On the other hand, many others applied anatomical structures from MRI with the hope of improving spatial resolution. Both two courses have reported numerous studies and applications, with the different weightings between accuracy and computation capacity [11,12]. In present, an intermediate trade-off model that is versatile and more computationally effective, is keen to be explored for the real-life implementation of diffuse optics.

Finally, and more practically, along with the development of many detection techniques in diffuse optics such as continuous-wave, time-domain and frequency-domain [13], it is now a challenge about concurrent modalities in diffuse optics as well. To achieve a better retrieval performance for the absolute quantification of optical properties, the integration of different modalities and the optimization of information from different dimensions is important. Many studies have been developing the approaches on this aspect. Moreover, a comprehensive computation method (such as Monte-Carlo method) which is suitable to the data acquisition of all modalities would be practically useful. From a higher perspective, the effective methods about quantification of brain optical properties based on multiple-domain optimization of diffuse optical information need to be cultivated.

### **1.3 Thesis aim and structure**

Upon aforementioned challenges and recent advances, the methods and approaches developed in the frame of this thesis are dedicated to overcoming the challenging difficulties and achieve the aims which might benefit to the implementations of diffuse optics, as follows:

- 1) To simultaneously retrieve the absolute quantities of optical absorption and optical scattering in homogenous and layered turbid media with high accuracy.

- 2) To investigate the complementarity of the observations of photon diffusion in different domains and study on solving the inverse problem of diffuse optics in a comprehensive way.
- 3) To propose an innovative concept that can integrate information from photon's diffuse propagation in both time domain and space domain for a better retrieval of optical properties.
- 4) To provide a new experimental approach which applies the space-enhanced time-domain diffuse optics methodology that combining time-domain and continuous-wave modalities.

In this thesis, Chapter 1 introduces the background and significance of the project and is a present overlook of the investigated field. In Chapter 2, a general review is given for the theoretical fundamentals and models used in diffuse optics, especially for the applications studying on optical properties of biological tissues and brain oxygenation. The forward and inverse models in diffuse optics are systemically considered from a mathematical perspective. Furthermore, the general idea and implementation of the Monte-Carlo method on modelling light transport in tissues are briefly presented as well.

Chapter 3 focuses the method and instrumentation for tissue diagnosis based on diffuse optics. The state-of-art modalities of near infrared spectroscopy systems are introduced and compared. A new method from this thesis, namely space-enhanced time-domain diffuse optics, which integrates time domain and space domain modalities of near infrared spectroscopy system, is discussed in detail. The physical instrumentation used in experiments, including light sources, detectors, timing electronics, and light guides are briefly presented in the scope of their applications and limitations. Finally, the phantoms used in this project are discussed as well.

Chapter 4 and 5 serve as the main body of the thesis. Two previously published articles are contained and typesetted to form and fuse into the thesis as the physical application and experimental demonstration of the space-enhanced time-domain diffuse optics in homogenous and two-layered structures. The concept, practical methods, phantom materials, and experimental setups are presented individually. The Monte-Carlo simulations and forward models used in these two chapters are significantly different and contain different levels of complexity. In addition, the complementary correlations in space domain and time domain are discovered in chapter 4. The "deep scattering neutrality" is introduced in chapter 5 and the solution from space-enhanced time-domain diffuse optics is given there as well. The uncertainty, uniqueness, and stability, as well as the accuracy, error, and linearity are investigated and discussed in both chapters too.

Chapter 6 discusses the current limitations of the new method from both methodological and experimental concerns, and proposes the potential solutions. Chapter 7 summarizes all conclusions of the thesis and provides an outlook of the further developments and applications of the new method.



# 2

## Principles and models of Diffuse Optics

In diffuse optics studies, two major optical phenomena dominate the light propagation, i.e., absorption and scattering. Although the physical mechanisms of light absorption and light elastic scattering are already well explained by Stimulated Emission theory from *Albert Einstein*, and by Mie Scattering theory from *Gustav Mie*, the predictable models of light propagation and accurate optical parameters recovery which are directly based on these general theories are usually difficult in practice or even computationally impossible. Biomedical applications of light propagation are further complicated due to the structural complexity and heterogeneity of biological tissues. In this chapter, the theoretical fundamentals of diffuse light propagation are briefly described in 2.1. The optical properties of biological tissues and diffuse optics on brain oxygenation are given in 2.2. The forward modelling methods of diffuse light propagation, and the inverse solutions of recovering optical properties from boundary measurements of turbid media are discussed in 2.3. The computational methods focusing on Monte-Carlo simulations are discussed in 2.4.

### 2.1 Theoretical fundamentals

#### Light absorption

When light is irradiated on the turbid media, photons penetrating the media will be absorbed and scattered. Optical absorption of the media can be quantitated by the absorption coefficient  $\mu_a$ , which is defined by the probability of a photon being absorbed per unit pathlength  $\mu_a = -\partial I / (I_0 L)$  where  $L$  is the optical pathlength. The reciprocal of  $\mu_a$  also yields the mean pathlength before a group of photons are totally absorbed in the media. The famous *Beer-Lambert* law [14,15] can be derived by the definition of  $\mu_a$ :

$$I = I_0 \exp(-\mu_a L) \quad (2.1)$$

Where  $I_0$  and  $I$  are the incident and transmitted intensity. The light energy transfer to the host media during the absorption process.

## Light scattering

Similarly, the probability that a photon is scattered per unit pathlength defines the scattering coefficient  $\mu_s$ . In the context of the present thesis work, we focus on elastic scattering where the photon energy remains conserved but the momentum (i.e., directions) of the photons are altered by scattering. The directions of the scattered photons, or the angular dependence of scattering, is described by the phase function  $p(\theta)$ , meaning the probability of a photon's trajectory turned from  $0^\circ$  (original direction) to  $\theta^\circ$  after one scattering event. The amount of forward direction retained after one scattering event can be described by the dimensionless anisotropy factor  $g$ :

$$g = \langle \cos \theta \rangle = \int_0^\pi p(\theta) \cos \theta 2\pi \sin \theta d\theta \quad (2.2)$$

Photons will be scattered to all possible directions with equal probability if  $g = 0$ , corresponding to so-called isotropic scattering, and larger  $g$  values indicate the more dominant forward scattering. In the Mie scattering regime where the sizes of large particles are comparable or larger than optical wavelength,  $g$  tends to be always larger than 0, indicating anisotropic and more or less forward scattering, which is usually assumed to be the dominant case in biological tissues.

While it is difficult to retrieve  $g$  value by calculating Eq. (2.2), one approximating function has proven to be useful in biological tissues, as described by *Henye* and *Greenstein* [16]:

$$p(\theta) = \frac{1}{4\pi} \frac{1 - g^2}{(1 + g^2 - 2g \cos \theta)^{3/2}} \quad (2.3)$$

With the definition of  $g$ , one can get the reduced scattering coefficient  $\mu'_s$  as:

$$\mu'_s = \mu_s(1 - g) \quad (2.4)$$

$\mu'_s$  corresponds to the equivalent rate of isotropic scattering. Its reciprocal,  $1/\mu'_s$ , is referred to the photon transport mean free pathlength [17].

Given absorption coefficient  $\mu_a$  and reduced scattering coefficient  $\mu'_s$ , we further have the extinction coefficient  $\mu_t = \mu_a + \mu'_s$ , and effective attenuation coefficient  $\mu_{eff} = [3\mu_a(\mu_a + \mu'_s)]^{1/2}$ , which will be given more descriptions in chapter 3.

## 2.2 The optical properties of biological tissues and brain oxygenation

## The optical properties of tissue components

The absorption coefficient  $\mu_a$  is closely related to endogenous and exogenous chromophores in biological tissues, since it can be expressed by sum of the product of constant  $\ln 10$ , the molar extinction coefficient (absorptivity)  $\kappa$ , and the amount concentration  $c$  of various chromophores in tissues,  $\mu_a = \sum(\ln 10 \kappa_i c_i)$ , where  $c_i$  and  $\kappa_i$  are the amount concentration and the molar extinction coefficient of chromophore  $i$ , respectively. The major endogenous chromophores in biological tissues are water, blood (oxyhemoglobin  $\text{HbO}_2$ , and deoxyhemoglobin  $\text{Hb}$ ), lipid(fat), and Melanin. The absorption spectra for different tissue components can vary a lot, which in turn provide special advantages regarding the chromophore-selectivity to diffuse optics. As Jobsis first demonstrated in 1977 [18], a significant amount of light radiation can effectively penetrate through biological tissues over longer distances in the near infrared spectral range compared to all other ranges, *i.e.*, the “near-infrared optical window” (wavelength from 650 nm to 1000 nm). The intense absorption bands of blood below 650 nm and the increasing water absorption above 1000 nm jointly create the unique fact that biological tissue is comparatively transparent in this window. Absorption spectra of tissue components are shown in Fig. 2.1. More detailed data of tissue components’ absorption spectra can be found in many literatures [19,20].

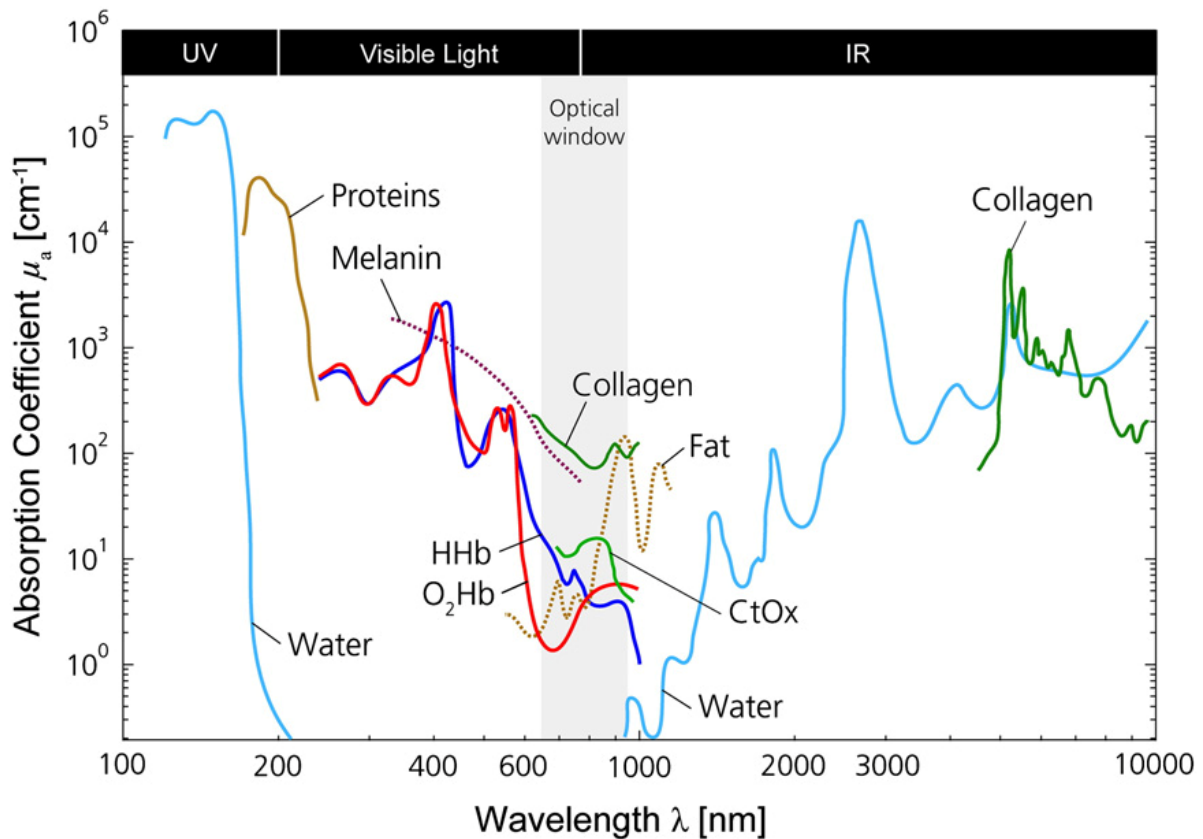


Fig. 2.1. Absorption spectra of different tissue components: Hb, HbO<sub>2</sub>, H<sub>2</sub>O, and Lipid, and the therapeutic window in NIR range [21] (Reprinted from *Neuroimage* (2014): 6-27, with permission from Elsevier).

On the other hand, different from absorption spectrum which are quite specific among chromophores, the wavelength dependency of the reduced scattering coefficients generally follows a so-called power law, given by:

$$\mu'_s(\lambda) = a \left( \frac{\lambda}{\lambda_0} \right)^{-b} \quad (2.5)$$

where  $\lambda_0$  is the reference wavelength and the parameters  $a$  and  $b$  can be experimentally determined for individual tissue components. Eq. (2.5) delivers the important message that the light scattering in biological tissues will always reduce alongside with the increase of wavelength. More detailed spectra data of tissue components' scattering (and anisotropy factor  $g$ ) can be found in literatures [19,20].

Typically,  $\mu'_s$  is much larger than  $\mu_a$  in near infrared window for most biological tissues, implying that the scattering effect is much stronger than absorption effect on photons in tissues. In the other words, the propagation of near infrared light in tissues is strongly dominated by scattering, and thus the direct reconstruction of absorption, which is of more biomedical interest, is heavily hampered. The optical image of the distribution and concentration of chromophores inside tissue will be blurred by scattering. Therefore, unlike some other non-invasive medical imaging techniques (x-ray CT, ultrasonography, etc.) which have strong penetration ability, NIRS diffuse optics must simultaneously consider and analyse both, scattering and absorption effects during the reconstruction of optical properties. Furthermore, the extinction coefficient is quite large due to strong scattering and usually one has to deal with low-photon count detection for the instrumentations.

A few recent studies show that the “second NIR window” ( $1100 \text{ nm} < \lambda < 1350 \text{ nm}$ ) [22] and the “third NIR window” ( $1600 \text{ nm} < \lambda < 1850 \text{ nm}$ ) [23] might be helpful to obtain deeper penetration length and clearer optical images due to a reduction in scattering as implied by Eq. (2.5). Advances on new sensitive photodetectors and intense laser sources on these new NIR ranges, as well as the methods to overcome the stronger water absorption, are needed, before further investigations and explorations in these new windows could be performed.

## **Head anatomy and brain optical properties**

The human brain is the focus of many biomedical NIRS studies because of its central role of the nervous system. It is also an ideal object for applications of diffuse optics because of the

non-invasiveness, sensitive chromophore-selectivity, and high temporal resolution of NIRS techniques [24–26]. However, the anatomy of the head and structure of the tissue needs to be known before applying diffuse optics, and to adapt an appropriate geometrical model for the reconstruction of optical properties distribution.

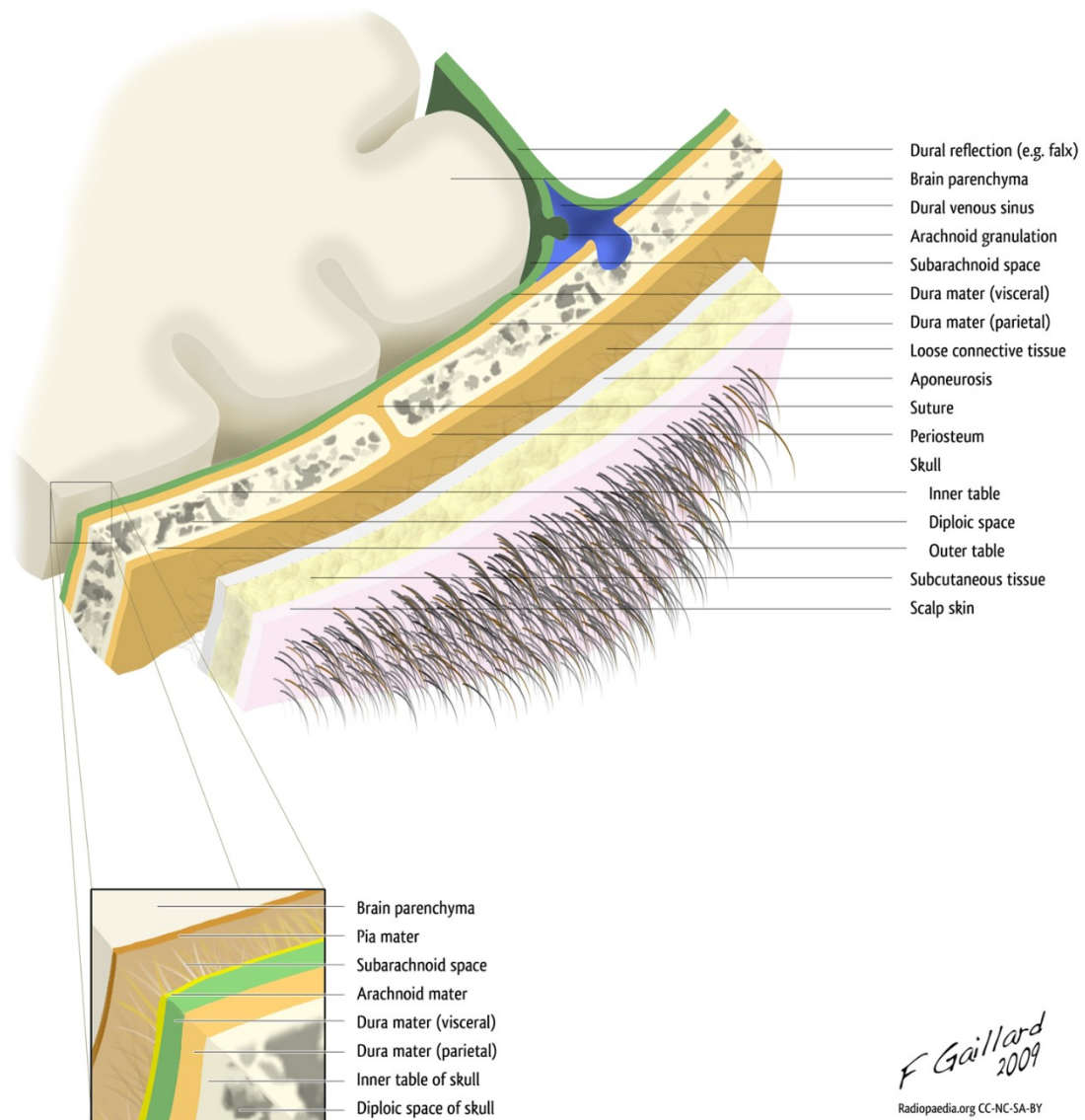


Fig. 2.2. Cross section of a human scalp and skull [27] (by Frank Gaillard, licensed under CC BY-SA-NC).

More or less simplified, the brain is constituted by a deep region of white matter and covered by a layer of grey matter, and then surrounded by the meninges (dura mater, arachnoid mater, and pia mater) including a thin layer of cerebrospinal fluid (CSF) within, a bone layer (skull), and a derma layer (scalp). A cross section of the brain and its surrounding tissue is shown in Fig. 2.2. The useful NIRS information is encoded by photons which have travelled through the head and interacted with cortex of the brain, and are finally detected by the photosensor above the scalp skin. All the tissue compartments shown in Fig. 2.2 can be

penetrated by near infrared light, while the heterogeneity of head structure strongly affects the light propagation. The skull is made up from 22 cancellous bones that are less dense than compact bones and more vascular. The total absorption and scattering of it is like those of its surrounding tissue [28]. From an optical point of view, the CSF layer could rise “light guiding” effect due to its relatively low scattering and could interrupt the “normal” light scattering due to its reticular structure formed by arachnoids.

A lot of studies have dedicated into looking for an appropriate physical model of the brain to simulate photons travelling in it. The assumption of homogenous models for the brain could heavily impede the robust and reproducible reconstruction of optical properties in adult brain, despite their feasibility in neonate and small animal studies [29,30]. On the other hand, applying real detailed anatomical structures of brain (usually from MRI) could also not be necessary and even have a worse performance on recovering optical properties sometimes [11,12] compared to much simplified models. In a good approximation, the geometry of adult brain can be assumed as layered structures, which is advantageous to simplify the light propagation modelling and maintain a high accuracy at the same time.

Only until recently [31], the overview picture of *in vivo* optical properties ( $\mu_a$  and  $\mu'_s$ ) in NIR for the adult human brain is reported under the investigation of intra- and inter-subject with cross-validation with different methodologies. It is found that in a layered geometry of an adult head, the upper layer (including scalp and skull) usually has the lower light absorption (e.g.,  $0.07 \text{ cm}^{-1}$  @830 nm) than the deeper layer (including the meninges and grey and white matter, e.g.,  $0.15 \text{ cm}^{-1}$  @830 nm). And the upper layer has the higher scattering (e.g.,  $8 - 16 \text{ cm}^{-1}$  @830 nm) than the deeper layer (e.g.,  $4 - 10 \text{ cm}^{-1}$  @830 nm). The  $\mu_a$  and  $\mu'_s$  values vary a lot in different subjects and in different regions of brain. But two features are certain:

- (1) The scattering effect is two orders of magnitudes stronger than the absorption effect in NIR for all compartments of adult brain.
- (2) Brain optical properties are sealed by the upper tissues; detectable photons are scarce if not scattered out by upper tissues, absorbed by brain, or exiting from other places of head not covered by detector.

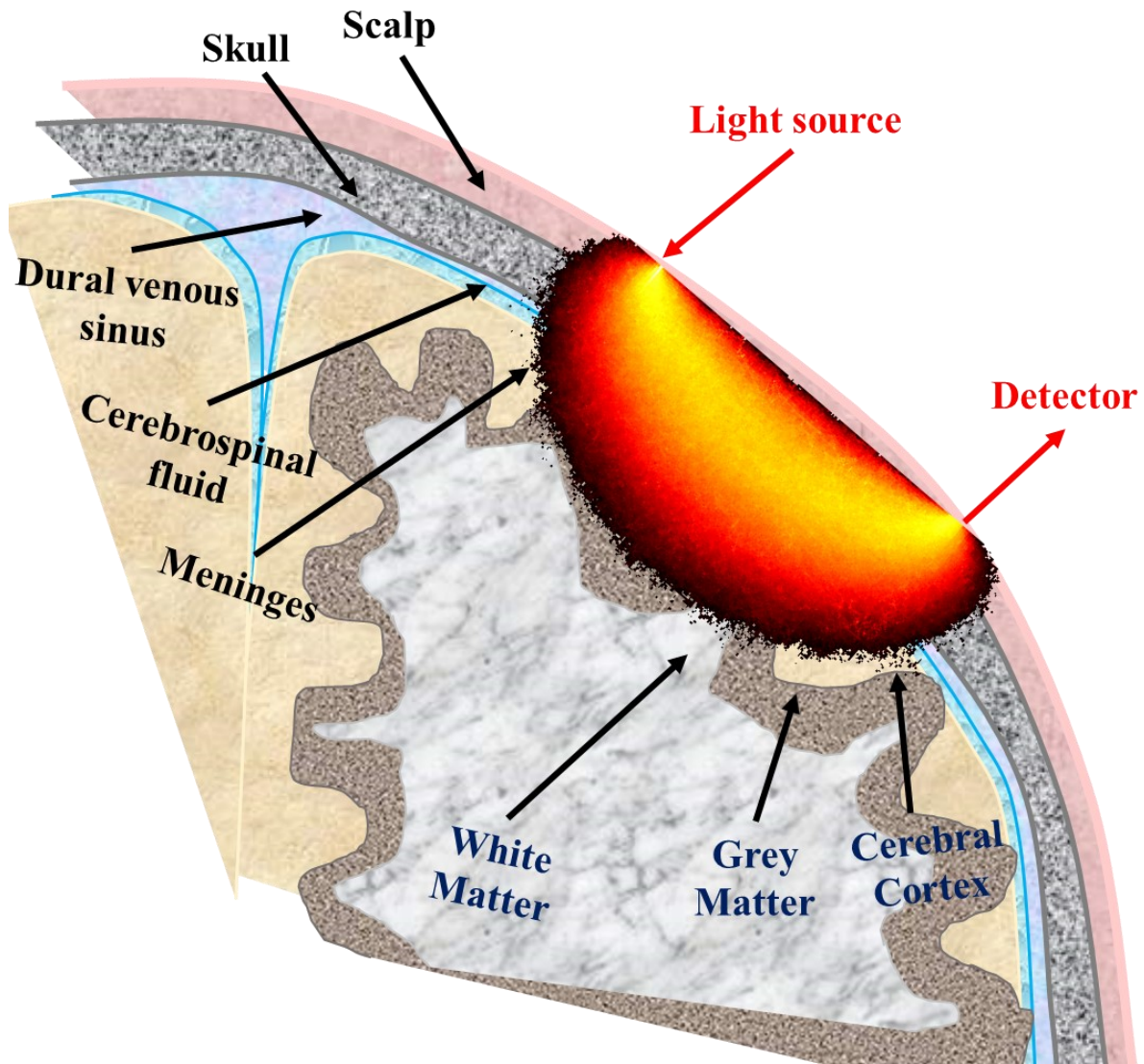


Fig. 2.3: NIR light travelling in the layered geometry of human brain; the “banana shape” of light trajectory.

Brain oxygen saturation  $SO_2$  is defined by the ratio of  $HbO_2$  concentration and total haemoglobin concentration,  $SO_2 = cHbO_2 / (cHbO_2 + cHb)$ , and therefore directly related to absolute quantities of  $\mu_a$  in brain.  $cHb$  is the absolute concentration of deoxyhemoglobin;  $cHbO_2$  is the absolute concentration of oxyhemoglobin; and  $cHbT$  sometimes refers to the absolute concentration of total hemoglobin, i.e.,  $cHbO_2 + cHb$ . As a highly clinically relevant parameter, the reliable assessment of  $SO_2$  is still challenging [32]. Tremendous efforts, as for establishing and solving the forward and inverse problems in diffuse optics, have been devoted to the accurate assessment.

### 2.3 Forward and inverse problems in diffuse optics

In diffuse optics, the mathematical formulation of modelling and predicting light propagation is called forward problem. And the reconstruction of the optical properties of the media from boundary observations is called inverse problem.

### Forward problem

Light propagation in turbid media abides by Maxwell's equations as electromagnetic wave. However, Computation of wave theory is not feasible in turbid media quickly after a few scattering events. The most straight-forward physical model is formulated in terms of the conservation law under the principle of *Boltzmann transport equation*, i.e., accounting for gains and losses of photons in a small volume. The more commonly used term, radiative transfer equation (RTE), is formulated by focusing on the photon density function  $\phi(\mathbf{r}, \mathbf{s}, t)$  defined as the number of photons per unit volume at position  $\mathbf{r}$  propagating in direction  $\mathbf{s}$  at time  $t$ . The RTE in the integro-differential form is written as:

$$\left( \frac{1}{c} \frac{\partial}{\partial t} + \mathbf{s} \cdot \nabla + (\mu_a + \mu_s) \right) \phi = q + \mu_s \int_{4\pi} p(\mathbf{s}', \mathbf{s}) \phi d\Omega' \quad (2.6)$$

The right side of the equation stands for the photon gains:  $q = q(\mathbf{r}, \mathbf{s}, t)$  is the light source density in the small volume, and the integration term is the photon gain due to the scattered photons from all possible direction  $\mathbf{s}'$  into the direction  $\mathbf{s}$ . On the left side of the equation,  $(\mu_a + \mu_s)\phi$  is the photon loss due to the absorption and scattering in the small volume, and the  $\mathbf{s} \cdot \nabla \phi$  term is the photon loss due to non-interactive photon transporting at direction  $\mathbf{s}$ . The  $\partial\phi/c\partial t$  term is then the time derivative of  $\phi$  coming out from the small volume, given  $c$  is the speed of the light in the medium  $\Omega$ . Eq. (6) can also be utilized for light energy radiance  $L = h\nu c\phi(\mathbf{r}, \mathbf{s}, t)$ , for the perspective of energy instead of photons. Note that the RTE normally does not consider many other phenomena such as polarization and fluorescence, but can be extended to include them [33].

Except for a very few situations with simple geometric structures and optical properties, the RTE is extremely hard to solve analytically. Given various geometries, solving RTE usually consider different assumptions, approximations, and boundary conditions. Therefore, the forward modelling of light propagation remains to be a problem. As a focus of diffuse optics, the field of RTE forward modelling has grown out of all proportion and many of these approaches overlap or cooperate with each other. It is almost impossible to summarize all the approaches. Nevertheless, in this chapter the approaches that have proven to be enduring and representative are enumerated, as an attempt of a brief overview.

**Table 1.1. The methods for Light propagation modelling based on RTE**

Concept Category	Methods	Representative references
Expansion Methods	$P_1$ / DE $P_3$ $P_N$	Patterson <i>et al.</i> , 1989 [34] Liemert <i>et al.</i> , 2014 [35] Phillips <i>et al.</i> , 2009 [36]
Discrete Methods	Kubelka-Munk Adding-doubling Discrete ordinates	Sandoval <i>et al.</i> , 2014 [37] Prahl <i>et al.</i> , 1993 [38] Klose <i>et al.</i> , 1999 [39]
Stochastic Method	Monte-Carlo	Wang <i>et al.</i> , 1995 [40] Boas <i>et al.</i> , 2002 [41] Fang <i>et al.</i> , 2010 [42]
Finite Methods	Finite difference method Finite element method Boundary element method	Abdouljev <i>et al.</i> , 2005 [43] Arridge <i>et al.</i> , 1993 [44] Srinivasan <i>et al.</i> , 2007 [45]
Semi-empirical / Hybrid Methods		Wilson <i>et al.</i> , 2009 [46] Tualle <i>et al.</i> , 2004 [47] Paasschens, 1997 [48]

In summary, the expansion methods develop the RTE terms into spherical harmonics to separate the position and directional variables, and then express the equation under  $P_N$  approximation with a certain accuracy applied. The discrete methods usually apply to special structure (e.g., Kubelka-Munk to slabs), or to isotropic scattering (Discrete ordinates), or require measuring the total transmission and reflection (Adding-doubling). The stochastic method is suitable to complex geometries while is also the most computationally expensive, as well as the finite methods. Semi-empirical methods are useful to many special situations rather than the universal modelling methods.

Recently, a group has presented that the exact solutions of the RTE can be solved for the infinite [49], semi-infinite [50], and laterally infinite layered media [51], with the anisotropic scattering. Moreover, the analytical description of TD perturbation forward solver has also greatly improved for photon migration with large highly absorbing objects [52].

There are also numerous hybrid methods which combine methods with different concepts. For example, “Toast++” developed by Schweiger and Arridge [53] combines FEM with DE; as well as “NIRFAST” developed by Dehghani [54]. “MCX” developed by Fang combines FEM with Monte-Carlo method [55]. Generally, analytic methods to the RTE can also be easily integrated into numerical method to provide solutions of Green’s function, and to accelerate the computation speed compared to pure numerical/stochastic methods. However, the simplicity

and validity of analytic methods often break down under special situations such as complicated boundary conditions, extreme source/detector distance or uncommon  $\mu_s/\mu_a$  ratio. Hereby, when the aim is to model the light propagation in the tissue where the boundary and interior geometries are complex as well as varying optical properties, the optimal choice may be pure numerical methods inside of hybrid analytic-numerical method.

There are also a few forward modelling approaches that do not rely on the RTE, such as the random walk theory [56,57] and the Markov random field method [58]. However, these methods have been far less widely used nowadays, and are left out of the discussion here.

The comprehensive elaborations of every forward modeling approaches are beyond the scope of this thesis. To understand the coupling effects of  $\mu_a$  and  $\mu'_s$  in the next chapter, the most widely used and classical model, the Diffusion Equation (DE), is briefly described here.

The DE is under  $P_1$  approximation of the RTE, i.e., assuming the higher order Legendre Polynomials (order  $N>1$ ) in the spherical harmonic expansion of the RTE are all 0. Additionally, the DE must adapt the assumptions that (1)  $\mu'_s \gg \mu_a$  (strong scattering media), (2) the temporal change on light radiant flux  $\mathbf{J}$  is negligible during the period of one photon transport in media, and (3) the light source is isotropic. Then we can obtain the DE as follows:

$$\frac{1}{c} \frac{\partial}{\partial t} \Phi(\mathbf{r}, t) - D \cdot \nabla^2 \Phi(\mathbf{r}, t) + \mu_a \Phi(\mathbf{r}, t) = S_0(\mathbf{r}, t) \quad (2.7)$$

Where  $\Phi(\mathbf{r}, t)$  is the fluence rate, the integral of light energy radiance  $L$  over all angles, and  $S_0$  is the integral of isotropic source radiance over all angles.  $D = 1/3(\mu_a + \mu'_s)$  is so-called optical diffusion coefficient. The flux  $\mathbf{J}$  follows Fick's first law:  $\mathbf{J} = -D \cdot \nabla \Phi$ . Based on Eq. (2.7), the light reflectance and transmittance (i.e., the measured photons on tissue surfaces) can be predicted under proper boundary conditions [59–61], e.g., zero boundary condition (ZBC) or extrapolated boundary condition (EBC). The mismatch of the refractive index on the boundary also needs to be considered. The accuracy of the modelling based on the DE is heavily dependent on the boundary conditions [61,62].

Forward modelling based on the DE is intrinsically limited by its assumptions. The DE fails in the high spatial and temporal frequency domains, leading to the model breakdown for short source-detector distances, for short time values (early photons), and for highly absorbing objects. Moreover, to ensure the accuracy, both light fluence rate and light flux shall be calculated to obtain the radiance [63,64].

In summary, although analytical forward modelling methods are very quick and useful, they are not accurate at many extreme circumstances. The RTE can still not be solved

analytically for arbitrarily shaped objects, as needed for common real-life applications. In principle, a pure stochastic method to solve the RTE up to any desired accuracy is the Monte-Carlo simulation.

### **Inverse problem**

Given the forward problem involves modelling the light transport by a known set of optical properties, the inverse problem is then recovering the optical properties from the measured light on tissue surfaces. The inverse problem is usually formalized as solving the equation of the form:

$$m = \mathcal{F}^{-1}(\mu) + e \quad (2.8)$$

Here  $m$  is the measured data, assumed to be given.  $\mu$  is the vector of optical parameters to recover, and  $e$  is the observational noise model which constitutes the arbitrary corruptions in  $m$ . The function  $\mathcal{F}^{-1}$  indicates the inverse operation of the forward model function  $\mathcal{F}$ .

In tissue diffuse optics, three types of inverse problem may be defined:

- (1) Imaging without amplitude information:  $m$  is not determined as absolute numbers of photons, but their relative numbers at different spatial, frequential, or temporal windows can be obtained.
- (2) Relative imaging:  $m$  is available in two or more sets with some differences of significance on  $\mu$  having occurred between their acquisitions. The reconstruction is dynamic and may be approximated by a linear reconstruction.
- (3) Absolute imaging:  $m$  is only one set of available but sufficient data for the inverse process. The  $\mu$  reconstruction requires a forward model to be fitted with  $m$  nonlinearly.

These three types of problem address three different branches in tissue diffuse optics: Type (1) mainly addresses the performance assessment of the diffuse optics instruments, Type (2) the relative imaging addresses the functional near infrared spectroscopy (fNIRS) which focuses on changes only, and Type (3) the absolute imaging addresses the diffuse optical tomography (DOT) that estimating absolute optical properties. The three types are of increasing difficulty and need to be distinguished in the different measurement contexts.

In this thesis the main task is focusing on the third type of problem, i.e., the nonlinear inversion of the measured data  $m$  to determine absolute quantities of optical properties  $\mu$ . The nonlinearity of the problem originates from the dominance of scattering in light propagation which makes absorption nonlocal and dependent on scattering distribution as well. The opposite of such nonlinearity is x-ray CT wherein scattering is minimal. Furthermore, as stated by

*Jacques Hadamard* for the necessary conditions of a well-posed problem [65] are: (1) the solution exists, (2) the solution is unique, and (3) the solution continuously depends on the measured data (small variation in data does not produce large error in the solution). The absolute inverse problem does not fulfill (2) and (3) conditions (based on data types) and hence is an ill-posed problem. Therefore, the recovery of absolute quantities of optical properties must follow the scheme of ill-posed, nonlinear inversion.

The nonlinear inversion usually does not lead to an explicit formula. However, the mathematical formulation could be implicitly expressed as following:

$$\mu = \arg \min\{|\mathcal{F}(\mu) - m| + \alpha\mathfrak{R}(\mu)\} \quad (2.9)$$

Here  $\alpha$  is the regularization parameter and  $\mathfrak{R}(\mu)$  is the regularization function. The selection of the regularization function is discussed in chapter 3. The  $\arg \min |\mathcal{F}(\mu) - m|$  term involves the proper selection of the objective function. A common objective function is to calculate the residual norm based on  $\chi^2$  distribution.

$$\chi^2 = \left(\frac{\mathcal{F}(\mu) - m}{\sigma}\right)^2 \quad (2.10)$$

Where  $\sigma$  is an estimate of the standard deviation of measurement  $m$ . Then the inversion becomes a problem of minimizing  $\chi^2$  by the iteration of modifying optical parameters  $\mu$ .

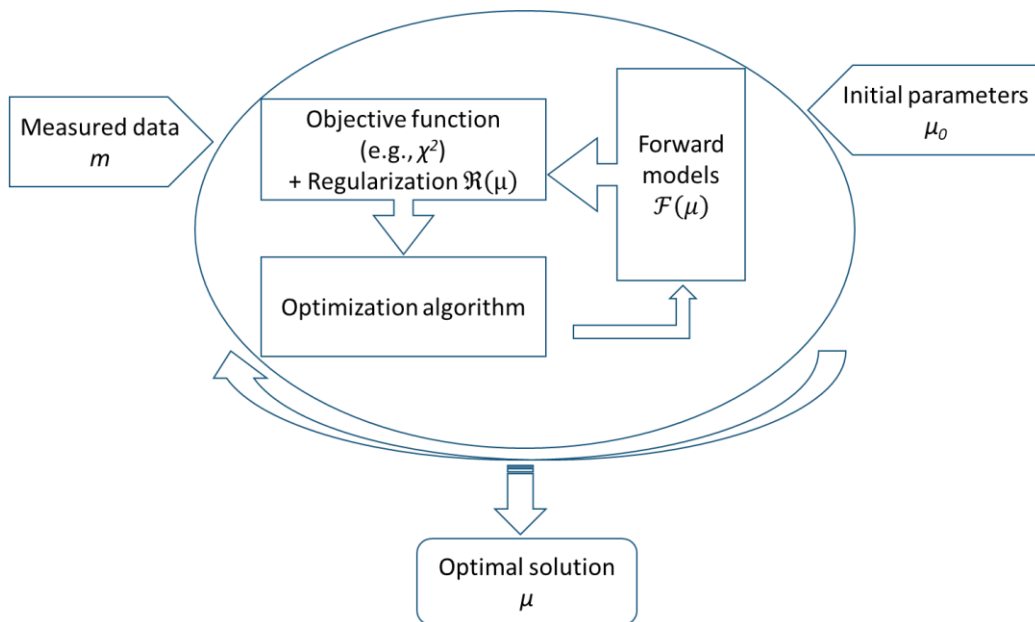


Fig. 2.4: The flow scheme of inverse problem iteration

In terms of optimization theory, the inversion then looks for the direction of the steepest descent update direction, in the sense this will give the most rapidly residual norm decreases

and the most optimal solution locally. Typically, Newton methods would involve from here by taking the derivative of the objective function. And if the inversion is for non-singular properties at many locations  $N$  in the tissue  $\mu_{i,N}$  by multiple measurements  $m_N$ , the derivative matrix such as Hessian matrix and Jacobian matrix will also involve, which is common for finite element methods. More details can be found at a review [66] but are not the focus here.

As for the optimization itself, much effort has been devoted to all the possibilities as well, such as Gauss-Newton method or quasi-Newton methods. The Levenberg-Marquardt method has been validated by many groups in diffuse optics [40,67]. Improved methods such as Bayesian-based optimal estimation method [68] and genetic algorithm [69] have also been proposed. Furthermore, besides knowledge-driven approach as mentioned above, recent developments on regularization also introduce the data-driven method for diffuse optical tomography, more details can be found at [70].

Essentially, the accuracy of nonlinear iterative inversion requires the efficiency of forward modelling. The multiple evaluations of the selected data types by the forward model are the core of the accurate recovery.

## 2.4 Monte-Carlo modelling of light transport in tissues

As a numerical approach, Monte-Carlo (MC) methods provide flexibly precise solutions for modelling light transport in tissues, serving as a stochastic interpretation to the RTE. In MC, the trajectory of photons is simulated as the kind of persistent random walk in which every step's direction is dependent on the direction of the previous step. On the contrary, the simple random walk considers all the steps are independent. The ensemble-averaged quantities in diffuse optics, such as diffuse reflectance, can be precisely and efficiently estimated, once a sufficiently large number of photons are simulated and tracked.

For the forward problem, the MC method is regarded as the gold standard method to model light transport in tissues, for its flexibility and accuracy. Light distribution can be simulated by MC for given optical properties. To solve the inverse problem, the optical properties can be estimated by fitting the MC simulations with the experimental measurements.

There are several variants of MC modeling of light propagation, for example, the “albedo-weight” method (AW) [40], the “albedo-rejection” method (AR) [67], the “absorption-scattering path length rejection” method (ASPR) [68], and the microscopic Beer-Lambert law method (mBLL) method [69]. These variants have been proved to be statistically equivalent on modelling light diffuse propagations, and the differences are minor [71]. The major difference among these variant methods is the convergence speed to obtain the final simulation results. All

the methods follow the same general procedure of modelling as following. The incident light will be simulated as launched photon packets with an assigned initial weight when they enter the tissue model at the positions of the source fibers. The optical properties of the tissue, including the absorption coefficient  $\mu_a$ , the scattering coefficient  $\mu_s$ , the anisotropy factor  $g$ , and the refractive index  $n$  shall be predefined at each spatial site in the tissue model. The random walk steps of photon packets will be traced when photons interact with the tissue, and the step size and step direction will be sampled randomly based on the predefined  $\mu_s$  and  $g$ , respectively. The photon packets also follow Snell's law and Fresnel's equations (i.e.,  $n$ ) when they hit either an internal tissue boundary or the tissue-air interface. At each step's end, the photon packet's weight is reduced according to  $\mu_a$  and the step size. The photon packages propagate in the tissue for many steps until they exit from the boundary, or their weights are reduced to a certain threshold. The cumulative distribution of all photon trajectories can give an accurate estimate of the optical properties of interest, once a sufficient large amount of photon packets is launched and traced.

Figure 2.5 is the flow chart for Monte Carlo modelling of the propagation of photon packets. In total, there are seven major events/processes to be handled by Monte-Carlo for the life cycle of a photon packet in tissues: 1. Launching, 2. Step size calculation, 3. Movement, 4. Absorption, 5. Scattering, 6. Boundary crossing, and 7. Termination. A brief description will be given in below along with the flow chart.

The core of the Monte-Carlo modelling is a pseudo-random number generator, as it relies on the repeatedly sampling of random variables from their probability distributions. Such sampling method is called "inverse distribution sampling" method, and a detailed mathematical explanation can be found in [72]. The pseudo-random number generator is involved in calculate every step size calculation  $L$  of photon packet, to calculate the step direction  $S$  during scattering, and to decide to reflect or transmit when photon hits a boundary.

1. First, every photon packet is sequentially launched into the tissue with a certain but different seed. The first step in the tissue is considered as a ballistic transport while the step size is determined by the seed. The Fresnel's equations will also be considered if the refractive indices are different at both sides of the tissue surface.

2. The calculation step size  $L$  after ballistic transport is carried out by a pseudo-random number generator, in which the probability density function used is  $p(L) = \mu_t \exp(-\mu_t L)$ , according to Beer-Lambert law.

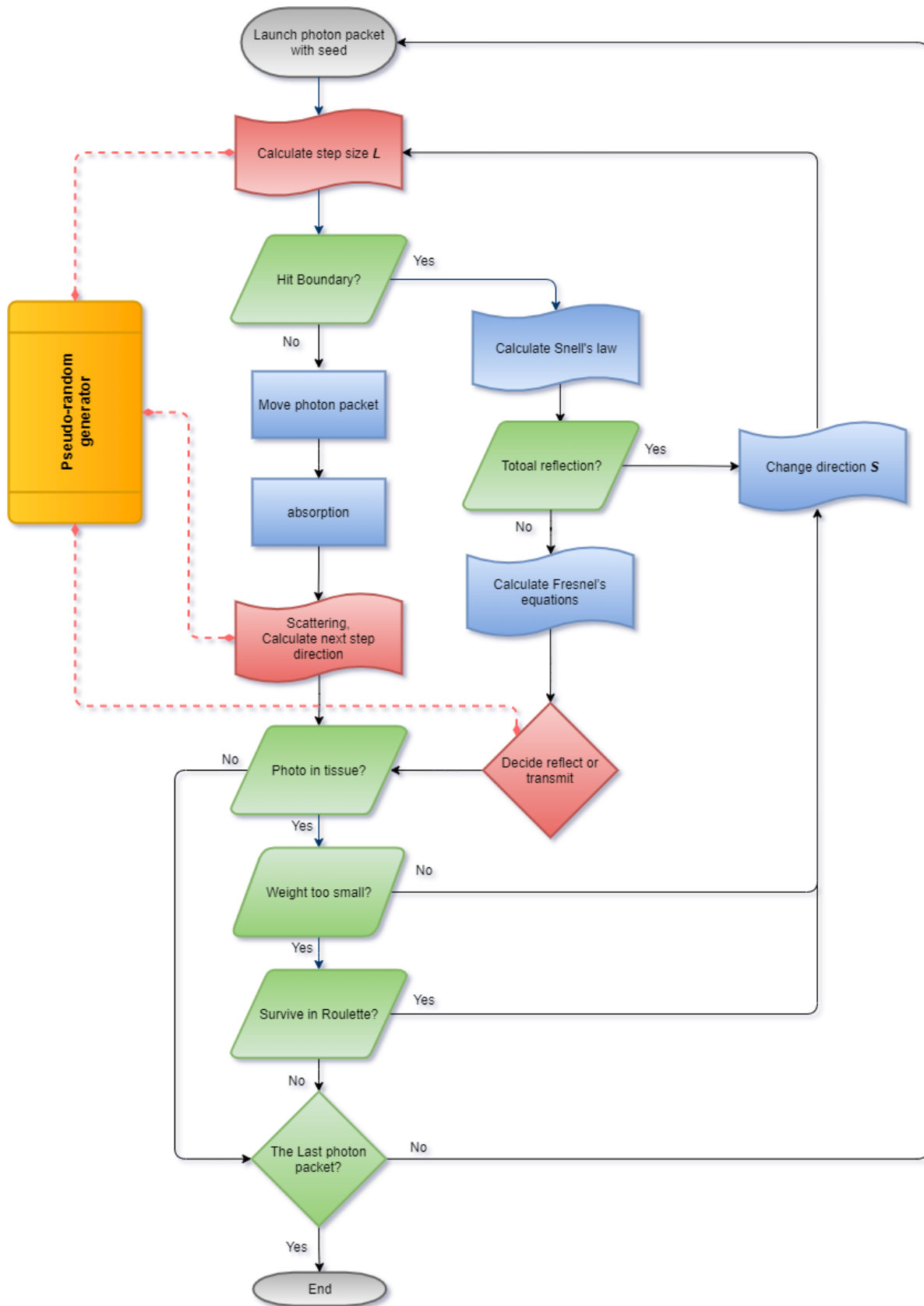


Fig. 2.5: The flow chart for Monte Carlo modelling of the propagation of photon packets

3. The movement of a photon packet is carried out after the determination of  $L$  and  $S$ .

4. The photon packet may hit a boundary during the movement, and four steps are involved for calculating the boundary crossing: (1) Update the fraction of  $L$  which remains in the current layer; (2) Calculate Snell's law and determine whether a total reflection occurs; (3) Calculate Fresnel's equation to get the local reflectance rate  $R$ ; (4) Use pseudo-random number generator to get a random number  $\varepsilon$  and compare it with the local reflectance rate, determine the photon packet to reflect when  $\varepsilon \leq R$ , and to transmit when  $\varepsilon \geq R$ .

5. The absorption of a photon packet is carried out in the way of updating the weight of a photon packet according to Beer-lambert law. The absorption process can happen after its movement at every step but may also occur after the entire simulation. The so-called "White Monte-Carlo" method [69] saves trajectories of photon packet and then calculate absorption and properly scaling and binning in post-simulation procedure.

6. The scattering of a photon packet is the process to determine the next step's movement direction  $S$  of a photon packet. The direction is decided by polar angle  $\theta$  and azimuthal angle  $\phi$  in spherical coordinate system, and the angles are sampled by the pseudo-random number generator separately. The probability density function of  $\cos\theta$  following the above-mentioned *Henyey-Greenstein* phase function decided by local  $g$  value, while the azimuthal angle  $\phi$  is purely decided by a random number  $\phi = 2\pi\varepsilon$ .

7. Finally, to terminate a photon packet there are two ways. First, a photon packet that, after traveling in the medium, escapes from the same surface of the tissue as the detector located is terminated and the remaining fraction weight is scored as diffuse reflectance. On the other hand, if the weight of a photon packet  $W$  in the tissue has fallen below a predefined threshold  $\Theta$ , then the photon packet needs to undergo a process "Roulette", in which the photon will be given one chance to survive with an updated weight  $mW$  or is directly terminated ( $W=0$ ). Surviving is decided by another random number with the criteria  $\varepsilon \leq 1/m$ . The termination can therefore be unbiased and conserve the total energy in the same time.

The above steps give a description about common light-tissue interactions in MC Modelling and can be directly implemented for simulating the steady state (continuous wave) light transport in tissues. Other interactions and properties, such as fluorescence, Raman scattering, polarization, can also be incorporated into the model by adding additional parameters. Furthermore, for simulating time-resolved measurements by MC modelling, all the steps remain the same, except that one additional parameter, i.e., time, is tracked and recorded at when each above-mentioned light-tissue interaction occurs.

Since the measurements of reemitted light from tissues are usually on the tissue surfaces, MC modelling pays special attention on the photons there. Nevertheless, when the entire

trajectories of photons are tracked and recorded in the time-resolved manner, it is completely feasible to determine any local fluence within the tissues. Figure 2.6 gives an example for the volume-based MC modelling in a homogenous tissue slab geometry. The mean trajectories of detected photons, where the detector locates 60 mm away from the source, can be presented as the spatial distribution of the mean partial pathlength (MPP) values. The tissue is modelled in a finite volume manner, and each photon that travelled through a predefined volume on its way to the detector will be tracked and recorded as a property of the volume.

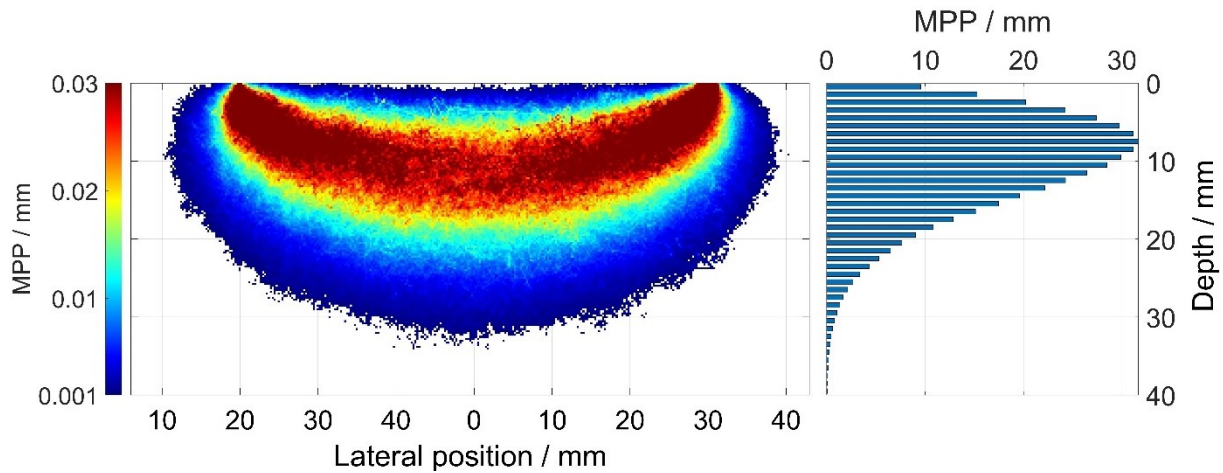


Figure 2.6. The Monte Carlo modelling of the photon propagation trajectories in a homogenous tissue slab ( $\mu_a = 0.1 \text{ cm}^{-1}$ ,  $\mu'_s = 10 \text{ cm}^{-1}$ ,  $n = 1.33$ ). Left: MPP in each volume represent the visiting probability distribution of the volumes for the detected photons; Right: the cumulative MPP summed along with the depth.

As shown in Figure 2.6, the visiting probability distribution [73] of the detected photons, i.e., the spatial distribution of probability of visiting the voxels by the photons travelling from source to the detector, emerges as the “banana-shape”. This phenomenon has been investigated and discussed in several studies [74,75] and validated by Monte-Carlo simulations. According to the patterns shown in Figure 2.7, the so-called “banana-shape” region illustrate the regions where the photon migration paths are concentrated. The MPP values in logarithmic form present in different colors to represent the visiting probabilities. In total five billion photons were launched during two simulations, where the source-detector distances are 1 cm in Fig. 2.7(a) and 6 cm in Fig. 2.7(b). Obviously, the detected photons would have higher visiting probabilities at deeper regions if the detector is located more distant from the incident light source. Therefore, it is possible to separate the optical properties of different layers by analyzing the time-resolved measurement data from different source-detector distances.

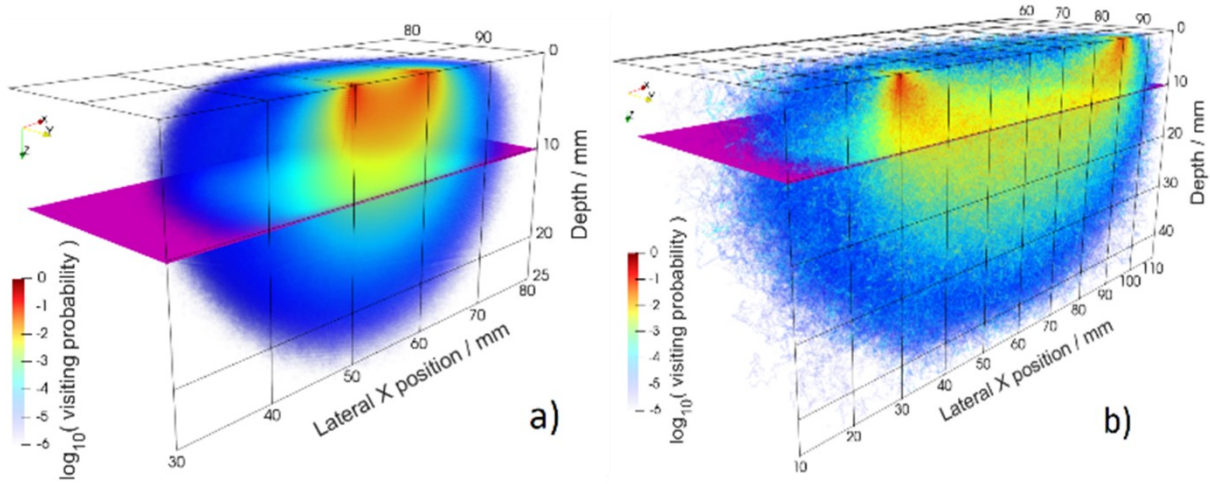


Figure 2.7. Monte Carlo modelling of the “banana shape” trajectories of detected photons in the different source-detector distances. In a homogenous tissue slab ( $\mu_a = 0.1 \text{ cm}^{-1}$ ,  $\mu'_s = 10 \text{ cm}^{-1}$ ,  $n = 1.33$ ), the source-detector distances are (a) 1 cm and (b) 6 cm, MPPs in each volume are presented in logarithmic form. The pink plane indicates the 1 cm deep from the surface of the incident source.

In this thesis, the experiments were carried out to record the time-resolved diffuse reflectance, and the analyses were focused on both the time domain and space domain observations of the photon migration pattern on the detectors. Therefore, the MC modellings used in this thesis mainly simulate the distributions of times of flight (DTOF) curves at several source detector separations, rather than the detailed photon trajectories in the tissues. By comparing the simulated DTOFs and the measured DTOFs, one can retrieve the optical properties of interest.

The MC program in this thesis used parallel computation technique to significantly accelerate the simulations. The idea [76] to parallel compute with GPU has been proven to speed up MC simulations more than 1000 times than those performed on the conventional CPU-based computer. The main quantitative analyses in this thesis were carried out by the GPU-based CUDA (Compute Unified Device Architecture) program to realize parallel computation. NVIDIA graphics cards were deployed to model photon transport in turbid media.

# 3

## Method and instrumentation for tissue diagnosis

Whereas a physical model is essential for data analysis, the biomedical applications of diffuse optics are also highly influenced and defined by the measuring methods, the detected data types, and the criteria of concerns. In practice, the different modalities of NIRS system deploy on clear-cut different application scenarios, exploit instruments with different levels of complexity, and assess the different variants derived from measurements [77–79]. In this chapter, the state-of-the-art modalities of NIRS system and their comparison are briefly described and reviewed in 3.1. One novel methodology that incorporates the major modalities will be explained and presented in 3.2. The instrumentation and its compartments used for tissue diagnosis are introduced in 3.3. In 3.4, the investigated phantoms and their preparation are presented and discussed.

### 3.1 Modalities of NIRS system

Three typical modalities of NIRS are commonly used for tissue diagnosis: i) continuous wave (CW), ii) frequency domain (FD), and iii) time domain (TD). The concepts of modalities and the physiological variables they investigate, respectively, are summarized and compared in Fig. 3.1. detailed technical considerations related to specific application scenarios of the modalities are presented in the following sections.

#### CW-NIRS system

Generally speaking, CW-NIRS [21] systems use steady state light sources with intensity constant in time and light detection is solely based on the intensity measurement regardless of which type the light source is. In practice, however, the CW (continuous wave) light source is nevertheless often amplitude-modulated at a low frequency (few kHz) to significantly improve the SNR and sensitivity by applying phase lock-in detection techniques. Anyhow, no time or phase information is analysed in this approach but only amplitude. CW-NIRS systems are the most simplistic among the modalities that make the use of simple detectors and detection

electronics, and can enable fast data acquisition and analysis. However, CW-NIRS cannot decouple the effects of light absorption and scattering since no measure of the optical pathlength that photons travelled is available. Therefore, the absolute values of  $\mu_a$  and  $\mu_s'$  cannot be determined simultaneously, and investigations of complex, non-homogeneous media are far from real situations. For a single distance CW-NIRS system, only the relative change of cHb, cHbO<sub>2</sub>, and cHbT can be obtained. For a multi-distance CW-NIRS system or so-called spatially resolved spectroscopy (SRS), it is possible to determine the absolute quantity of  $\mu_a$ , given the *prior* knowledge about  $\mu_s'$  from other techniques or from assumptions. The absolute cHb, cHbO<sub>2</sub>, and cHbT can then be derived. Nevertheless, the superficial contaminations to the deeper brain's optical properties remains a challenging problem for CW-NIRS today due to its fundamental assumption of a homogeneous semi-infinite medium. Typically, the source-detector distance of CW-NIRS system has values between 30 to 40 mm in order to properly probe the cortex of adults, while for new-borns a shorter distance (15-30 mm) can be used and have been proved more efficient [80].

### **TD-NIRS system**

TD-NIRS systems [81] use ultrashort (picosecond) pulsed laser as light source to irradiate subjects, and use detection apparatus with temporal resolution in sub-nanosecond order to collect and count the diffusely remitted photons and measure their time of arrival with respect to the input pulse. Unlike CW-NIRS systems which only measure light intensity, TD-NIRS systems measure light pulses in time domain after light propagates through the turbid media. The histogram of the time-of-flight of photons re-emerging from the turbid media, often known as the photon's DTOF (distribution of time-of-flight) or sometimes TPSF (temporal point spread function), plays the central role in TD-NIRS systems. From time domain perspective, the injected light pulses in a turbid medium will be delayed due to the finite time that light travels between the injection point (source) and detection point (detector); they will be broadened as the consequence of multiple scattering and the dispersion of the photons in different directions and paths; and they will be attenuated because of absorption and scattering. The absorption and scattering in turbid media impact the DTOF curves in different ways. Higher scattering will result in an increased broadening and delay of DTOF curves, as well as fewer detectable photons at a certain detection area. Higher absorption on the other hand will result in a global decreased probability of detecting photon from any possible paths in media, and will particularly affect the trailing edge of DTOFs (longer photon travelling path), while substantially remaining the temporal position of DTOFs unchanged. Owing to such the different effects from absorption and scattering on DTOFs, TD-NIRS systems are able to simultaneously

determine the absolute values of  $\mu_a$  and  $\mu_s'$  with simply a single-distance time-domain measurement, and subsequently the absolute values of cHb, cHbO<sub>2</sub>, cHbT and S<sub>O<sub>2</sub></sub> at least for homogenous media. Employing time-gating techniques [82] and moment analysis [83] methods, the depth-dependent information of turbid media's optical properties can be retrieved which in turn allows the better spatial resolution with respect to locating the origin of changes in chromophore concentrations. A proper quantitative determination of cerebral hemodynamic parameters with high selectivity can be obtained.

### **FD-NIRS system**

FD-NIRS systems [84] are based on periodically intensity-modulated light source (with angular frequencies at the order of 100 MHz to 1 GHz). Light intensity demodulation and phase shift are measured at the detector site. Compared with CW-NIRS systems, the additional phase information allows simultaneous determination of  $\mu_a$  and  $\mu_s'$  as it can be used to decouple the effects from absorption and scattering together with intensity demodulation (AC/DC). Since the relation between TD and SD information can be expressed with the help of a Fourier transform, FD-NIRS systems can be regarded as the TD-NIRS at only one or a few frequencies, and TD information can be treated as the FD information with all the possible frequencies from DC to 100GHz (if TD information has sufficient temporal resolution, e.g., of 1 ps). The main advantage of FD-NIRS systems is that they are less expensive compared with up-to-date time-resolved instrumentations.

Fig. 3.1 gives a simple visualization of three modalities about their principles, measured data types, detected hemodynamic signals, and applicable structures.

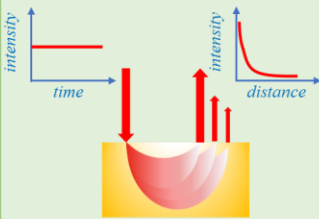
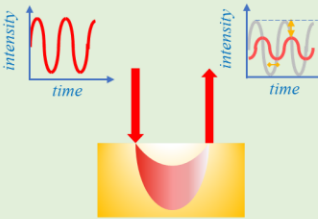
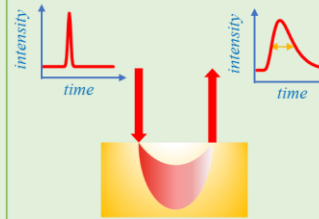
Modalities	Continuous Wave NIRS*	Frequency Domain NIRS	Time Domain NIRS
Principles			
Relative Values	$\Delta cHb, \Delta cHbO_2, \Delta cHbT, \Delta SO_2$ Homogenous model, with assumed pathlength	$\Delta cHb, \Delta cHbO_2, \Delta cHbT, \Delta SO_2$	$\Delta cHb, \Delta cHbO_2, \Delta cHbT, \Delta SO_2$
Absolute Values	$cHb, cHbO_2, cHbT, SO_2$ Homogenous model, with assumed $\mu_s'$	$cHb, cHbO_2, cHbT, SO_2,$ and simultaneously ( $\mu_a, \mu_s'$ )	$cHb, cHbO_2, cHbT, SO_2,$ and simultaneously ( $\mu_a, \mu_s'$ )
Accuracy	Low	Moderate	High
Portability	High	Moderate	Moderate
Cost	Moderate	Moderate	High
Discrimination of extracerebral and cerebral tissue	Non-feasible for absolute values; possible for relative values, with short channel regression	Feasible, with layered or Atlas models	Feasible, with layered or Atlas models

Fig. 3.1: Modalities of NIRS systems. The comparison of their principles, measurable data types, detected hemodynamic signals and applicable conditions, accuracy, portability, cost and the ability of discriminating data/signals from extracerebral and cerebral tissue. \*Note: The Continuous Wave NIRS modality here refers to the spatially resolved spectroscopy (SRS) / multi-distance method.

For many biomedical applications of diffuse optics, especially mapping the functioning of brain, a system's ability to probe the tissue in depth i.e., "penetration depth", is of the utmost importance. Such ability can be evaluated by defining a *Relative Contrast*, i.e., the relative change of a measurand with respect to its baseline value. In order to compare CW and TD modalities, intensity was used in a study [85] as the measurand to investigate the relative contrast with respect to a local absorption perturbation set in different depth (10 to 60 mm) in a homogenous turbid media. The CW-NIRS system was tested for different source-detector distances  $\rho$  (1 to 5 cm) and the TD-NIRS system has null source-detector distance and applies time-gating concept (from 1 to 11 ns time windows of DTOFs). As shown in Fig. 3.2, it is reported that the TD modality has much better relative contrast at any depth under the same maximum safe laser exposure, representing the larger physical limit of potential detectability. Under the criteria that contrast  $>1\%$  and Poisson noise level  $<1\%$ , for a TD modality with null source-detector distance an ideal maximum depth of 60 mm was achieved, whereas for the SD modality only 30 mm of maximal depth can be reached at the largest usable source-detector distances  $\rho = 5$  cm. Recent studies have also demonstrated that mean penetration depth does not depend on  $\mu_a$  and  $\rho$  [86], and mean path length of travelling photons is invariant in media with different scattering properties [87].

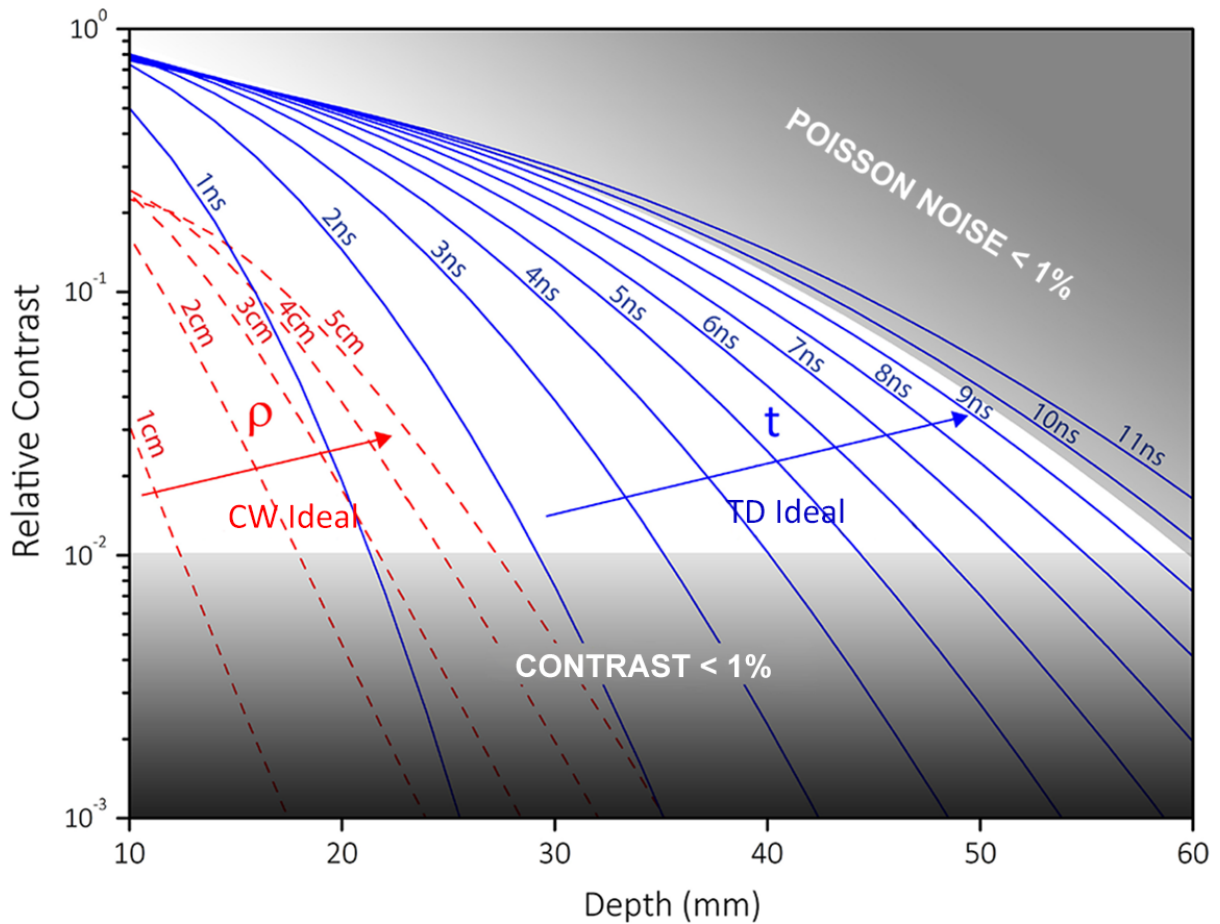


Fig. 3.2: Comparison of CW and TD modalities on probe the changes in depth. A local absorption perturbation of  $\Delta\mu_a = 0.1 \text{ cm}^{-1}$  over a  $1 \text{ cm}^3$  volume is localized in various depth from 10 to 60 mm in a homogenous turbid medium with  $\mu_a = 0.1 \text{ cm}^{-1}$  and  $\mu_s' = 10 \text{ cm}^{-1}$ . The relative contrasts of ideal CW systems (red dash lines) measuring at  $\rho = 1$  to 5 cm and an ideal null source-detector distance TD system's various time-gated windows (blue solid lines) at  $t = 1$  to 11 ns were compared. The simulations consider ideal sources and detectors with laser exposure and acquisition time compatible with clinical environment [85]. (Reprinted from *J. Biomed. Opt.* (2016): by [Antonio Pifferi, et al.](#), licensed under [CC BY 4.0](#)).

Owing to the outstanding ability of TD-NIRS modality on the accuracy, absolute quantification, and depth-resolved localization, the systems based on a TD approach have been rising among others. A modified hype cycle diagram has been given in a review [85] according to the expectations about visibility, usability, and relative maturity level for the TD and CW-NIRS modalities. In Fig. 3.3 the CW approach includes all systems which are based on physical models that rely on the intensity measurement, while the classical TD approaches represents the previous and state-of-art TD instrumentations. And TD next gen stands for the TD systems with breakthrough in terms of performance, size, cost, and flexibility, enabled by both the physical models of TD diffuse optics and the promising new optoelectronics and devices.

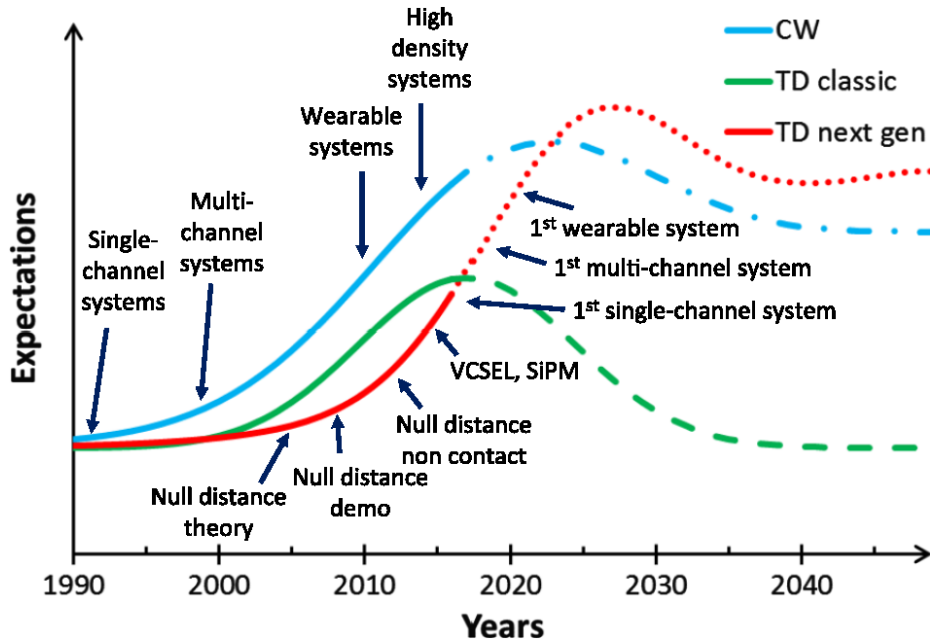


Fig. 3.3: Modified hype cycle diagram for the CW and the TD approaches. The diagram represents the review authors' interpretation of the hype cycle of these technologies [85]. (Reprinted from *J. Biomed. Opt.* (2016): by [Antonio Pifferi, et al.](#), licensed under [CC BY 4.0](#)).

### 3.2 Integration of time and space domain NIRS

In this section, I will propose and discuss a new methodology, i.e., Space-enhanced Time Domain (SeTD) method which attempts to integrate CW-NIRS and TD-NIRS modalities by integrating the information in space and time domain so as to realize a higher accuracy on  $\mu_a$  and  $\mu_s'$  and to overcome the potential limit of detectability with the sense of low photon existence.

#### Negative correlation of $\mu_a$ and $\mu_s'$ in SD

The contributions of scattering and absorption properties on measured intensity curve profiles in space domain are negatively correlated with each other. As shown in Fig. 3.4(a) and 3.4(b), the Monte-Carlo simulations of the space-domain reflectance intensity curves for a 5 cm homogenous slab with various  $\mu_a$  and  $\mu_s'$  values are presented. In Fig. 3.4(a), the  $\mu_s'$  value is fixed at  $8 \text{ cm}^{-1}$  while the  $\mu_a$  value increases from  $0.05$  to  $0.3 \text{ cm}^{-1}$ ; the gradual darkening red shows the effects on SD intensity curves. Meanwhile in Fig. 3.4(b), the  $\mu_a$  value is fixed at  $0.1 \text{ cm}^{-1}$  while the  $\mu_s'$  value increases from  $5$  to  $10 \text{ cm}^{-1}$ ; the gradual darkening blue shows the effects as well. Therefore, when solving the inverse problem from SD measurements, the effects on SD reflectance intensity curves from  $\mu_a$  and  $\mu_s'$  variations will be canceled out with each other. A simultaneously increasing  $\mu_a$  and decreasing  $\mu_s'$  to certain extent, or by the opposite

way: a simultaneously increasing  $\mu_s'$  and decreasing  $\mu_a$ , can result a same SD curve as the original  $\mu_a$  and  $\mu_s'$  combination. This negative correlation of  $\mu_a$  and  $\mu_s'$  in SD causes the non-uniqueness of the solutions.

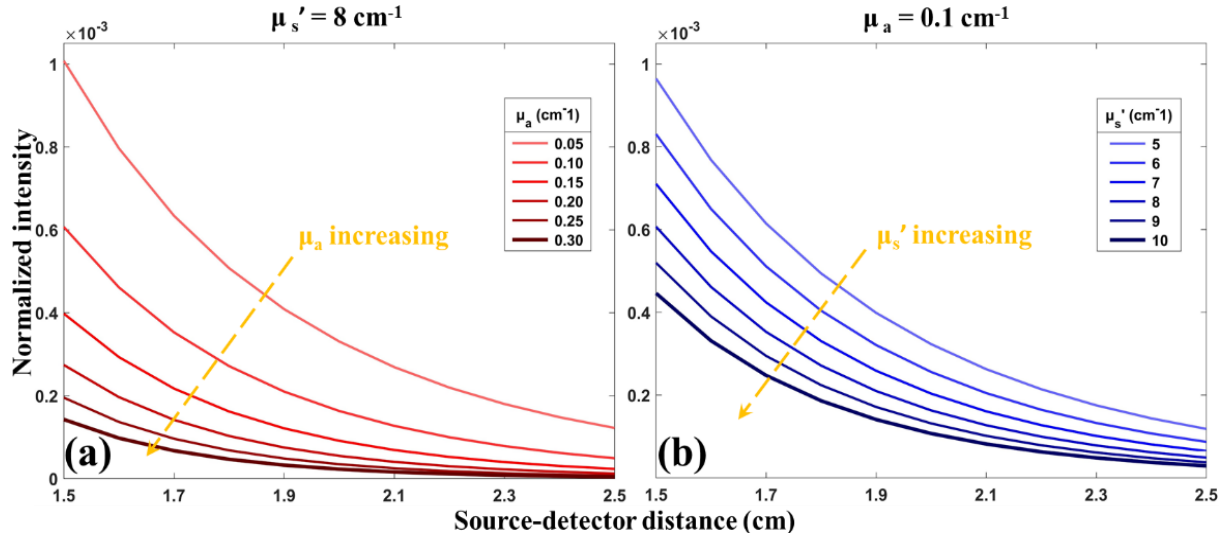


Fig. 3.4: MC simulated Space-domain reflectance amplitude curve profiles at 2 cm source-detector distance on a 5 cm thick slab, with (a) varying  $\mu_a$  when  $\mu_s'$  is fixed at  $8 \text{ cm}^{-1}$ , and (b) varying  $\mu_s'$  when  $\mu_a$  is fixed at  $0.1 \text{ cm}^{-1}$

As mentioned in Section 3.1, multi-distance CW-NIRS system or so-called spatially resolved spectroscopy (SRS) can determine the absolute value of  $\mu_a$ , given the prior knowledge about  $\mu_s'$ . The physical model for SRS can be derived from diffusion theory under semi-infinite geometry and zero boundary condition. When  $(\rho \times \mu_s') \gg 1$ , i.e., the detector is far from the source, the time-resolved reflectance can be written as [34]:

$$R(\rho, t) = \frac{z_0}{(4\pi Dc)^{3/2}} t^{-5/2} \exp\left(-\mu_a ct - \frac{\rho^2}{4Dct}\right) \quad (3.1)$$

By integrating with time. The space-resolved reflectance can be written as:

$$\begin{aligned} \int_0^\infty R(\rho, t) dt &= \frac{z_0}{(4\pi Dc)^{3/2}} \cdot \int_0^\infty t^{-2-1/2} e^{-\mu_a ct - \frac{\rho^2}{4Dct}} dt \\ &= \frac{2z_0}{\pi\mu_{eff}} \cdot \frac{\partial^2 e^{-\mu_{eff}\rho}}{\partial(\rho^2)^2} \\ &= \frac{z_0 e^{-\mu_{eff}\rho}}{2\pi\rho^2} \cdot \left(\mu_{eff} + \frac{1}{\rho}\right) \end{aligned} \quad (3.2)$$

in which  $\rho$  is source-detector distance and  $\mu_{eff}$  is effective coefficient defined in section 2.1. In practice, the light attenuation  $A = \ln R / \ln R_0$  is more often to be measured. By introducing  $A$  into Eq. (3.2) and differentiating with  $\rho$ , we have:

$$\frac{\partial A}{\partial \rho} = -\frac{\partial \ln(R)}{\partial \rho} \approx \mu_{eff} + \frac{2}{\rho} \quad (3.3)$$

It is easy to understand that  $\partial A/\partial \rho$  determines the SD curve profiles. From Eq. (3.3), it can be revealed that within a certain range of  $\rho$ , the SD curve profiles is completely determined by  $\mu_{eff}$ , *i.e.*, by the product of  $\mu_s'$  and  $\mu_a$ . Absorption and scattering have an approximate reciprocal relation, given  $\mu_{eff} = \text{constant}$ , which confirms the non-uniqueness of CW results [88] and the negative correlation of  $\mu_s'$  and  $\mu_a$ .

### Positive correlation of $\mu_a$ and $\mu_s'$ in TD

The contributions from scattering and absorption properties on DTOF curves are positively correlated with each other. As shown in Fig. 3.5(a) and 3.5(b), the DTOF curves from Monte-Carlo simulations for a 5 cm homogenous slab with various  $\mu_a$  and  $\mu_s'$  values are presented. The DTOF curves from the simulations with fixed  $\mu_s' = 8 \text{ cm}^{-1}$  and  $\mu_a = 0.05$  to  $0.3 \text{ cm}^{-1}$  are normalized and compared in Fig. 3.5(a), indicating the increasing  $\mu_a$  values will narrow the width of DTOF shape. In Fig. 3.5(b) the DTOF curves with fixed  $\mu_a = 0.1 \text{ cm}^{-1}$  and  $\mu_s' = 5$  to  $10 \text{ cm}^{-1}$  shows the fact that increasing  $\mu_s'$  values will widen the DTOFs, *vice versa*. The positive correlation of  $\mu_a$  and  $\mu_s'$  stands for any increase/decrease of one coefficient must be compensated by an increase/decrease of the other. Solving the inverse problem in time domain is in fact a curve fitting process, the DTOF will always need to be normalized and then fit with theoretical curves after convoluted with IRFs. During the normalization, the intensity information will be inevitably lost.

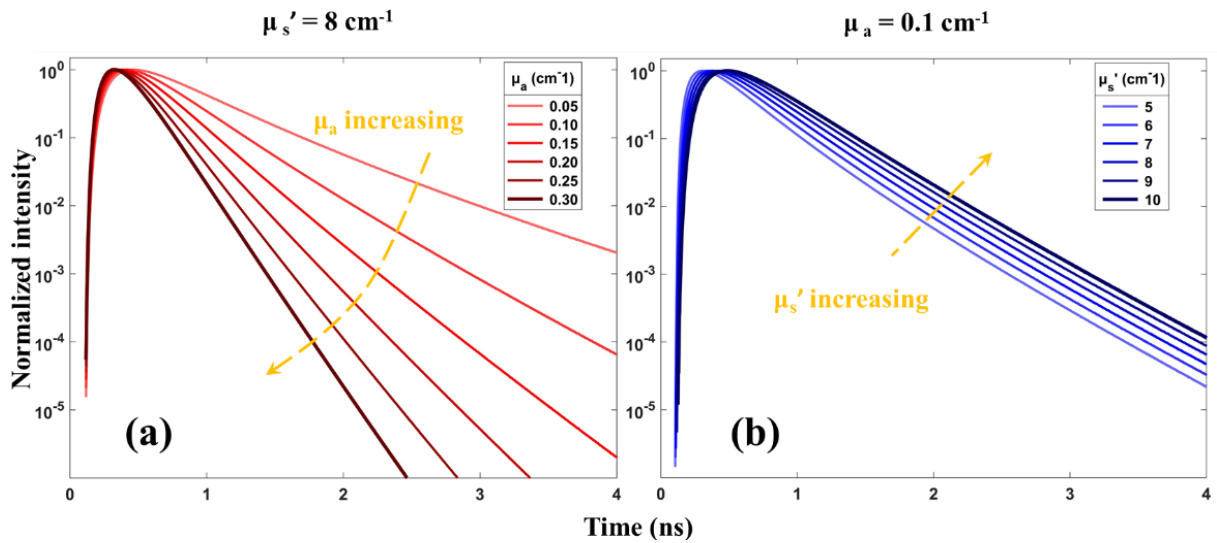


Fig. 3.5. MC simulated reflectance DTOFs curve profiles at 2 cm source-detector distance on a 5 cm thick slab, with (a) varying  $\mu_a$  while the  $\mu_s'$  is fixed at  $8 \text{ cm}^{-1}$ , and (b) varying  $\mu_s'$  while the  $\mu_a$  is fixed at  $0.1 \text{ cm}^{-1}$ .

However, the influence from  $\mu_a$  and  $\mu_s'$  variations on DTOF profiles are quantitatively different. The  $\mu_a$  variation influences more significant and more on late time range of DTOF, whilst the  $\mu_s'$  variation have relatively even influences one different time range of DTOF. This leads to the uniqueness of the results based on TD measurements.

The positive correlation can be elaborated by moments theory. Considering the DTOFs obtained from semi-infinite media with large source-detector distance  $\rho$ , their second central moment can describe the width of DTOF curves. The following equation about variance stands:

$$V = \langle t^2 \rangle - \langle t \rangle^2 = \frac{\rho}{4c^2} \sqrt{\frac{3\mu_s'}{\mu_a^3}} \quad (3.4)$$

It is clear, if  $V$  is constant for a given DTOF,  $\mu_a$  and  $\mu_s'$  must both increase or decrease. However, since it is the cubic term of  $\mu_a$  in the denominator, a small percentage variation of  $\mu_a$  must be compensated by a much larger percentage variation of  $\mu_s'$ , to maintain the DTOF profiles.

### The SeTD integration

Given the opposite correlations of  $\mu_a$  and  $\mu_s'$  in time domain and space domain, a new methodology, i.e., Space-enhanced Time Domain (SeTD) method is purposed in this thesis to facilitate the quantification of scattering and absorption with high accuracy and to create a novel modality of NIRS technique for tissue diagnosis. The SeTD method attempts to combine CW-NIRS and TD-NIRS modalities by effectively integrating the complementary information in space domain and time domain, as to realize the higher accuracy on  $\mu_a$  and  $\mu_s'$  retrieval and to increase the sensitivity and applicable detectability with the sense of low photon count.

For all problems involving forward modelling and inverse validation, the process to obtain the optimal results (absolute quantities of  $\mu_a$  and  $\mu_s'$ ) from the measurements always contains three steps, or more precisely speaking, three levels: *Data-level*, *Feature-level*, and *Decision-level*.

(1) For the conventional modalities like CW-SRS and TD, in the *data-level* the measurement data were obtained in different forms, i.e., DTOFs for TD and SRACs (Space-resolved Amplitude Curves) for CW-SRS / SD, respectively. As shown in Fig. 3.6:

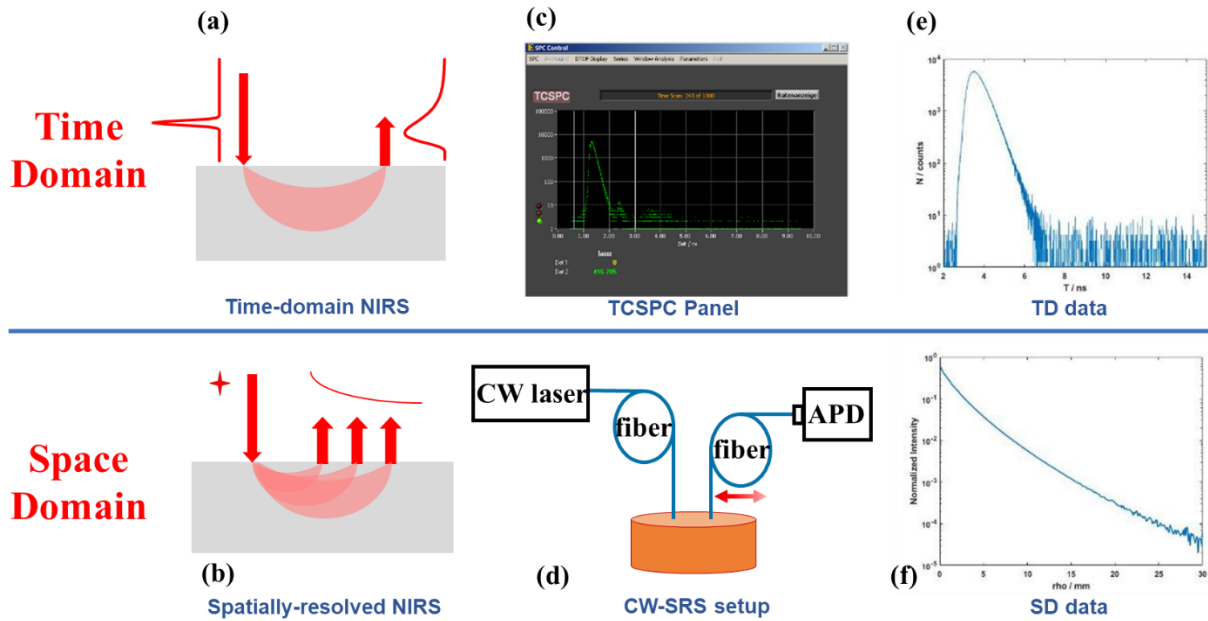


Fig. 3.6: Data-level of TD and CW-NIRS modalities. (a) and (b) refer to the principles of TD and CW-NIRS measurements; (c) and (d) refer to the data acquisition manners of TD and CW-SRS systems; (e) and (f) refer to the data forms in TD and SD.

It can be seen in Fig. 3.6 (e) and (f) that DTOFs as TD data and SRACs as SD data have apparently different forms of data. DTOFs contain time-resolved photon counting numbers whereas SRACs contains space-resolved light amplitude levels. The choice of data types profoundly influences the ability of reconstruction of optical properties. The data in single domain are merely the unilateral observations of the optical phenomena (absorption, scattering, etc.) within the media and can hardly reflect the whole picture, thus the optical properties to recover and the accuracy level to achieve must be well-defined before the choice of data types and their underlying measurement modalities. Meanwhile the noise level and noise model in different data types also need to be considered.

(2) After the data acquisition, the next level – *feature-level* – involves the feature recognition. Feature recognition here denotes how the features originated from absorption and scattering properties of the measured subjects will be recognized by the underlying physical models. The features that absorption and scattering project to the data in TD and SD have already been discussed in the earlier part of this section, as shown in Fig. 3.4 and 3.5. A forward physical model that can quantitatively explain these features shall be selected in this level. By comparing the model simulations and the measurements, the absorption and scattering properties can then be quantified by analyzing their features. The physical models here can be an analytical model like diffusion equation or a numerical model like Monte-Carlo simulations. As illustrated in Fig. 3.4 and 3.5, the characteristics of absorption and scattering effects

projected on time domain and space domain, i.e., the features of  $\mu_a$  and  $\mu_s'$  can be then evaluated and recognized by the proper physical models.

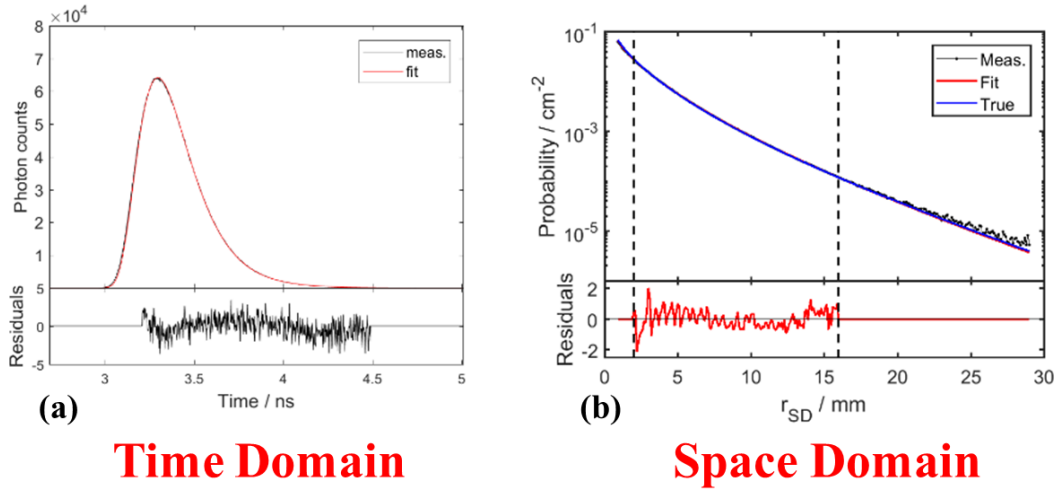


Fig. 3.7: Feature -level of TD and CW-NIRS modalities. (a) the feature recognition process of fitting DTOFs from measurement and MC model in time domain; (b) the feature recognition process of fitting SRACs from measurement and MC model in space domain.

Figure 3.7 gives the examples of the processes of feature recognition based on TD and SD data. In Fig. 3.7(a), the measured DTOF (black curve) is fitted with a simulated DTOF (red curve) from Monte-Carlo method after the convolution with IRF. The features from absorption and scattering will be recognized through the process of minimizing the discrepancy between the measurement and the model simulation, as represented by the residuals underneath the curves. Similarly, in Fig. 3.7(b), the measured SRAC (black curve) is fitted with a MC-simulated SRAC (red curve) within the  $\rho$  range of 2 to 16 mm. And by minimizing the residuals (red lines underneath), the feature from absorption and scattering could be recognized to quantify the optical parameters of interest.

(3) The *decision-level* involve the algorithms which are responsible to decide the final results of the desired optical properties values. The criteria must be established to determine that **(I)** under which conditions the quantities of optical parameters (e.g.,  $\mu_a, \mu_s'$ ) are optimal and reflect the true values to the best extent; and **(II)** along with which path the optimal solution can be retrieved in the fastest way. Typically, an objective function, sometimes referred as loss function, is used as the criteria to define (I), and various advanced gradient descent optimization algorithms, such as Momentum, Nesterov accelerated gradient (NAG), Adagrad, Adadelata, and Adaptive Moment Estimation (Adam) have been developed in the computer science community to accelerate (II), which is beyond the scope of this thesis.

In this thesis, the classical and most effective objective function, the  $\chi^2$  function, is used as the criteria to determine the quality of the fitting between measurements and simulations based on underneath physical models. The  $\chi^2$  function quantify the discrepancy between the measurement and the model forward simulation, by considering:

$$\chi^2 = \frac{1}{n-2} \sum_{i=1}^n \left( \frac{m_i - s_i}{\sigma_i} \right)^2 \quad (3.5)$$

where  $m_i$  and  $s_i$  are the measurement and the model simulation, respectively. Subscript  $i = (1 \dots n)$  represent the time channels in TD-NIRS modality, and the source-detector distance steps in SD-NIRS modality.  $\sigma_i$  is the standard deviation of  $m_i$ , to describe the noise. The denominator  $(n-2)$  is the degrees of freedom of the inverse model applied, given the 2 fit parameters  $\mu_a, \mu_s'$ .

The process of searching for the optimal solution will then be turned to find the best  $(\mu_a, \mu_s')$  values combination which lead to the objective function  $\chi^2$  be minimal. As an example, shown in Fig. 3.8, the searching process starts from an initial guess of  $(\mu_a, \mu_s')$  combination at  $(16.93, 0.1408) \text{ cm}^{-1}$ . And as shown in the left subplot, the model simulation based on the initial guess fits not well with the measured DTOF curve and cause high residuals and large  $\chi^2$  value. Along with the process goes on, the algorithm finds the path with decreasing  $\chi^2$  values as shown as green points and lines, and eventually ends up at the optimal solution as  $(\mu_a, \mu_s') = (13.81, 0.1256) \text{ cm}^{-1}$  with the much-improved fitting performance and lowest  $\chi^2$  values as shown in the right subplot. The final results are close to the ground true values indicated as the red cross in the center.

In the *decision-level* the decision of optimal results shall only be made when the objective function reaches its global minimum.

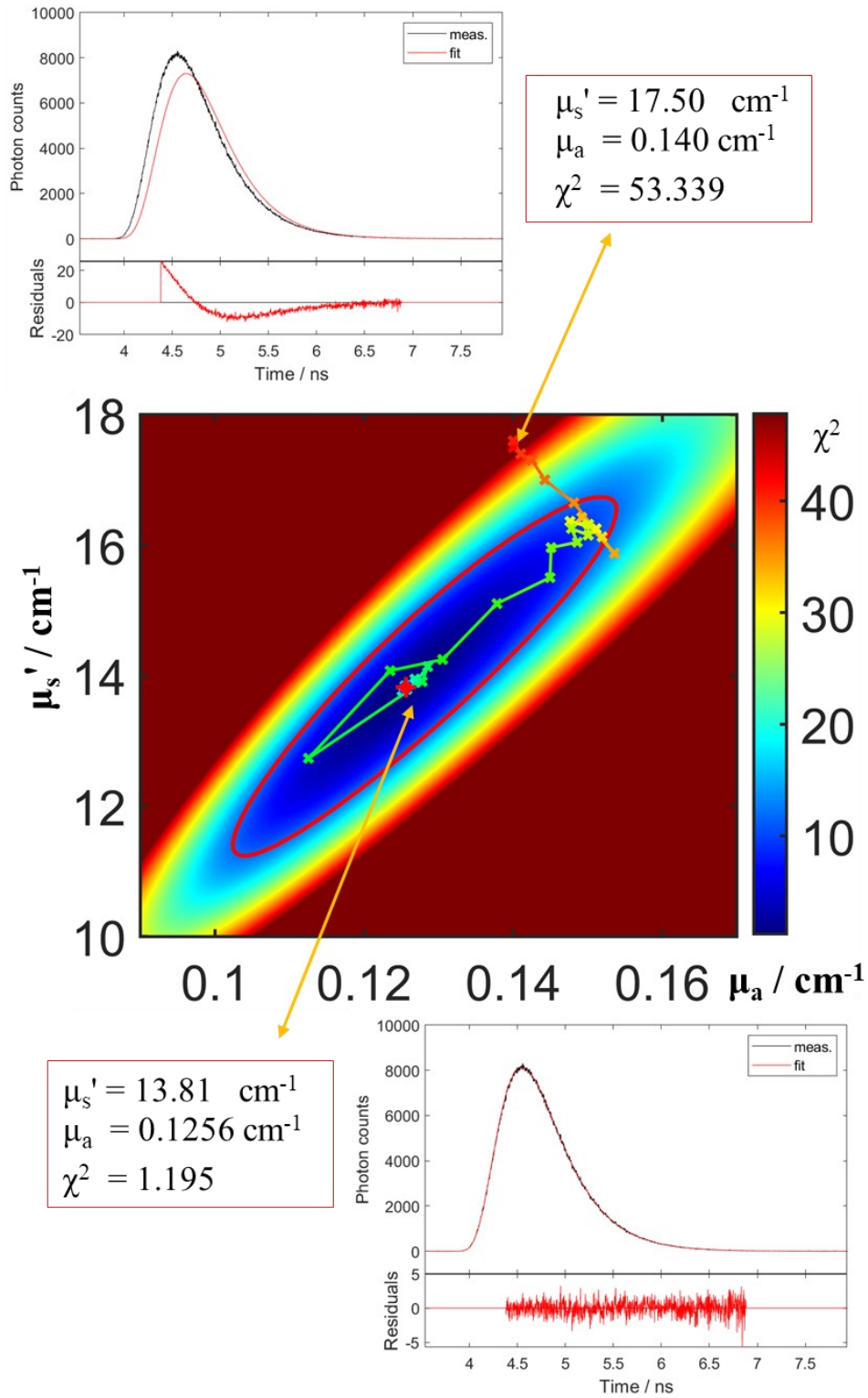


Fig. 3.8: Decision-level of TD modalities. The  $\chi^2$  map in the  $\{\mu_a, \mu_s'\}$  space denotes the  $\chi^2$  distribution of fitting model simulations of various  $(\mu_a, \mu_s')$  combinations with the measurements of  $(\mu_a, \mu_s')$  values at ground truth pointed at the red cross point. The left subplot is the initial fit performance at  $(16.93, 0.1408)$   $\text{cm}^{-1}$  while the right subplot is the fit performance of the final optimal result at  $(13.81, 0.1256)$   $\text{cm}^{-1}$ . The green points and lines indicate the fitting progress from the initial to the final. The red contour line are the positions where  $\chi^2 = 3 \chi_{\min}^2$ .

Overall, for all the conventional modalities like CW-SRS and TD, the optimal results are obtained after the above-mentioned three steps. The problem to be solve can be conceptually described as follow:

**Primal Problem (P\*):** To retrieve  $\mu_a$  and  $\mu_s'$  by minimizing the discrepancy between measurements and models:

$$\mu = \arg \min \{ \mathcal{F}_{\text{model}} - \mathcal{F}_{\text{meas}} \} \quad (3.6)$$

where  $F_{\text{model}}$  and  $F_{\text{meas}}$  indicate the physical model and measurements, respectively.

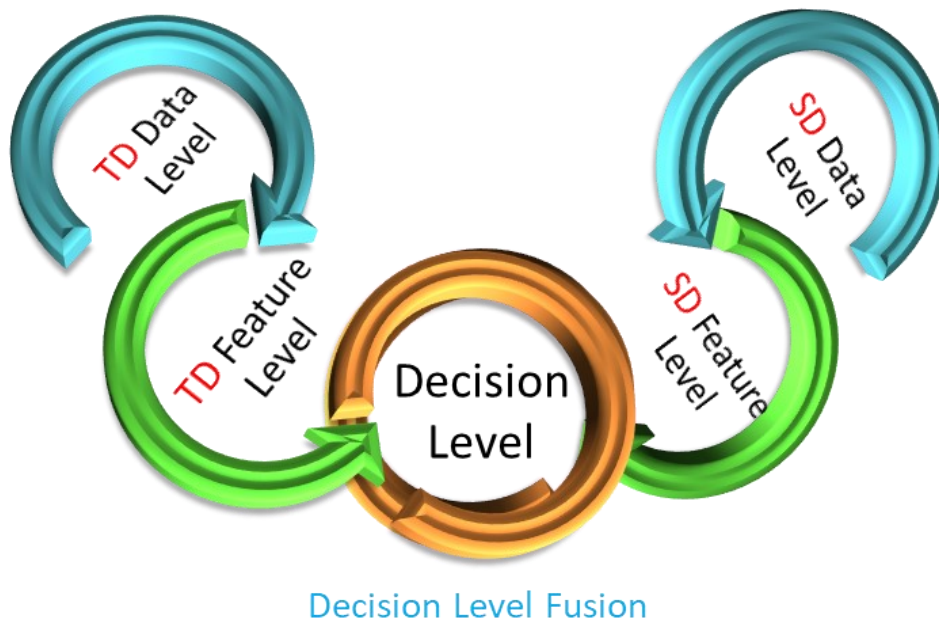


Fig. 3.9: The SeTD integration on the decision-level. TD and SD information's fusion.

The opposite correlations of  $\mu_a$  and  $\mu_s'$  in TD and SD shows on the *feature-level* can be advantageously used to improve the performance on  $\mu_a$  and  $\mu_s'$  retrieval. One attempt is to directly combine the TD and SD data at the *data-level*, as the “TD global fit” method which will be described in Chapter 4. However, on the *data-level*, the different features originated from absorption and scattering cannot be effectively integrated with the proper weights. On the *feature-level*, it is difficult to integrate the information from different domains. Therefore, The SeTD integration is the TD and SD information's fusion on the *decision-level*.

In the scheme of SeTD method, the primal problem (P\*) would be circumvented by considering its dual problem (D\*) in  $\{\mu_a, \mu_s'\}$  space:

**Dual Problem (D\*):** To minimize the correlation between  $\mu_a$  and  $\mu_s'$  by integrating TD and SD knowledge in the  $\{\mu_a, \mu_s'\}$  space

$$\mu = \arg \sup \rho(\mu_a, \mu_s') |_{\{\mu_a, \mu_s'\}} \quad (3.7)$$

Equation (3.7) reveals the kernel idea of the SeTD method: Unlike the conventional modalities which always approach the optimal results by minimizing the discrepancy between models and measurements, the SeTD method approaches the optimal results by minimizing the correlation between the features of absorption and scattering. In other words, the conventional methods solve  $P^*$  through looking for the minimal  $\chi^2$  (as in equation 3.5) in  $\{\mu_a, \mu_s'\}$  space in a single domain, whereas the SeTD method solves  $D^*$  through find minimal *Perason* correlation coefficient  $\rho(\mu_a, \mu_s')$  by efficiently balancing the information from multiple domains. A new  $\chi^2$  function that integrating information from multiple domains is established to balance the weights of domains, as the form of Generalized *Lagrangian* Function (GLF)  $\chi^2_L$ :

$$\chi^2_L = \chi_T^2 + \lambda \chi_S^2 \quad (3.8)$$

where  $\chi_T^2$  and  $\chi_S^2$  are the  $\chi^2$  objective function from time domain and space domain, respectively.  $\lambda$  is the weight multiplier to be optimized.

It should be stressed that  $\chi^2_L$  is not the objective function for SeTD method. The optimal  $\mu$  combination is reached under the condition of minimizing  $\rho(\mu_a, \mu_s')$  in  $\{\mu_a, \mu_s'\}$  space. Thus Eq. (3.7) is subject to Eq. 3.8 by adjusting  $\lambda$  to integrate the weights of different domains.

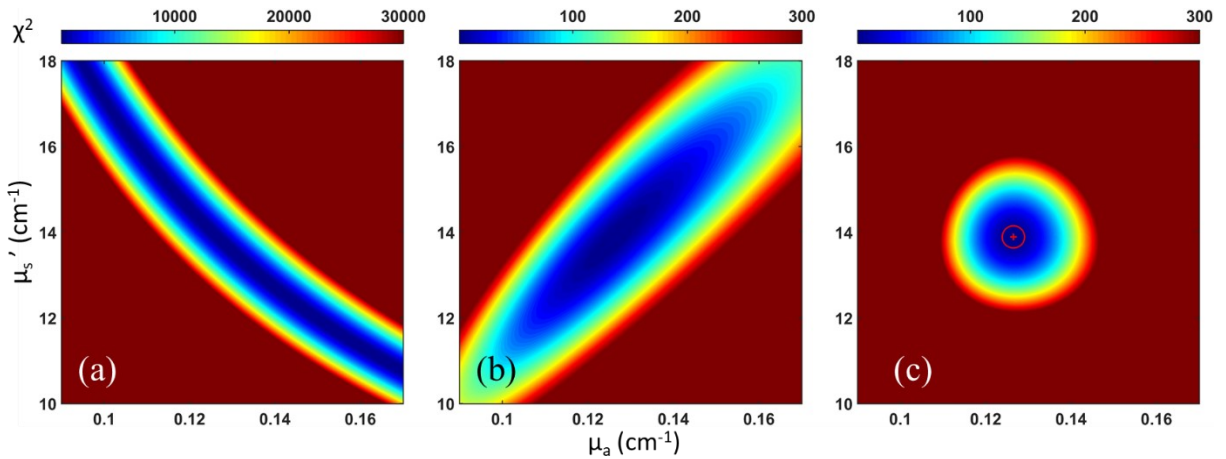


Fig. 3.10. Schematic illustration of the decision-level fusion via the fittings of a homogeneous medium measurement with MC simulations. (a)  $\chi_S^2$  distribution for SRACs fitting, (b)  $\chi_T^2$  distribution for DTOFs fitting, (c) final  $\chi_L^2$  distribution when  $\lambda$  is optimized to minimizing the correlation; Red cross is the optimal solution.

As illustrated by Fig. 3.10, the measurements of a homogeneous medium are fitted with Monte-Carlo simulations. Fig. 3.10(a) is the  $\chi_S^2$  distribution by fitting SRACs with MC simulations of all  $(\mu_a, \mu_s')$  combinations and Fig. 3.10(b) is the  $\chi_T^2$  distribution by fitting DTOFs with MC simulations of all  $(\mu_a, \mu_s')$  combinations. The optimal results for TD and SD methods

will be obtained at the position of minimal  $\chi^2$  value of Fig. 3.10(a) and (b) respectively. On the other hand, in Fig. 3.10(c) the optimal results for SeTD method are reached when the features of absorption and scattering is decoupled, i.e., the *Perason* correlation coefficient  $\rho(\mu_a, \mu_s')$  is minimized at contours of the same  $\chi^2$  values. The weight multiplier  $\lambda$  is optimized along the process to adjust the weights of SD and TD information.

The theoretical ground of the SeTD method can be elaborated with the help of optimization theory. The Primal Problem is equivalent to the dual problem under the fact that the physical process of absorption is independent to the physical process of scattering. Thus, the features of them should be decoupled in a certain spatio-temporal space so that the  $(\mu_a, \mu_s')$  combination at the minimal  $\chi^2_L$  position can optimally reflect the true values. The criteria of minimizing the discrepancy between measurements and models in individual domains can be then transferred to the criteria of minimizing the correlation of the unknown but independent optical parameters in the artificially mixed domain.

### 3.3 Instrumentation

In this section, the overview of the instrumentation and photonic components of diffuse optics system will be presented, focusing particularly on the time domain modality. The light sources, detectors, timing electronics, and light guides will be briefly introduced. A crucial factor to the accuracy for TD systems, IRF (Instrument Response Function), will also be discussed.

#### Pulsed Light Sources

To build up a time domain system for diffuse optics and tissue diagnosis measurements, at least four requirements of the suitable laser source must be met. First, the emission wavelengths shall fall in the “near-infrared therapeutic window” (650 to 1000 nm). Secondly, the pulse width, usually evaluated by FWHM (full width at half maximum), shall be as narrower as possible, so that the time resolution will not be hampered. Thirdly, the repetition rate shall be sufficiently high (typically  $\geq 20\text{MHz}$ ) to allow the compatible acquisition time for *in-vivo* measurements. And finally, the appropriate and stable emission power shall be maintained to allow a stationary measurement and a suitable SNR, and to follow the requirements of safe laser exposure for *in-vivo* measurements. The laser systems fulfilling these requirements are listed in below.

(1) Ti:Sapphire Lasers: this kind laser system uses self mode-locking technique and can therefore achieve the FWHM  $\sim 100$  fs. The repetition rate can reach up to 100 MHz, and the average output power can be up to 1 W. The wavelength can be tunable from 600 to 1000 nm.

The major disadvantages of this laser system are its expensive cost and bulky volume, which makes it unsuitable to the clinical measurements.

(2) Pulsed diode lasers: also called as semiconductor laser. This kind lasers use edge emitting diodes in gain switching mode to launch light pulses. The repetition rate can reach up to 100 Mhz. The typical values of FWHM and average output power are 150 ps and 10 mW. Due to the inherent mechanism of gain switching mode, the correlation between power and pulse width cannot be avoided, indicating that increasing power will inevitably lead to the increasing FWHM.

A special type of pulsed diode laser, vertical cavity surface-emitting laser (VCSEL), is worth to mention for its compactness and integrability. It is possible to host many VCSEL sources in a dense arrangement so that to increase the overall output power while maintain the pulse width. The major advantages of VCSEL and other pulsed diode lasers are their low cost and portability.

(3) Pulsed fiber lasers: the laser systems with fiber-based oscillator and amplifier raise on the market for its robustness, relative compactness, and broad spectrum. The pulsed fiber lasers based on supercontinuum generation can have a large, continuous spectral range (400 to 2000 nm) and a total average output power up to 10 W integrated over the whole spectrum. The pulse FWHM can go down to 10 ps and the repetition rate is in the order of tens of MHz. The supercontinuum fiber laser often combines with spectral filter such as acousto-optic tunable filters (AOTF) to realize the tunable wavelength with high flexibility. The switching between wavelengths can occur within a few  $\mu$ s. fiber-based Supercontinuum laser with spectral filters is the major laser system used in the experiments of this thesis.

## **Detectors**

The performance of a detector for time domain photon counting is determined by four factors: photon detection efficiency, active area, transit time spread (TTS), and response shape (background noise, afterpulsing, and response tail). Photon detection efficiency decides the photon collection effectiveness of a detection chain. Active area decides the effective collection area of light harvesting. Transit time spread dominantly determines the time resolution and IRF width. And response shape influences the performances in the accuracy of recovering the optical properties and in the investigation of deeper regions of heterogeneous media. Several representative detector types are presented in below.

(1) Photocathode-based detectors. PMT (photomultiplier tube), MCP-PMT, and Hybrid PMT are in the same family of photocathode-based detector which always contains a photosensitive surface and a vacuum tube. MCP-PMT is known as the microchannel-plate PMT that offers a much shorter transit time spread. And Hybrid PMT combines photoelectron

emission from photocathode with the amplification from avalanche diode and provides a relative short transmit time spread as well. Nowadays the typical active area diameter for PMTs can be more than 10 mm. Regarding TTS, the traditional PMTs is about 140 to 200 ps, MCP-PMTs can be as low as 20 ps, and hybrid PMTs is usually about 50 ps. One striking advantage of hybrid PMT compared to all other detectors is its clean response shape, which allows the high resolution in the tail of response curves and subsequently the deeper region properties' accuracy. Hybrid PMT is the major detector used in the experiments of this thesis.

(2) Single-photon avalanche diodes (SPAD). Solid-state semiconductor detectors representing by SPAD have high photon detection efficiency, typically two orders of magnitude than PMTs, but suffer from the very small active area (diameter usually up to 100  $\mu\text{m}$ , i.e., three orders of magnitude smaller than PMTs). Since diffuse optics intrinsically needs high photon collection capacity to maximize light harvesting from all possible diffuse directions, the small active area is the major disadvantage and bottleneck of SPAD. Notwithstanding SPAD has quite small TTS down to 20 ps, the response shape of SPAD always has the long tail due to trapped carriers of the previous avalanche breakdown. This feature also heavily limits the SPAD's ability to recovery optical properties related to the exponential decay tails of DTOFs, especially for the deep regions of tissues. The cost and compactness of SPAD are advantageous to other detectors, as well as its strong resistance to the high light exposure.

Figure 3.11 gives a comparison of the response shapes of HPM detectors and a SPAD detector, illuminated by a same laser source.

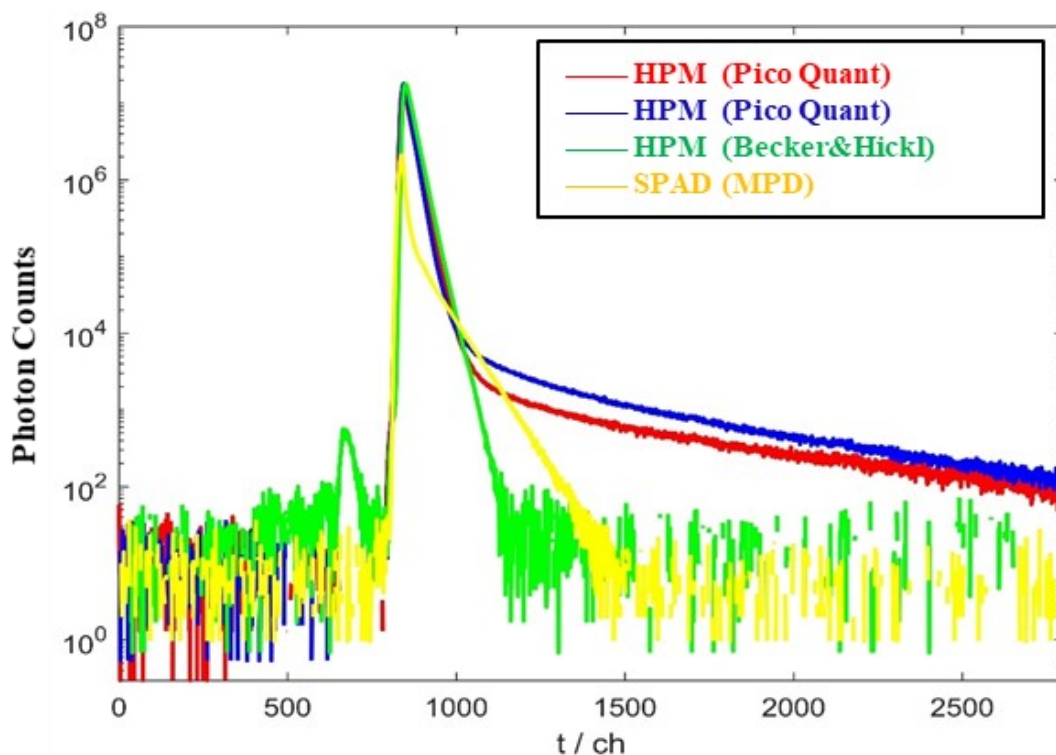


Fig. 3.11. Comparison of the response shapes of HPM detectors and an SPD detector under same source. The response shapes of HPMs vary among different companies. The SPAD has the narrowest FWHM while suffering a long decay tail.

(3) Silicon photomultipliers (SiPM). SiPM can be envisaged as a structure of an array of many SPADs and have risen interests of diffuse optics community just in recent years as a candidate detector with large active area like PMTs and low cost like SPADs. SiPMs can detect very high photon count rates meanwhile with high temporal resolution (down to 60 ps). The major problem of SiPMs is its high background noise and afterpulsing in the response shape. The relevant advances on SiPMs are ongoing right now and could make SiPMs become the most promising detector in the future [89].

### **Timing electronics**

In time domain diffuse optics and many other fields such as fluorescence, Time-correlated Single Photon Counting (TCSPC) is the key technique and has been widely used for years. A well-written guidebook about this technique can be found at [90]. In this section only a brief introduction and a few cautionary notes about the applications in diffuse optics are discussed.

In TCSPC system, unlike CW modality which records light intensity, it is the time-stamp marking the arrival time of every detected photon to be recorded, to accumulate a histogram of photon numbers, and thus to recover the time-resolved curve. For low light levels, which is the normal case in diffuse optics of tissue imaging, the constant-fraction discriminator (CFD) is applied to determine the arrival time of the incoming pulses regardless their amplitude. The arrival time of every detected pulse can then be addressed in two different ways.

(1) TAC-ADC. A time-to-amplitude converter (TAC) will convert time into voltage amplitude, which is further processed by an analog-to-digital (ADC) converter to be assigned to a memory address in which the event is added.

(2) TDC. The process directly from time to digital will be carried out in digital form by a time-to-digital converter (TDC) with the use of digital counters and suitable delay logic gates chain.

Both ways have advantages and disadvantages. While they achieve similar performances at present in practice. In real applications, one must pay attention on several potential issues when deploying TCSPC electronics: differential nonlinearity (DNL), pile-up effect, and count loss due to dead time effect.

(1) Differential nonlinearity (DNL) denotes the signal distortion due to the unevenness of time channels. The distortion will act as the fluctuations on the DTOFs and result more or less photon pulses detected in different time channels. An effective way to remove DNL is to

measure a reference signal with a continuous light source, and then divide DTOFs by the reference. Since the reference has the same DNL errors as the DTOFs, the division may remove the DNL errors.

(2) Pile-up effect is caused by detection oversaturation when in one pulse event period a second photon appears and is not recorded. The effect leads to curve distortion and occurs only at much higher count rates. It should be prevented by avoiding too high count rate at any time channels.

(3) Count loss due to dead time effect is different with pile-up effect. Such count loss is due to the long dead time which extend more than one pulse recording event period. While the pile-up effect usually occurs at the late part of an event period, the count loss due to dead time effect happens at the early part. The “dead time compensation mode” that prolong the macro recording time can compensate the loss to some extent.

### **Light Guides**

In order to deliver light pulses onto the medium with minimal pulse broadening and collect re-emitted photon with high collection efficiency, a proper light guide system shall be considered carefully as well. The most-often used light guides in diffuse optics is optical fibers. Several features need to be reviewed when selecting fibers: numerical aperture (NA), core diameter, and refractive index profile.

The fibers connected to light sources usually do not require high NA and high core diameter since a highly coherent source, which is usually the case for TD diffuse optics, can be easily collimated. The choice for the source fiber shall be focus on the pulse broadening caused by temporal dispersion. The Graded index fibers (with dispersion  $\leq 1$  ps/m) is the ideal choice in this sense.

The fibers connected to detectors are responsible to the photon collection under very low light level. High NA and large core diameter play the important roles here to maximize light harvesting. The fiber bundles of few millimeters core diameter step-index fibers can achieve higher NA (up to  $\sim 0.5$  to  $0.6$ ) under the cost of bigger temporal broadening. A recent new large core graded index fiber with around  $100 \mu\text{m}$  core diameter and  $\text{NA} = 0.22$  pave the way for a better tradeoff between photon collection efficiency and temporal dispersion.

### **Instrument Response Function (IRF)**

The instrument response function (IRF) summarized all instrumental influences on final time domain signals except the response from the subject diffuse medium. IRF represents the

overall response of all components in the measuring instrumentation. The constitution of IRF  $I(t)$  can be expressed as follow:

$$S(t)=L(t)*F_l(t)*M(t)*F_d(t)*D(t)=I(t)*M(t) \quad (3.9)$$

Where  $S(t)$  is the final time domain signal, and  $L(t)$  is the light pulse ignited from the source.  $F_l(t)$  and  $F_d(t)$  are the responses from the fibers connected to source and detector.  $D(t)$  and  $M(t)$  denote the response of the detector and the diffuse medium. All instrumental components and the medium itself will contribute to the temporal broadening of the initial light pulse  $L(t)$ . The broadening effects are considered as the convolution (\*) of the corresponding characteristics, which include laser pulse shape, TTS of detector, and the temporal dispersion from fibers, *etc.* The IRF is then defined, according to the commutative property of convolution operation, as  $I(t)$  to represent the overall response of the instrumentation system.

IRF is essential to the time domain measurements since what is really under investigation is the characteristics in the response from diffuse medium  $M(t)$ . Eq. (3.9) provides a way to describe any time domain measurement  $S(t)$  by just two terms. Ideally, IRF should be independent to the subject medium and be constant in time. The most desirable IRF should be a delta function so that the instrumentation would cause no artefacts on the final signal. However, in the TD inverse problem, the theoretical simulations will always need to convolute with the IRF before comparing with the measurements. Thus the precise measuring on IRF directly determines the accuracy and time resolution of the final results.

### 3.4 Phantoms

Phantoms are critical for all diagnostic imaging systems. The phantoms that mimic the human or animal tissues have the functions of testing the feasibility of the systems, performing the assessment protocols of instruments, comparing performances between different systems, and optimizing desired signals. For diffuse optics in tissue diagnosis, an ideal phantom should fulfil the requirements that: (1) having the proper optical properties ranges close to the actual tissues, (2) having the well-known geometries (homogenous, heterogenous/with inclusions, or layered) to mimic the real tissue structures, (3) with the easily *on-site* tunable optical properties, (4) the geometry and optical properties are stable and durable, and (5) can be reproducible. A comprehensive review about the tissue simulating phantoms for optical spectroscopy has been given in [91]. In this section, several representative phantoms used in this thesis that focusing on mimicking human brain tissues are described and their advantages and disadvantages are discussed.

## Polydimethylsiloxane (PDMS)

Polydimethylsiloxane (PDMS) has been widely used to fabricate many materials with tissue-like optical and physical properties recently [92]. PDMS solids are mechanically and chemically stable in very long time period and free of contamination. The processability and optical transparency of PDMS allow its optical properties (absorption, scattering, and refractive index) to be adaptably tunable.

PDMS is added into the solution of white rutile  $\text{TiO}_2$  powder and Toluene and the solution is fully mixed for days. The Toluene will be evaporated from the mixture and then the solution will be baked for slow curing. The concentration of  $\text{TiO}_2$  in the solution decides the scattering properties of the final solid phantoms. One investigation on the linear relation between the  $\text{TiO}_2$  concentration and the  $\mu_s'$  values is shown in Fig. 3.12.

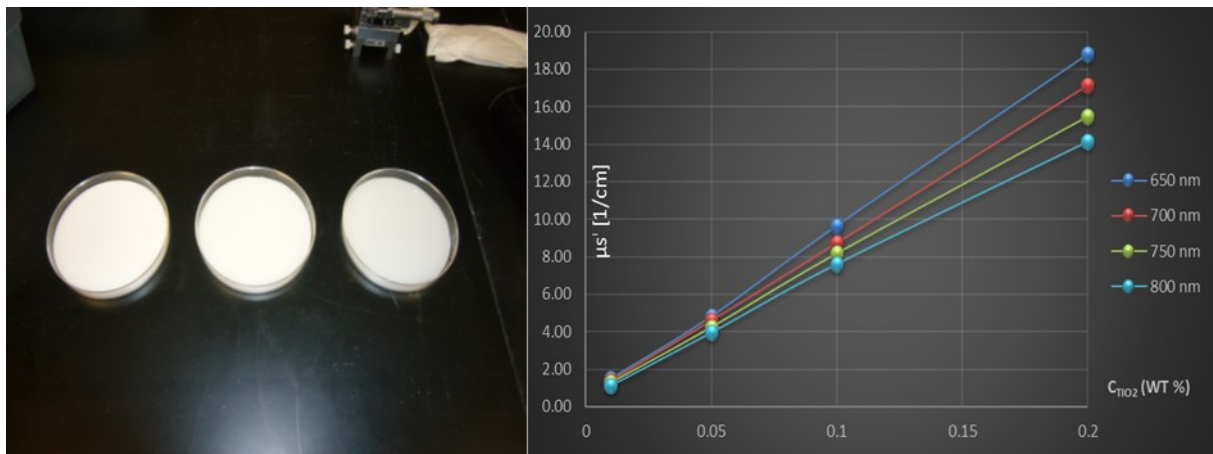


Fig. 3.12. The  $\mu_s'$  trend with respect to  $\text{TiO}_2$  Concentration. Left: PDMS phantoms with  $\text{TiO}_2$  concentration  $C_{\text{TiO}_2}$  (wt %) = 0.01, 0.05, 0.1. Right: The relation between  $\text{TiO}_2$  concentration and  $\mu_s'$  values in 4 wavelengths: 650, 700, 750, and 800 nm.

The consistency on different batches of PDMS phantoms validate the reliability and homogeneity of the phantom. Solid PDMS/ $\text{TiO}_2$  composites are promising tissue-mimicking materials for performance standards to validation measurements owing to its durability, reproducibility, and stability.

## Solid Epoxy Resin Phantoms

Epoxy Resin material is another solid but more classical phantom that has been widely for protocol designs and standardization in diffuse optics [93,94]. These phantoms use epoxy resin as the base material,  $\text{TiO}_2$  as the scatterer and toner as the absorber. The recipe and preparation process are presented by *Firbank et al.* [95] and *Swartling et al.* [96]. The ratio of scatterer and

absorber concentrations is adjusted to realize the gradual changes of both  $\mu_a$  and  $\mu_s'$ . A set of phantoms of  $\mu_a \times \mu_s'$  matrix can be realized by the resin phantoms and the phantoms with the relevant properties values within the optical properties range of human brain tissue has been produced and tested.

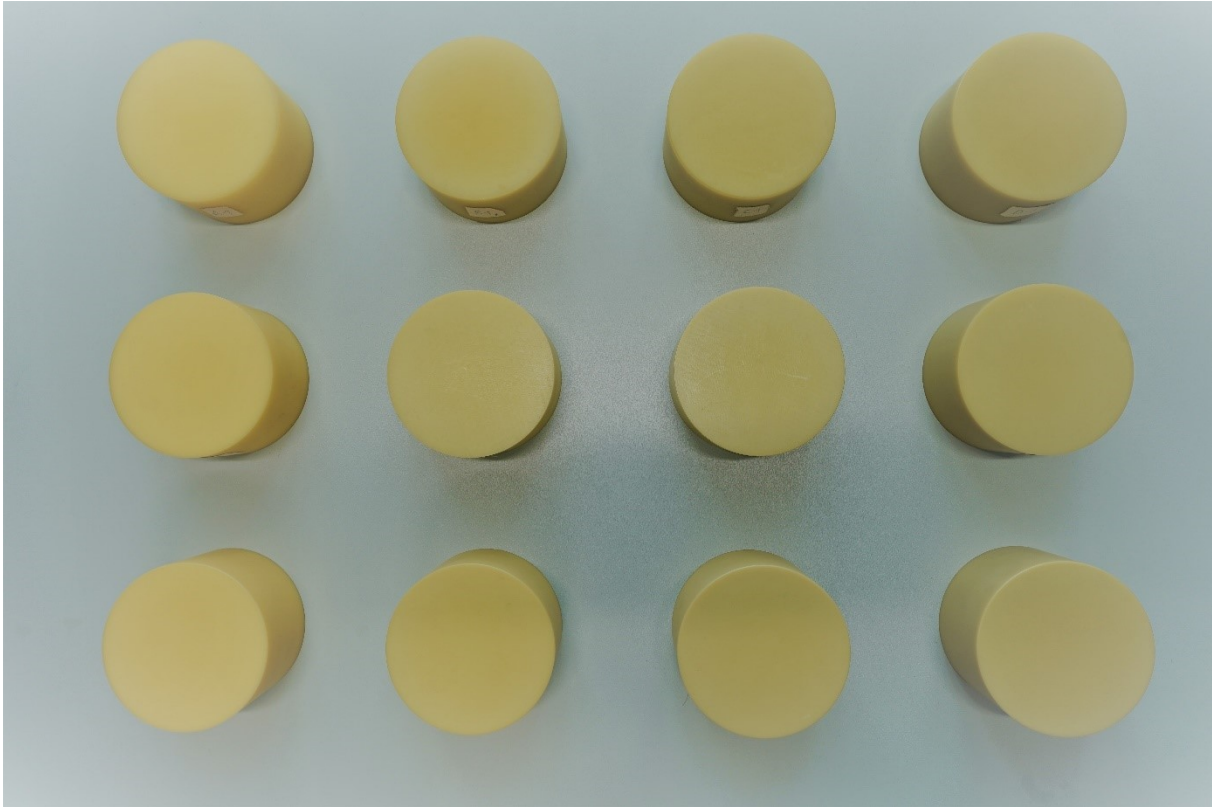


Fig. 3.13. A solid epoxy resin phantom matrix with the same scattering coefficients at each row and the same absorption coefficients at each column.

One of the main problems is this kind of phantoms, and many other solid phantoms, do not have reliable reference nominal values on optical properties since many uncontrollable factors in the producing process substantially influence the final properties and thus the quantities of optical properties cannot be simply calculated from the concentrations of absorber and scatters. The characterization of these phantoms needs to be carefully inspected before using them. Meanwhile, the cumbersome solid phantoms are also very difficult to have tunable optical properties.

### **Liquid Intralipid Phantoms**

Liquid phantoms are the most common tissue-mimicking photon for investigating photon migration. Intralipid is used as the scatterer and inks/dyes as absorber. The liquid mixtures of intralipid, ink, and water are inexpensive, easy to reproduce, and have strong flexibility. Most

importantly, it has been shown by many studies [97,98] that the liquid intralipid phantoms through precise preparation and characterization can have well-defined nominal values on  $\mu_a$  and  $\mu_s'$ , retrieved from the concentrations of the components in the solution.

The high flexibility of liquid phantoms has two aspects: changes of optical properties and construction of inhomogeneous geometries. The former one requires the amounts of components to be mixed with accurate weighing, and the latter one needs the proper container and potentially the thin membranes as the layer separators.

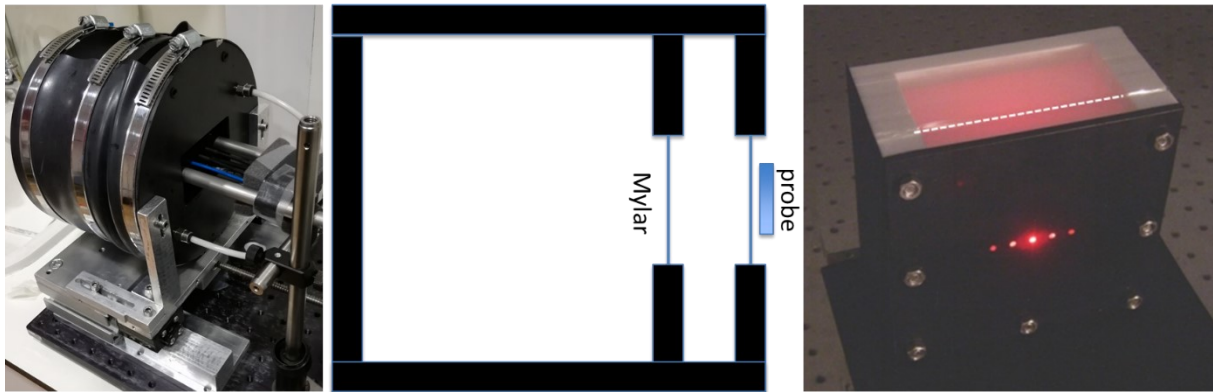


Fig. 3.14. Examples of liquid phantoms' containers to realize the layered structures. Photo in right is adapted from [99] with permission from © The Optical Society.

Figure 3.14 gives several instances to show the real structure of the liquid intralipid phantom's containers used in this thesis. The liquid solutions having different optical properties were separated by Mylar films which have negligible influence on the photon diffusion. At the moment, the liquid intralipid phantoms are the optimal and maybe the only choice for the reflectance measurements on layered structures.

On the other hand, liquid phantoms are always difficult to store, easy to lose durability, and struggling on reproduce the same properties based on different preparations condition or different material batches. And since liquid phantoms usually requires thin membranes to separate laser/detectors and liquids, the light guide effect and stray light along the membrane surface also need to be carefully addressed and overcome.

# 4

## **Space-enhanced time-domain diffuse optics in homogeneous structures**

**This chapter was previously published in:**

Lin Yang, Heidrun Wabnitz, Thomas Gladysz, Rainer Macdonald, and Dirk Grosenick, “Spatially-enhanced time-domain NIRS for accurate determination of tissue optical properties”. In: *Optics Express* **27**, 26415-26431 (2019) ©.

**Contributions to this chapter:**

I initialized the research idea, concretized the concept and methodology, and planned the measurement campaign. I conducted and participated in all measurement activities and data analyses. The original manuscript and the amendments before and after the peer-review are also conducted by me, with the suggestions and reviews from co-authors.

**These co-authors contributed to this chapter:**

H.W. helped to perform the time domain measurements and interpretate results, and gave revision suggestions.

T.G. helped to exercise the space domain measurements and analyze the results.

R.M. supervised the project and gave the research framework and revision suggestions.

D.G. helped to perform the numerical analysis and result interpretations, contributed to the research plan, and gave revision suggestions.

---

© 2019 *Optical Society of America*. Users may use, reuse, and build upon the article, or use the article for text or data mining, so long as such uses are for non-commercial purposes and appropriate attribution is maintained. All other rights are reserved.

## 4.1 Abstract

A multivariate method integrating time and space resolved techniques of near-infrared spectroscopy is proposed for simultaneously retrieving the absolute quantities of optical absorption and scattering properties in tissues. The time-domain feature of photon migration is advantageously constrained and regularized by its spatially-resolved amplitude patterns in the inverse procedure. Measurements of tissue-mimicking phantoms with various optical properties are analysed with Monte-Carlo simulations to validate the method performance. The uniqueness, stability, and uncertainty of the method are discussed.

## 4.2 Introduction

Near-infrared spectroscopy (NIRS) has become a powerful tool for clinical diagnosis and medical imaging [18], owing to its non-invasiveness, high temporal resolution, and portability. It can reveal the optical absorption property of biological tissues in depth, and thereby has been widely applied for indicating the concentrations of essential biomarkers, e.g., oxy-/deoxy-hemoglobin and cytochrome-c-oxidase in human brain, kidney, and breast [22,100,101]. The advantages of this technology in turn also allow for more sophisticated clinical applications such as neuroimaging, diffuse optical tomography, and tissue oximetry [13,77,102]. By quantifying optical scattering properties, NIRS-based real-time monitoring of many in vivo mechanisms [103,104] (e.g., intracellular oxygen delivery) can also become a feasible future.

Focusing on changes in concentration of oxy- and deoxyhemoglobin in human brain, functional NIRS (fNIRS) has received an enormous amount of attention in decades [105]. This technique studies on hemodynamic and metabolic responses to human brain activities and performs on task-based or event-related experiments. It derives many fruitful ramifications in different fields, e.g., clinical cerebral metabolism [106], cognitive neuroscience [107], and brain-computer interface studies [8].

On the other hand, absolute NIRS measuring methodologies, which aim at retrieving the absolute quantitative values of optical properties in biological tissues and materials instead of changes only, are promoting progress and drawing more and more interest through the years. Absolute NIRS techniques have already been shown to be a valuable tool for non-invasive diagnosis of many pathological tissues such as breast [108], thyroid [109], traumatic brain [79], skin [110], and many others [111]. Specifically, cerebral oximeters based on absolute NIRS have found widespread use. However, most of the devices are empirically calibrated and the accuracy and comparability of results from different devices is insufficient [98]. More

potentials of absolute NIRS require further exploration. By retrieving two essential optical parameters, i.e., absorption coefficient ( $\mu_a$ ) and reduced scattering coefficient ( $\mu_s'$ ), absolute NIRS methods can directly derive the absolute quantities of biomarkers' concentrations, and in particular, oxygen saturation of hemoglobin. In order to obtain absolute values of  $\mu_a$  and  $\mu_s'$ , absolute NIRS methods rely on various measurands, such as spatially resolved (SR) (also termed multi-distance) continuous-wave (CW) amplitude in space-domain (SD) [21], time resolved (TR) photon distribution in time-domain (TD) [34], or demodulation and phase shift in frequency-domain (FD) [84]. The recently introduced technique of interferometric NIRS, which is based on the time-of-flight resolved measurement of coherent light, can also determine absolute values of  $\mu_a$  and  $\mu_s'$  [112,113]. However, although from physics perspective  $\mu_a$  and  $\mu_s'$  themselves are two totally independent quantities, in practice the external characteristics originating from the internal nature of  $\mu_a$  and  $\mu_s'$  are heavily entangled in all above-mentioned measurands. Such entanglement causes that error in one retrieved quantity can manifest as artefacts in the other and reduce the accuracy for both. Therefore, the key issue of absolute NIRS methods is to decouple absorption and scattering in detected signals.

Many analytical models (e.g., diffusion approximation, P-n approximations) and numerical tools (e.g., Monte-Carlo, finite element methods) have been developed to describe photon migration in tissues, nevertheless simultaneous and accurate determination of  $\mu_a$  and  $\mu_s'$  still remains a challenging but promising task. SD approaches suffer from the non-uniqueness [88], while TD and FD approaches have difficulties regarding crosstalk among the unknowns [12] and unsatisfactory performance under low SNR circumstances like short-time acquisition or large source-detector distance [85]. Ambiguity and uncertainty of retrieved optical properties are particularly high in the presence of in vivo noise and perturbations, or in sophisticated heterogeneous structures. Some moment-based spatially-resolved TD attempts [114,115] have already been applied to handle these problems. More practical improvements aiming to increase uniqueness, stability and accuracy for clinical routine implementations of NIRS are crucial.

In this work, a new multivariate method integrating TD and SD techniques of NIRS, namely spatially-enhanced time-domain NIRS, is proposed, and tested for simultaneous quantification of  $\mu_a$  and  $\mu_s'$  in homogenous turbid materials. The method is based on the principle that optical absorption and scattering effects on diffuse reflectance, despite independent, are either positively correlated in TD observations or negatively correlated in SD observations. A similar concept has been indicated by S. Arridge and M. Schweiger in theoretical basis papers [10,116]. Effective mutual complementation of TD and SD information

of photon migration is realized by enhancing and optimizing TD fitting with SD constraints. Thus, a better convergence to the optimal solution in  $\{\mu_a, \mu_s'\}$  space is reachable. We first demonstrate the proof-of-principle of the method by Monte-Carlo simulations. Then the method is validated through experiments of retrieving  $\mu_a$ , and  $\mu_s'$  for a set of solid homogeneous phantoms. The method could be implemented to improve the performance assessment of clinical diffuse optics instrumentation when using tissue simulating homogenous phantoms [117]. And by decreasing uncertainty, spatially-enhanced TD NIRS is capable of coping with in vivo conditions with high noise and perturbations. Especially at large source-detector separations where the low photon appearance is prevailing, as other researchers previously pointed out, it is feasible to use homogenous models to estimate the optical properties of deep regions in heterogeneous layered structures [31], which therefore may allow spatially-enhanced TD NIRS to be implemented for circumventing the influence from superficial tissues.

By measuring a series of solid tissue-mimicking homogenous phantoms, we compared the results of the proposed spatially-enhanced TD method with two conventional TD methods (single-distance TD and Global fitting TD). Considerable improvements regarding uniqueness, stability and uncertainty of the retrieved optical properties are demonstrated.

### 4.3 Theory

The contributions from absorption and scattering properties of turbid media on the diffuse reflectance are entangled in TD and SD with different ways. Effective complementation of TD and SD information can improve the retrieval performance of optical properties.

#### 4.3.1 Positive correlation in time domain

In TD, time-resolved diffuse reflectance profiles are measured as histograms that represent distributions of times of flight (DTOF) curves. They are obtained by recording the time of flight from source to detector of many (typically 105 to 106) photons, by means of the time-correlated single photon counting technique. For homogeneous turbid media, the shape of the DTOFs depends on  $\mu_a$ ,  $\mu_s'$  and  $\rho$  (source-detector distance) [81]. An increase in  $\mu_s'$  or  $\rho$  broadens the DTOF, while an increase in  $\mu_a$  narrows it. In other words, at constant  $\rho$ , the contributions from  $\mu_a$  and  $\mu_s'$  are positively correlated with each other on DTOFs. The influence of  $\mu_s'$  and  $\rho$  on the DTOF shape is given by the product  $\rho^2\mu_s'$  [118]. This means a nearly identical DTOF shape (disregarding amplitude) can be obtained if an increase in  $\mu_s'$  is balanced by a decrease in  $\rho$ . On the other hand,  $\mu_a$  determines the DTOF slope at later time range of DTOF.

The uncertainty of  $\mu_a$  obtained by TD fit can be reduced by covering the DTOF up to late times. In the present work, this was achieved by extending the fit range to 0.1% of the DTOF's peak amplitude. The positive correlation of  $\mu_a$  and  $\mu_s'$  can also be demonstrated by considering variance (V), the second centralized statistical moment of DTOFs. In infinite media (as well as semi-infinite media with large  $\rho$ ) the following relation for variance holds [83]:

$$V = \frac{1}{4c^2} \sqrt{\frac{3\rho^2\mu_s'}{\mu_a^3}} \quad (4.1)$$

where  $\rho$  is source-detector distance and  $c$  is the speed of light in the medium. According to Eq. (4.1), to keep  $V$  constant, i.e., the shape of DTOFs could maintain, the ratio  $\mu_s'/\mu_a^3$  must remain unchanged. This means for constant  $\rho$ , since  $\mu_a$  and  $\mu_s'$  enter with different power, a small relative variation of  $\mu_a$  needs to be compensated by a 3 times bigger relative variation of  $\mu_s'$ , although in the same direction. (Note that the factor of 3 is specific for variance and does not necessarily apply to other characteristics of DTOFs).

In the procedure of searching  $(\mu_a, \mu_s')$  solutions and optimal fitting for TD measurements, the DTOFs are compared with corresponding theoretical curves which are convoluted with the instrument response functions (IRFs). For this comparison, the convoluted theoretical curves are scaled to have the same integral as the measured DTOFs, whereby the amplitude information is lost. With the increase of  $\mu_a$ , the curve width will become narrower whereas increasing of  $\mu_s'$  leads to a broadened curve. An example regarding positive correlation of contributions from  $\mu_a$  and  $\mu_s'$  on normalized reflectance DTOFs will be shown in Fig. 4.1(a).

### 4.3.2 Negative correlation in space domain

In SD, the contribution of scattering and absorption properties of turbid media on the diffuse reflectance profiles, i.e. spatially-resolved amplitude curves (SRACs), are negatively correlated with each other. Based on the diffusion equation under semi-infinite geometry and zero boundary condition, it can be derived that if  $(\rho\mu_s') \gg 1$ , i.e., the detector is far from the source, the time-resolved reflectance can be written as [34]:

$$R(\rho, t) = \frac{z_0}{(4\pi Dc)^{3/2}} t^{-5/2} \exp\left(-\mu_a ct - \frac{\rho^2}{4Dct}\right) \quad (4.2)$$

After integrating over time, the spatially-resolved reflectance can be written as:

$$R(\rho) = \int_0^\infty R(\rho, t) dt = \frac{z_0 e^{-\mu_{eff}\rho}}{2\pi\rho^2} \cdot \left(\mu_{eff} + \frac{1}{\rho}\right) \quad (4.3)$$

$\mu_{\text{eff}}=(3\mu_a\mu_s')^{1/2}$  is the effective attenuation coefficient.  $z_0$  is the depth of the isotropic source.

In practical experiments, the light attenuation  $A= \ln(R_0/R)$  is the relevant measurand and commonly used. By introducing  $A$  into Eq. (4.3) and differentiating it with  $\rho$ , one can get [119]:

$$\frac{\partial A}{\partial \rho} = -\frac{\partial \ln(R)}{\partial \rho} \approx \mu_{\text{eff}} + \frac{2}{\rho} \quad (4.4)$$

It is evident to deduce that in any specific distance range far from the source, the spatially-resolved diffuse reflectance shape, in particular the derivative of  $A$  to  $\rho$ , is solely dependent on  $\mu_{\text{eff}}$ . In other words,  $\mu_a$  and  $\mu_s'$  build a nearly reciprocal function when SRAC is constant. This explains the non-uniqueness of CW measurements [88]. The negative correlation of  $\mu_a$  and  $\mu_s'$  represents itself as reciprocal-ratio lines in a plot of  $\partial A/\partial \rho$  over  $\{\mu_a, \mu_s'\}$  space.

To maintain the shape of a SRAC, the changes originated from  $\mu_a$  and  $\mu_s'$  to SRACs will cancel each other out. Any increase of  $\mu_a$  should be compensated by a same extent decrease of  $\mu_s'$ , and *vice versa*. An example will be shown in Fig. 4.1(b).

### 4.3.3 Spatially enhanced time domain NIRS

Monte-Carlo simulations (details in Section 4.4.3) are used here to elaborate and validate the proposed spatially-enhanced time domain method. One  $(\mu_a, \mu_s')$  combination,  $I$  (0.127, 13.9)  $\text{cm}^{-1}$ , and 4 others at vertices of its one surrounding square in  $\{\mu_a, \mu_s'\}$  space, i.e.,  $II$  (0.134, 14.6),  $III$  (0.120, 13.2),  $IV$  (0.120, 14.6), and  $V$  (0.134, 13.2)  $\text{cm}^{-1}$ , are selected to simulate the diffuse reflectance. The geometry in the simulations is a 5-cm thick slab, and source-detector distance is 2 cm. As shown in Fig. 4.1(a)-4.1(b), the normalized DTOF of  $I$  is much more similar to those of  $II$  and  $III$  than of  $IV$  and  $V$ . On the contrary, for SD the normalized SRACs of  $I$ ,  $IV$  and  $V$ , which have nearly identical  $\mu_{\text{eff}}$ , are much harder to split than those of  $II$  and  $III$ .

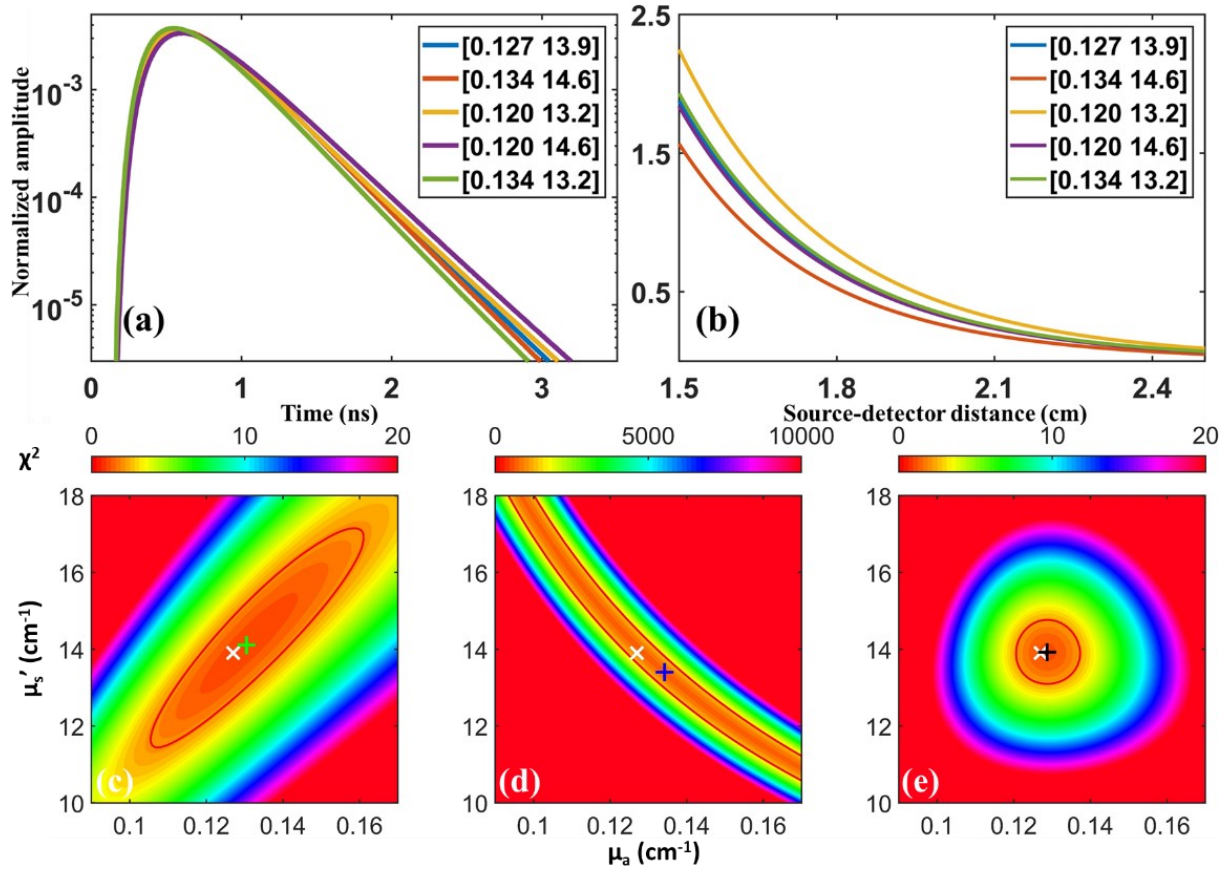


Fig. 4.1. Monte-Carlo simulations of 5 adjacent  $(\mu_a, \mu_s')$  combinations. Their reflectance profiles in (a) TD: DTOFs, (b) SD: SRACs, and the  $\chi^2$  distributions on the  $\{\mu_a, \mu_s'\}$  space based on: (c) TD fit, (d) SD fit, and (e) Spatially-enhanced TD method. The white X is the true value (0.127, 13.9)  $\text{cm}^{-1}$ , and the crosses in other colors are the optimal solutions of respective methods (Reprinted with permission from [I] © Optica Publishing Group).

A more global view can be seen in  $\{\mu_a, \mu_s'\}$  space, as illustrated by the  $\chi^2$  distributions plotted in Fig. 4.1. After adding Poisson noise, simulated DTOF and SRAC of  $I$ , (0.127, 13.9)  $\text{cm}^{-1}$ , are compared with their counterparts of all potential  $(\mu_a, \mu_s')$  combinations in a selected  $\{\mu_a, \mu_s'\}$  space ( $\mu_a$ : 0.09-0.17  $\text{cm}^{-1}$ ,  $\mu_s'$ : 10-18  $\text{cm}^{-1}$ ). The fit results, i.e. the distributions of  $\chi^2$  values in  $\{\mu_a, \mu_s'\}$  space, are generated for TD in Fig. 4.1(c) and SD in 4.1(d). The white X is the true value of  $I$  (0.127, 13.9)  $\text{cm}^{-1}$ , while the green (0.1305, 14.11)  $\text{cm}^{-1}$  and blue (0.1342, 13.4)  $\text{cm}^{-1}$  crosses are the points where the  $\chi^2$  value is minimal for TD and SD fitting, respectively. The deviations from the true value arise from the introduced noise. The red lines are the contours where the  $\chi^2$  values are 2 times minimal  $\chi^2$ .

Clearly, the ellipse-like contour in Fig. 4.1(c) refers to the low- $\chi^2$  region surrounding the minimal point. Although there is a convergence in TD, i.e. a unique minimum, the presence of noises or perturbations can cause the ambiguity and move the result away from the true value, due to the small  $\chi^2$  gradient within the ellipse contour. Meanwhile, the steep elongated ‘canyon’ in Fig. 4.1(d) refers to the low- $\chi^2$  region where all  $(\mu_a, \mu_s')$  combinations can generate SRACs

that are indistinguishable from  $I$  with added Poisson noise, indicating the reciprocal relation of  $\mu_a$  and  $\mu_s'$  in SD and the solution's non-uniqueness. Given these opposite characteristics, complementing TD and SD information effectively is promising to reduce ambiguity and improve uniqueness at the same time.

The above-mentioned purposes are realized by the isoperimetric inequality theorem as follows. First, the original  $\chi^2$  distributions from TD and SD are normalized to their minima, then merged in an artificial spatio-temporal  $\chi_{ST}^2$  distribution which contains all features from high dimensional spaces.

$$\chi_{ST}^2 = \chi_T^2 + \lambda\chi_S^2 \quad (4.5)$$

The new  $\chi_{ST}^2$  distribution is the projection of all characteristics from TD and SD on the  $\{\mu_a, \mu_s'\}$  space.  $\lambda$  is Generalized Lagrange multiplier and will be optimized by iterations.

The optimization aims at looking for the optimal  $\lambda$  which balances TD and SD information and eliminates the entanglement of  $\mu_a$  and  $\mu_s'$ , as well as at ensuring the solution's uniqueness. To this end, the isoperimetric inequality theorem is applied. Based on analyzing the shape of any given closed contour line of  $\chi_{ST}^2$  distribution, the theorem states that the ratio of area and squared perimeter can reach maximum only when the shape is a circle. More specifically, the objective function for optimization is chosen to be the isoperimetric quotient  $Q$  of  $\chi_{ST}^2$  contours:

$$Q(\lambda) = \frac{4\pi Area}{Perimeter^2} \Big|_{\chi_{ST}^2=const.} \leq 1 \quad (4.6)$$

It is worth to note that, before calculating  $Q$  in each iteration, the coordinates are normalized to the extent of the designated contour. In other words,  $Q$  is not calculated in the original  $\{\mu_a, \mu_s'\}$  space but in the new rescaled coordinate system based on the differences of maximal and minimal  $\mu_a$  and  $\mu_s'$  along the contour, to ensure the magnitudes of both coordinates comparable and to make the calculation dimensionless.  $\lambda$  will keep being updated until  $Q$  is most close to 1. The iteration process of searching the optimal solution (for this case,  $I$  (0.127, 13.9)  $\text{cm}^{-1}$  with added Poisson noise) is illustrated in Fig. 4.2.

By using the complementarity of TD and SD information, the goal is to neutralize the correlations amongst the contributions from  $\mu_a$  and  $\mu_s'$ , and to improve convergence and uniqueness. As shown in Fig. 4.2, at the 1st iteration, the original  $\chi^2$  contour presents as an oblique ellipse, when  $\lambda=0$  and Pearson correlation coefficient of the points on the red contour is  $r=0.8578$ , representing the TD positive correlation. Along with iterations,  $\lambda$  is updated to

introduce appropriate SD information, and  $r$  is gradually reduced. The optimization evolution suppresses the deviations around the optimal convergences. To the 36th iteration, the optimal  $\lambda=0.1556$  can be found to achieve  $r\approx 0$ , where a more well-defined convergence is reached. As already shown in Fig. 4.1(e), the black cross  $(0.1287, 13.92) \text{ cm}^{-1}$  based on the spatially-enhanced TD method is much closer to the true value of  $I$  than the TD and SD solutions alone.

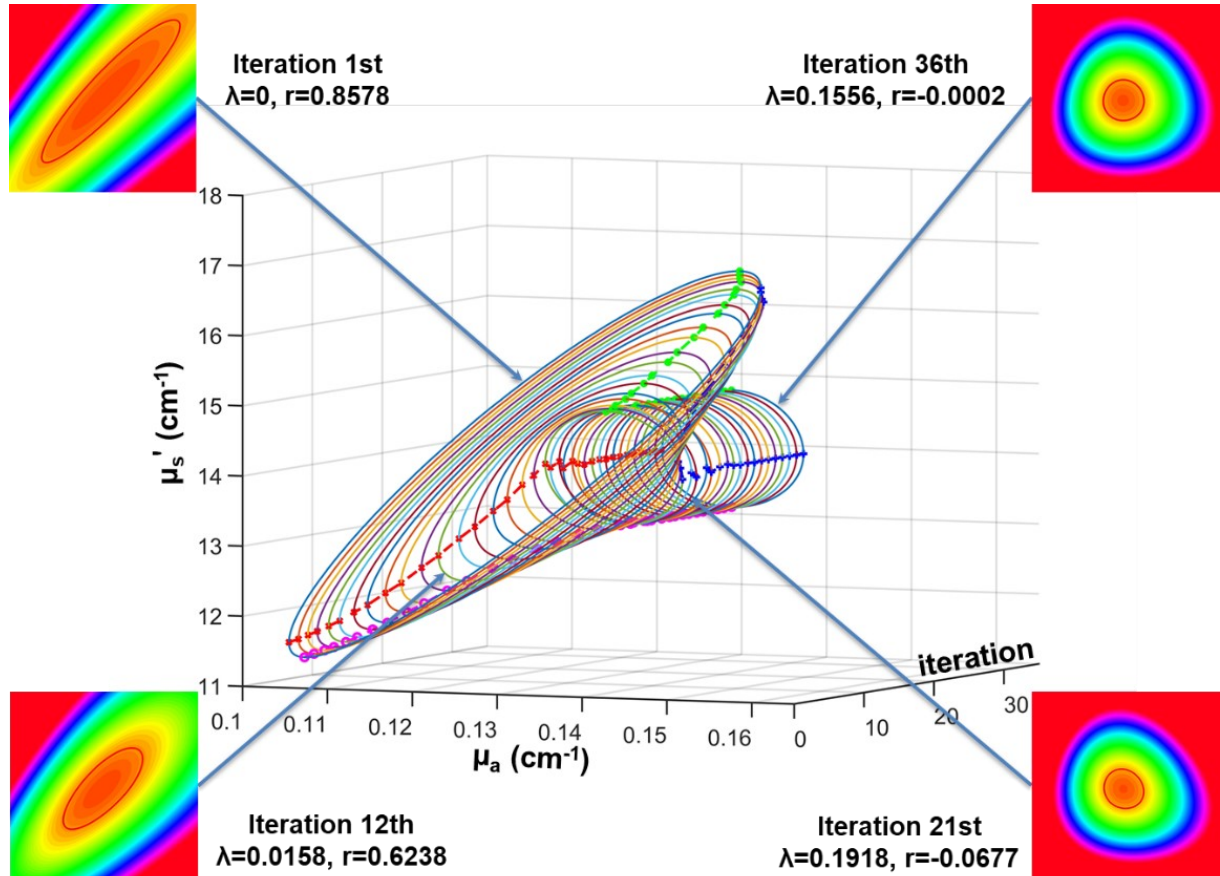


Fig. 4.2. The evolution of  $\chi^2$  contour along with iterations. The solid lines are contours of 2 times minimal  $\chi^2$ . The dotted lines are the connected extrema of  $\mu_a$  and  $\mu_s'$  at each contour.  $r$  denotes the Pearson correlation coefficient of the points on the red contours (Reprinted with permission from [I] © Optica Publishing Group).

Essentially, applying isoperimetric inequality on the inverse procedure is based on the nature of  $\mu_a$  and  $\mu_s'$ . The two coefficients, from their physical definitions, are independent to each other and shouldn't correlate. Decoupling  $\mu_a$  and  $\mu_s'$  in an artificial spatio-temporal  $\chi_{ST}^2$  is equivalent to separating them and approaching their true values. Furthermore, the result's uniqueness also restricts that the shape of such homocentric  $\chi_{ST}^2$  distribution must be a circle, where the isoperimetric inequality theorem at approaching to  $Q=1$  guarantees the only solution.

The orthogonality of two coordinates on optimized contours indicates that the cross-talk among  $\mu_a$  and  $\mu_s'$  is suppressed. The steepness of SD contour is paved by the smoothness within

TD contour, illuminating ambiguity among solutions is eliminated. Under same level of noise, the shrinking contour reveals a more confined solution.

## 4.4 Methods and materials

### 4.4.1 Phantoms

The phantoms used in the experiments are five solid homogenous cylinders. The diameter and height of the cylinder are 10.5 cm and 5 cm. They were manufactured by using epoxy resin (ME500, Nils Malmgren, Sweden) as base material, aliphatic amine (H179B, Nils Malmgren, Sweden) as hardener, TiO<sub>2</sub> powder (T-8141, Sigma-Aldrich, USA) as scatterer, and toner (4551, Infotec, UK) as absorber [96]. The amounts of absorber and scatterer added vary sequentially among the phantoms to realize gradual changes in each of the optical parameters while keeping the other constant. The details are shown in Table 4.1.

**Table 4.1. The components in 5 solid homogenous phantoms measured in the experiments. Columns Scatterer and Absorber denote the added amount of scatter stock solution (1:10 mixture of TiO<sub>2</sub> and resin) and absorber stock solution (1:100 mixture of toner and hardener).**

Name	Resin (g)	Hardener (g)	TiO <sub>2</sub> (mg)	Toner (µg)	Scatterer (g)	Absorber (ml)
α2	490.93	174.59	823.8	3.96	9.12	0.42
β2	490.87	175.03	830.1	7.93	9.19	0.84
γ1	495.67	174.90	415.5	11.89	4.60	1.26
γ2	490.93	175.23	817.5	11.89	9.05	1.26
γ3	486.31	175.01	1250.2	11.89	13.84	1.26

According to the added amounts of TiO<sub>2</sub> and toner, phantoms α2, β2, and γ2 should have nearly identical  $\mu_s'$  (around 9 cm<sup>-1</sup> at 800 nm), whilst phantoms γ1, γ2 and γ3 should have nearly identical  $\mu_a$  (around 0.125 cm<sup>-1</sup>). The final results for the optical properties of the phantoms are given in the result section below. In contrast to liquid phantoms based on intralipid and ink [99], the optical properties of epoxy based solid phantoms cannot be simply derived from the amount of the added components. In particular, the ways (e.g., mechanical, ultrasound) of mixing and dispersing the solid scatterers and absorbers and related heating and cooling processes will substantially influence the final properties. A well accepted method to determine the optical properties of solid phantoms is the application of time-resolved measurements with a single source and a single detector position. Below, we go beyond this way by applying three different TD approaches and discussing the optical properties as well as deviations between the methods.

### 4.4.2 Experimental setup

The experimental setup is a standard TD NIRS lab instrument with an SD extension. As schematically depicted in Fig. 4.3, a supercontinuum laser (SC500-6, Fianium, UK) equipped with an acousto-optical tunable filter (AOTF) is used as the light source, operated at 800 nm and providing picosecond light pulse with a repetition rate of 40.5 MHz. The output beam is guided by a 1.6 m multimode graded index fiber GI-Fiber 1 (core diameter 400  $\mu\text{m}$ , NA 0.27, Leoni, Germany). The light is diffused in the phantoms, re-emitted from their surfaces, and then collected by the other 1.6 m multimode graded index fiber GI-Fiber 2 (core diameter 600  $\mu\text{m}$ , NA 0.22, Leoni, Germany). The position of GI-Fiber 1 is fixed by a holder on the table. GI-Fiber 2 is mounted on a vertical linear stage (PT1/M, Thorlabs, USA) to adjust the height of the fiber end, and this linear stage is mounted on a horizontal long-range precision linear translation stage (length: 120 mm, OWIS, Germany) to move the detector fiber on the surfaces of phantoms to realize source-detector separations: from 15 to 25 mm with 1 mm step size. Both fibers' ends are carefully adjusted to the same height, vertical and close to phantom surfaces. Black sponge rings and cubes are stuffed around and between the fiber ends to block stray light travelling along the surface as well as residual ambient light. The phantoms are placed on a platform adjusted horizontally with a spirit level.

The whole detection part of the setup is placed in a black metal box to avoid stray light and prevent potential damage to the detector: a hybrid photomultiplier module (HPM-100-50, Becker&Hickl, Germany) controlled by a detector control card (DCC-100, Becker&Hickl, Germany) in the computer. The collected light is guided by GI-Fiber 2 into a black box to illuminate the detector. A shutter (Melles Griot, Germany), a Labview-controlled motorized attenuator (NDC-100C-4, OD: 0 to 4.0, Thorlabs), a collimator, and a focusing lens are placed between fiber end and detector to adapt the light intensity and reshape the beam.

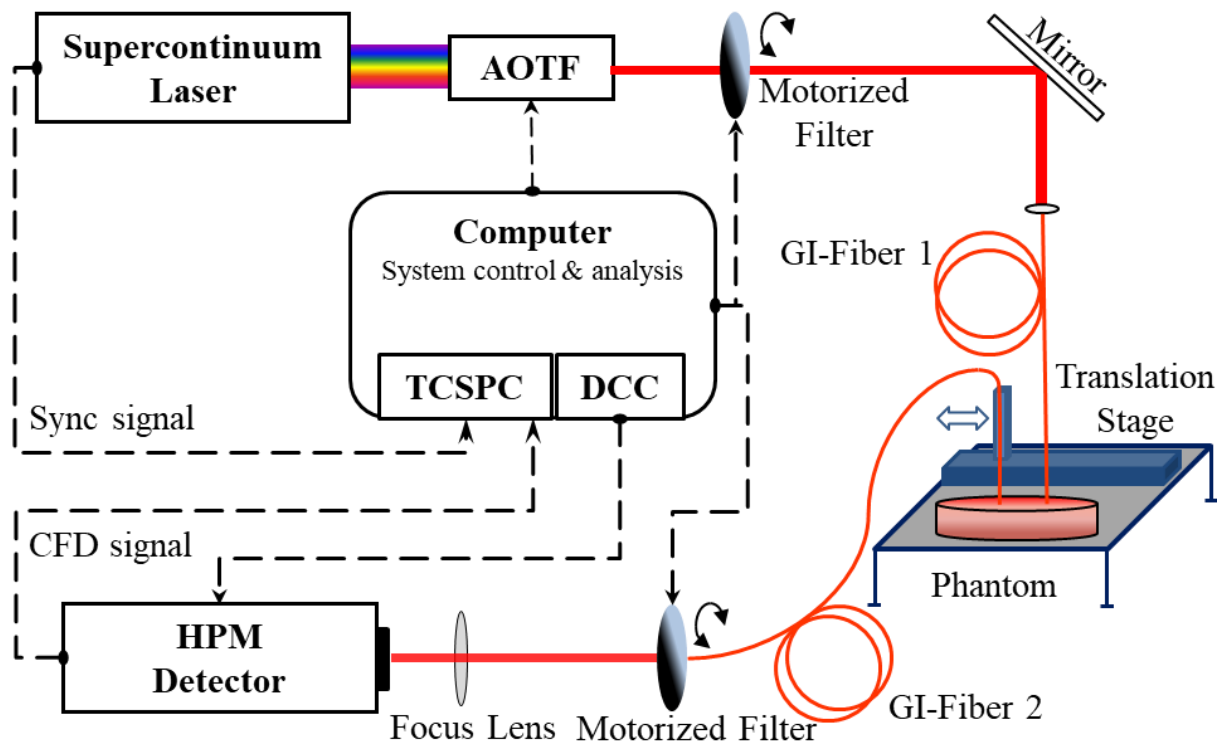


Fig. 4.3. Schematic diagram of the experimental setup. The solid lines are optical paths and the dotted lines are electric signals paths (Reprinted with permission from [1] © Optica Publishing Group).

The detected photon pulses are recorded by a time-correlated single photon counting (TCSPC) module (SPC-150, Becker&Hickl). The Sync signal from laser system is transferred to the TCSPC to provide the timing for the CFD signal from detection system. At every source-detector separation the DTOFs are recorded with a collection time of 1 s and collected 50 times to significantly improve the SNR. The DTOF monitoring, TCSPC settings control, and real-time raw signal analysis are all performed by one LabView program. DTOFs at the various source-detector distances were recorded with the same attenuation filter settings to maintain the amplitude information. The integrals of photon counts over all time channels are used as the light amplitude information in the analysis. The dead-time compensation mode of TCSPC is applied to prevent counting loss due to dead time effect, in case of high photon exposure, particularly for short source-detector separation. The maximum count rate was limited to 800 kHz to avoid dead-time related pulse shape distortions. We should note that this was an experimental set-up for proof-of-principle studies. For in-vivo applications, only single-distance DTOF detection is needed and spatially-resolved amplitude information can be obtained by CW multiple distance detection system.

For TD measurements, the IRF measurements are essential. Both fibers are mounted into a cage system and against each other. A thin diffusor is placed in front of GI-Fiber 2 to fulfill its numerical aperture and realize a similar fiber dispersion as in the phantom

measurements [120]. The distance between the two fibers' ends is precisely measured to determine  $t_0$ , the time shift between IRF and DTOF measurements. For the system shown here, at 800 nm wavelength, the time resolution of the whole experimental setup, i.e., FWHM of the IRF is about 110 ps. The IRF is always measured twice, before and after the measurements of each phantom.

#### 4.4.3 Monte-Carlo simulations and forward model

The main quantitative analysis is carried out by a white Monte-Carlo (MC) [69] GPU-based CUDA program. The concept and implementation of MC in diffuse optics have been widely studied through the years. In below we give a brief overview of MC simulations in this work.

DTOF curves are simulated by assuming a homogeneous slab with the thickness of the phantoms, 5 cm. Hereby, the lateral edges of the experimental phantoms can be neglected since the DTOFs were always measured in the central part of the cylinders' surface. For each simulated set of DTOFs, 429 billion photons are launched into the slab. Simulated photons leaving the slab in reflection are collected on concentric rings around the injection point with a step size of 0.01 cm and a time resolution of 2.44 ps. The refractive index and anisotropy factor are set as  $n=1.55$  and  $g=0.6$ . Generally, the  $g$  value does not affect the simulated DTOFs for source-detector distances between 1.5 and 2.5 cm as in measurements, since under these conditions the simulations solely depend on  $\mu_s'$ . The simulated DTOFs are then convolved with a Gaussian laser profile according to the diameter of the laser output fiber. To account for the size of the detector fiber, a circular cross section is overlaid onto the concentric rings at all detector positions as well.

As a collection of these MC simulations, a look-up table (LUT) database was created as the forward model in advance of the measurements. This database contains simulated DTOFs for  $\mu_s'$  range of [0.2 20]  $\text{cm}^{-1}$  with a step size of 0.2  $\text{cm}^{-1}$ .  $\mu_a$  was set to zero according to the white MC concept. DTOFs of specific  $(\mu_a, \mu_s')$  combinations are obtained from this LUT by (i) linear interpolation between the stored DTOFs with respect to  $\mu_s'$ , and then (ii) by multiplication of this DTOF with the time dependent absorption factor  $\exp(-\mu_a ct)$ .

#### 4.4.4 $\chi^2$ objective function and inverse models

Given the measurements and simulation curves, the universal  $\chi^2$  objective function is defined as:

$$\chi^2 = \frac{1}{n-2} \sum_{i=1}^n \left( \frac{m_i - s_i}{\sigma_i} \right)^2 \quad (4.7)$$

where  $i = (1 \dots n)$  represent the time or space channels of fitting interest. Therefore  $m_i$  corresponds either to the photon counts at each time channel of the measured DTOF curve in TD or, after integrating DTOF over time, to the light amplitude at each source-detector separation of the SRAC in SD. Likewise,  $s_i$  corresponds to the MC simulation counterpart of  $m_i$ .  $\sigma_i$  is the standard deviation of  $m_i$ .  $(n-2)$  are the degrees of freedom of the inverse models.  $m_i$  were always corrected by background subtraction.

For analysis and comparison purposes, there are four inverse models applied in this work: (1) conventional TD model, (2) SD model, (3) global TD model, and (4) spatially-enhanced TD model. For all TD models,  $i$  ranges are always selected in the time interval from 80% height on the rising edge (left) to 0.1% height on the decay part (right), relative to the amplitude at the peak of curves. Accordingly, the simulated curves need to convolve with measured IRFs, and then be rescaled to  $\sum_i m_i$  for generating  $s_i$ . More specifically:

- (1). Conventional TD model calculates  $\chi^2$  on DTOFs at one single source-detector distance;
- (2). SD model calculates the  $\chi^2$  on the SRACs over all space channels  $\rho$ , i.e. 1.5 to 2.5 cm;
- (3). Global TD model denotes the fit procedure based on the DTOFs from all available source-detector distances to determine  $\mu_a$  and  $\mu_s'$  whereby the relative amplitudes of every individual DTOFs are also considered. By expanding time channel range  $i$  to the DTOFs at all space channels  $\rho$ , the model exploits the full TD and SD information of the measured data.
- (4). Spatially-enhanced TD model is carried out as described in section 4.3.3.

The inverse models traverse all combinations of  $\mu_a$  and  $\mu_s'$  to draw  $\chi^2$  distributions in  $\{\mu_a, \mu_s'\}$  space. The optimal solution is determined at the place the objective function is minimal.

## 4.5 Results

Figure 4.4 gives an example of measured DTOFs for the various source-detector distances  $\rho$  and corresponding curve fitting results from conventional TD and global TD model. The data in Fig. 4.4 refer to phantom  $\beta_2$ , for its intermediate optical properties among all phantoms.

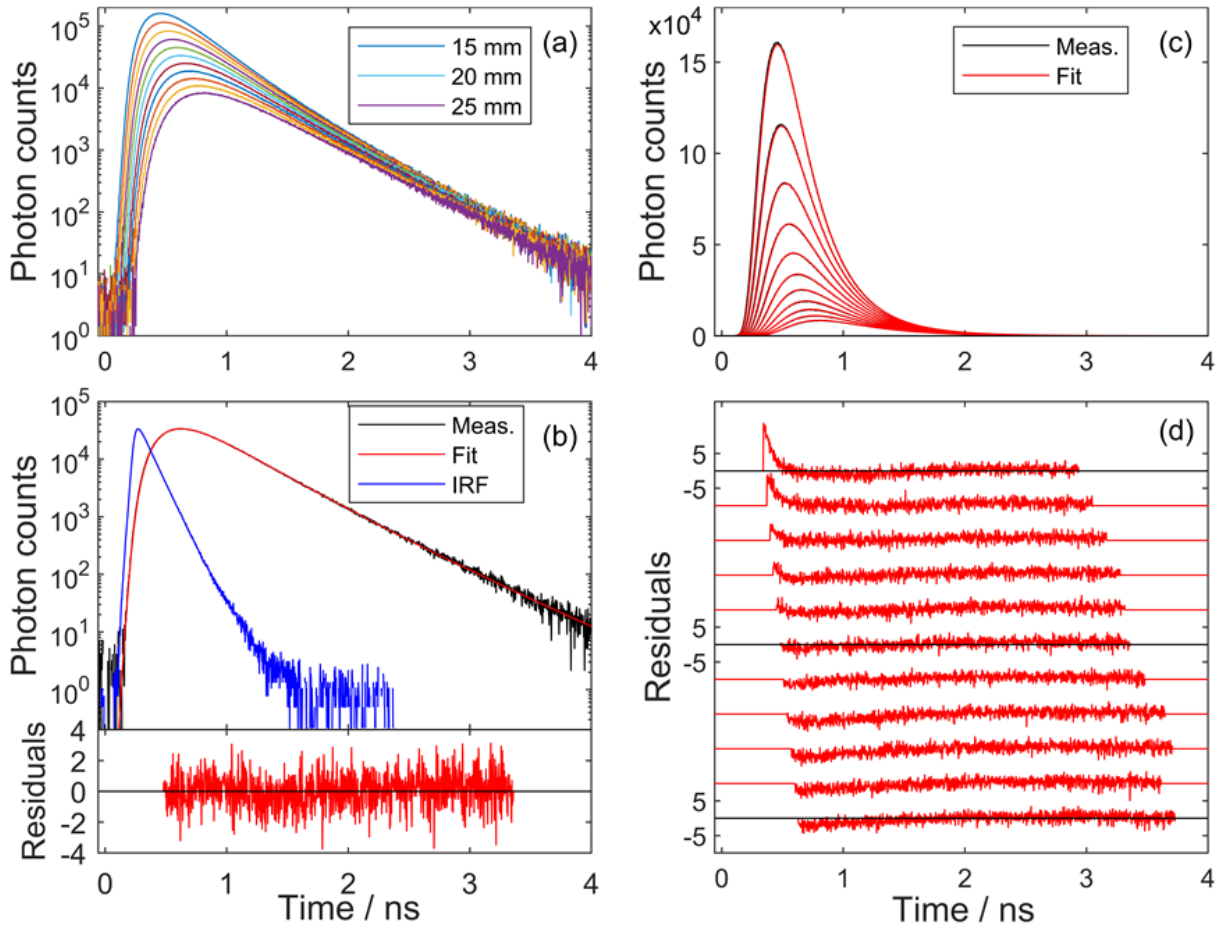


Fig. 4.4. (a) DTOFs measured on  $\beta 2$  at source-detector distances  $\rho$ : from 15 to 25 mm. (b) Conventional TD model: The optimal curve fit for DTOF at  $\rho=20$  mm, the IRF curve and the weighted residuals. Global TD model: (c) the optimal curve fit, and (d) weighted residuals of DTOFs at various  $\rho$  (top: 15 mm, bottom: 25 mm) (Reprinted with permission from [I] © Optica Publishing Group).

In Fig. 4.4(a), the original DTOFs at various  $\rho$ , after background subtraction, contain all the temporal and spatial information from measurements of  $\beta 2$ . The curve fit depicted in Fig. 4.4(b) is the optimal fit of the DTOF at  $\rho=20$  mm based on the conventional TD model, and considers only the temporal information of diffuse photon migration. The flattened residuals along with time imply a good fit quality and a small (for this case the minimal)  $\chi^2$  value. The curve fit in Fig. 4.4(c) is based on the global TD model. This approach attempts to simultaneously fit the DTOFs at all  $\rho$  and the relative amplitudes amongst DTOFs are not abandoned. Therefore the temporal and spatial information are both considered in some degree. It has to compromise between the global optimal fit and every individual optimal fit when these two contradict each other. As shown in Fig. 4.4(d), the fit residuals from top to bottom are from the DTOFs at  $\rho=15$  mm to 25 mm, under the optimal global TD regime. The discrepancies at the early time channels of smaller  $\rho$  sites will be suppressed if the single distance conventional TD model were applied, but hence leads to different fit results.

Figure 5.5 summarizes the detailed  $\chi^2$  distributions in the  $\{\mu_a, \mu_s'\}$  space under the different analysis scenarios for all phantoms. It's worth to note that the color bars in the 1st, 3rd and 4th column (TD analysis) obey the same limit [0 300], while in 2nd column (SD analysis) it's 10 times amplified to [0 3000], indicating the steeper  $\chi^2$  valley in SD.

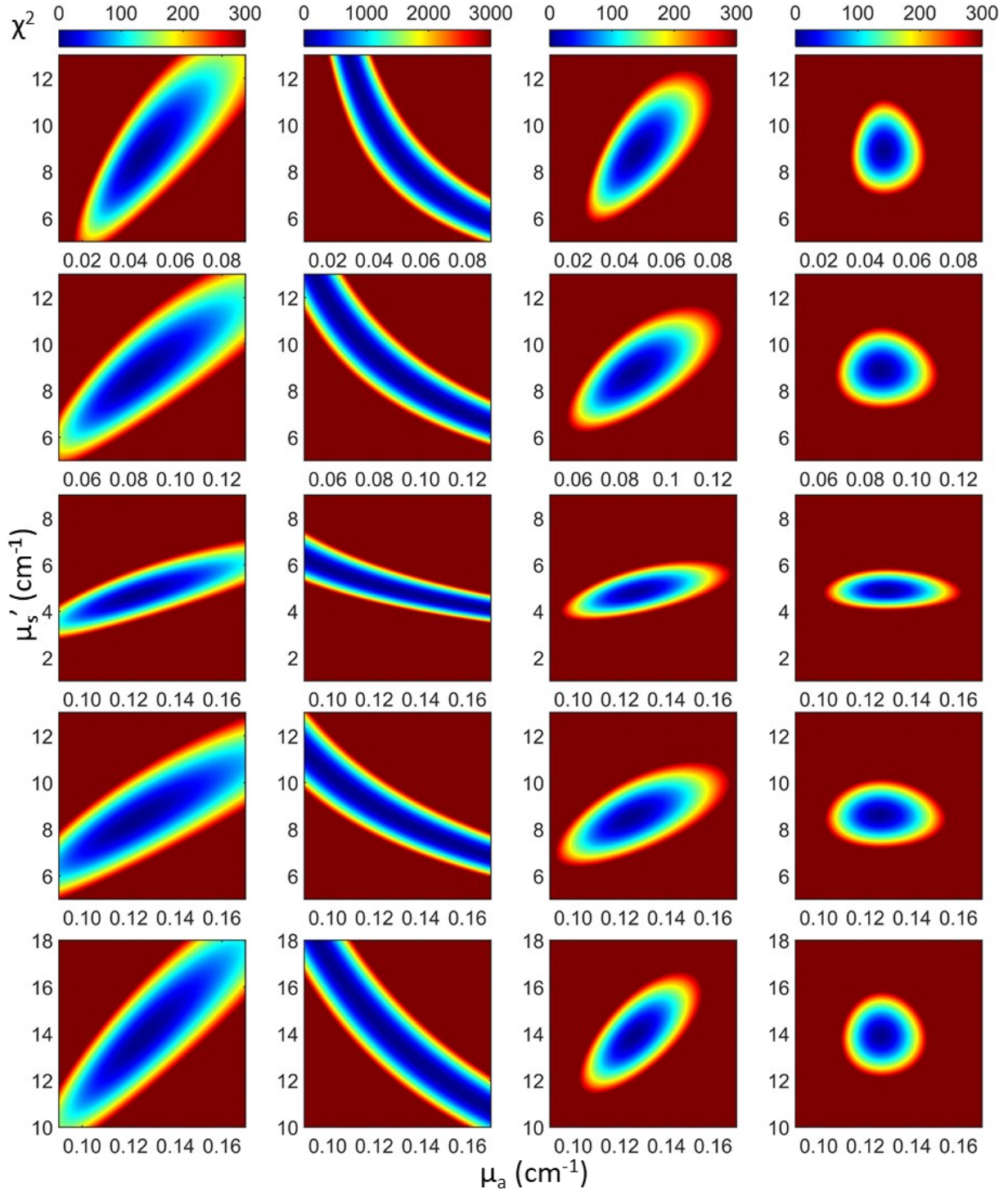


Fig. 4.5.  $\chi^2$  distributions in the  $\{\mu_a, \mu_s'\}$  space. From left to right: conventional TD, SD, Global TD, and Spatially-enhanced TD; from top to bottom: Phantom  $\alpha_2$ ,  $\beta_2$ ,  $\gamma_1$ ,  $\gamma_2$  and  $\gamma_3$  (Reprinted with permission from [I] © Optica Publishing Group).

For all phantoms it is obvious that  $\mu_a$  and  $\mu_s'$  have opposite correlations in TD and SD profiles leading to different shapes and orientations of low value regions of  $\chi^2$  distributions. Specifically, the following points can be noted from the different columns in Fig. 4.5: (1) In conventional TD fit, the ellipse-like low  $\chi^2$  zones have small gradients along the long axis of the ellipse. Although there is an optimal solution, i.e. minimal  $\chi^2$  point, the results can easily move away from the real solution or split into several regional minima in the existence of noise or various perturbations. (2) In SD fit, the extended  $\chi^2$  valley indicates the non-uniqueness of an optimal solution. And the steepness of the valleys shows qualitatively the explicit reciprocal relation amongst  $\mu_a$  and  $\mu_s'$ , as discussed in Section 4.3.2. (3) The global TD reduces the ambiguity in low  $\chi^2$  ellipses by shrinking their area. However, the extent is insufficient and the cross-talk and correlation among the two unknown properties are not eliminated. (4) By spatially-enhanced TD, not only the ambiguity area of low  $\chi^2$  zone can be reduced, but also the cross-talk artefact can be compressed to minimum extent. The correlation coefficients among the two desired coefficients are nearly reduced to zero, which implies that the entangled contributions from scattering and absorption are decoupled by integrating SD and TD information. (5) For different phantoms, the sensitivities for  $\mu_a$  and  $\mu_s'$  differ. In general, a higher  $\mu_s'/\mu_a$  ratio will make the inversion more sensitive to  $\mu_s'$ , as illustrated by the contour orientations of  $\gamma_1$ ,  $\gamma_2$  and  $\gamma_3$ . On the other hand, a higher  $\mu_a/\mu_s'$  ratio will make the inversion less sensitive to  $\mu_a$ , by comparing the contour orientations of  $\alpha_2$ ,  $\beta_2$  and  $\gamma_2$ .

**Table 4.2. The absorption and reduced scattering coefficients derived from conventional, global, and spatially-enhanced TD methods. (units:  $\text{cm}^{-1}$ )**

	Conventional TD		Global TD		Spatially-enhanced TD	
	$\mu_a$	$\mu_s'$	$\mu_a$	$\mu_s'$	$\mu_a$	$\mu_s'$
$\alpha_2$	0.0464	8.72	0.0474	8.82	0.0479	8.91
$\beta_2$	0.0843	8.68	0.0857	8.74	0.0868	8.88
$\gamma_1$	0.123	4.69	0.127	4.81	0.129	4.90
$\gamma_2$	0.122	8.36	0.125	8.49	0.126	8.61
$\gamma_3$	0.126	13.87	0.126	13.9	0.127	13.92

Table 4.2 summarizes the optical properties of the 5 phantoms derived from all 3 TD methods. Suffering from the non-uniqueness, the results by SD method are arbitrary and far from those by TD methods, therefore they are excluded from the comparison. The general trends for all phantoms' results shows a good match along with the added absorber and scatterer volume shown in Table 4.1. Table 4.2 reveals that there are small but systematic changes between the results of the three methods. The spatially-enhanced method yields the largest absorption and reduced scattering coefficients. Compared to the global TD method, absorption

is larger by 0.3% to 1.5%, and scattering by 0.1% to 1.9%. The main reason for this deviation is that the center lines of the valleys in the space domain method (Fig. 4.5, 2nd column) do not cross the minima of the  $\chi^2$  distributions from the global fits (Fig. 4.5, 3rd column). Instead, the center lines are slightly shifted to the upper right with respect to the ellipses from the global TD analysis. This result indicates some general deviations between the pure TD and the pure SD information. The global TD analysis exploits both types of information in the most comprehensive way. Even though, the systematic deviations of the corresponding residuals from the zero line (Fig. 4.4d) indicate that there is no perfect match between the global TD model and the experiment either. Hence, one cannot decide whether the global TD or the spatially-enhanced TD results are the most reliable solution. Both methods weight the measured information in different ways. Another reason for the deviations could be that both methods sample slightly different sub-volumes of the phantom, while the phantoms are not perfectly homogeneous. The absorption and reduced scattering coefficients from the conventional TD method are smaller than the results of the other TD methods. Compared to the global TD analysis, the deviation in absorption ranges from -0.2% to -2.8% and in scattering from -0.2% to -2.5%. Hence, by skipping the amplitude information of the acquired DTOFs we get a shift along the diagonal line (main axis of the ellipse in the 1st column of Fig. 4.5). Generally, the small deviations between the spatially-enhanced TD and the global TD method demonstrate the power of the spatially-enhanced method. Corresponding data can be acquired by a single time-domain detection channel combined with highly economical and fast CW intensity detection at selected distances  $\rho$ . In contrast, the global TD method would require either time-consuming scanning with a single TD channel or parallel detection with an expensive multichannel TD system.

## 4.6 Analysis of uncertainty, robustness, and uniqueness

The quality and performance of the 3 TD methods are quantitatively analyzed and compared from the perspectives of uncertainty, uniqueness, and stability.

### 4.6.1 Uncertainty

We propose to use the shape and size of  $\chi^2$  contours as the quantitative measure to compare the uncertainty of methods. As presented in Fig. 4.5, the low  $\chi^2$  ellipse zones from conventional TD can be squeezed to smaller zones. The uncertainty of the same level of  $\chi^2$ , i.e. the extremum on the contours, can be reduced. As a measure of uncertainty, the ratio of error bar on 5 times  $\chi_{\min}^2$  contour lines divided by the optimal solution is defined in Eq. (4.8). Our

analysis has shown that the results have good agreement based on different-times  $\chi_{\min}^2$  contours. The choice of 5 times  $\chi_{\min}^2$  contour here is used as a representative.

$$\varepsilon = \frac{(\mu_{\text{Max}} - \mu_{\text{Min}})|_{5\chi_{\text{Optima}}^2}}{\mu_{\text{Optima}}} \quad (4.8)$$

where  $\mu_{\text{Max}}$  and  $\mu_{\text{Min}}$  are the maximum and minimum values of  $\mu_a$  or  $\mu_s'$  on the designated contour line.  $\mu_{\text{Optima}}$  is the value of  $\mu_a$  or  $\mu_s'$  at  $\chi_{\min}^2$  enclosed by contours, i.e., the optimal solution.

**Table 4.3. The uncertainty comparison about  $\mu_a$  and  $\mu_s'$  of different methods.**

	Conventional TD		Global TD		Spatially-enhanced TD	
	$\varepsilon(\mu_a)$	$\varepsilon(\mu_s')$	$\varepsilon(\mu_a)$	$\varepsilon(\mu_s')$	$\varepsilon(\mu_a)$	$\varepsilon(\mu_s')$
$\alpha_2$	13.7%	20.7%	11.0%	16.7%	7.7%	11.3%
$\beta_2$	13.4%	16.6%	10.0%	12.5%	6.0%	7.5%
$\gamma_1$	13.2%	13.6%	13.5%	14.3%	7.6%	9.4%
$\gamma_2$	12.8%	14.1%	9.2%	10.3%	5.9%	7.0%
$\gamma_3$	10.5%	11.5%	5.2%	5.7%	3.9%	4.4%

Table 4.3 lists the relative uncertainty  $\varepsilon$  of the different methods for all 5 phantoms. The ratio reveals that, under the presence of noise or perturbation, how far the maximal deviations of unknown parameters can reach. By comparison, it is apparent that Spatially-enhanced TD can significantly reduce this kind of variance.

In addition, the size of low- $\chi^2$  region is the other measure to evaluate whether a method can find a well-defined optimum and compress variance. Here we normalize all areas of 5 times  $\chi_{\min}^2$  contours to that of conventional TD, as in Table 4.4.

**Table 4.4. Comparison the area of 5 times  $\chi_{\min}^2$  contour of different methods**

	Conventional TD	Global TD	Spatially-enhanced TD
$\alpha_2$	1	0.905	0.609
$\beta_2$	1	0.867	0.440
$\gamma_1$	1	1.772	0.866
$\gamma_2$	1	0.901	0.534
$\gamma_3$	1	0.441	0.353

Compared with the conventional TD method, spatially-enhanced TD method halves the area of the low  $\chi^2$  zones. This indicates that Spatially-enhanced TD method will find more well-defined optima, since the  $\chi^2$  distributions are more concentrated and the  $\chi^2$  gradient in low  $\chi^2$  zones becomes steeper.

#### 4.6.2 Uniqueness

One of the most important attributes of TD NIRS techniques is their ability to separate effects from absorption and scattering. Although in theory all the TD methods exhibit an optimum, i.e. minimal  $\chi^2$  in the  $\{\mu_a, \mu_s'\}$  space, the effects of changes in both parameters on the residuals often interfere. Error in one parameter can manifest as artefacts in the other and reduce the accuracy of both. Such correlation leads to ambiguity and cross-talk among parameters, or several regional optimal solutions which make the inversion process difficult. For quantifying the correlation strength, here Pearson correlation coefficient of points on the 5 times  $\chi_{\min}^2$  contour line is used to evaluate the performance of decoupling the unknown parameters.

$$r|_{5\chi_{Optima}^2} = \frac{Cov(\mu_a, \mu_s')}{\sigma(\mu_a)\sigma(\mu_s')} \quad (4.9)$$

where  $Cov$  is the covariance function and  $\sigma$  is the standard deviation. In Table 4.5, the  $r$  of points assembling the 5-times- $\chi_{\min}^2$  contour lines in the  $\{\mu_a, \mu_s'\}$  space are presented and compared.

**Table 4.5. Pearson correlation coefficients of  $5 \times \chi_{\min}^2$  contour lines**

	Conventional TD	Global TD	Spatially-enhanced TD
$\alpha_2$	0.7418	0.5568	-0.0001
$\beta_2$	0.7839	0.5444	-0.0018
$\gamma_1$	0.7699	0.4841	-0.0001
$\gamma_2$	0.8095	0.5272	-0.0018
$\gamma_3$	0.8435	0.5476	-0.0003

It can also be noticed from Fig. 4.5 that the  $\chi^2$  distributions in the  $\{\mu_a, \mu_s'\}$  space for conventional TD and global TD are both positively correlated, despite global TD slightly reduces the correlation by considering the SD's negative correlation effect. The correlation coefficients can be reduced to nearly zero by spatially-enhanced TD method for all phantoms. The essential aspect is that this method can adjust the weights between two contradicting correlation and search for an optimal balance to neutralize both. Therefore, for any  $\mu_a, \mu_s'$  combinations it can always achieve a compromise between the effects from  $\mu_a$  and  $\mu_s'$  and separate both parameters. The uniqueness of the optimal solution can be guaranteed by the decorrelation process.

### 4.6.3 Stability

In this work we also study the stability of the methods between successive measurements. The measurements are all recorded for 50 repetitions with 1 s per repetition. Here we split the measurements into 10 segments where each segment comprises 5 s. Then the three TD methods are applied on these segments to obtain 10 different results of  $\mu_a$  and  $\mu_s'$ . The mean ( $\bar{\mu}$ ) and

standard deviation ( $\sigma$ ) are calculated. Then the coefficients of variation ( $CV = \sigma/\bar{\mu}$ ) of the results from different methods are calculated and presented in Table 4.6.

**Table 4.6. Comparison of coefficient of variation for different methods**

	Conventional TD		Global TD		Spatially-enhanced TD	
	$CV(\mu_a)$	$CV(\mu_s')$	$CV(\mu_a)$	$CV(\mu_s')$	$CV(\mu_a)$	$CV(\mu_s')$
$\alpha_2$	0.37%	0.23%	0.09%	0.08%	0.13%	0.09%
$\beta_2$	0.37%	0.26%	0.10%	0.11%	0.12%	0.08%
$\gamma_1$	0.33%	0.40%	0.09%	0.11%	0.05%	0.01%
$\gamma_2$	0.47%	0.32%	0.06%	0.10%	0.12%	0.09%
$\gamma_3$	0.33%	0.35%	0.06%	0.09%	0.07%	0.08%

The coefficient of variation can describe the degree of dispersion of the results under the same experimental conditions but at different measurement time, thus evaluate the repeatability of methods. According to Table 4.6, in general the dispersions are all small, owing to the fine MC database and low-noise measurements. Both global TD and spatially-enhanced TD show improved stability compared to conventional TD. For some cases  $CV(\mu_a)$  values for spatially-enhanced TD are slightly higher than for global TD. This is mainly due to the fact that global TD processes much more information than spatially-enhanced TD. This also means, by acquiring fewer measurements, spatially-enhanced TD is able to reach the nearly a same level of stability as global TD. The stability performance of spatially-enhanced TD could be further improved, if using a reliable CW power detection system to provide amplitude information, instead of the photon counting system utilized in this experiment setup. It is essential that, in lower signal or short-time acquisition conditions, the methods which consider the SD information will compress the spread of results.

## 4.7 Conclusion

In aim to improve uniqueness, stability and uncertainty associated with the inverse problem on simultaneously retrieving the absolute quantities of optical absorption and scattering properties in turbid media, a multivariate method integrating time and space resolved techniques of near-infrared spectroscopy is proposed. The spatially-resolved distributions of times of flight contain the maximal information one can obtain from the reflectance scattered field, but also the sufficient information for extracting complete optical knowledge of an object's interior. The essence of the problem is how numerous observations of different data types should be combined so as to give the most optimal result. We utilized the opposite correlations in time domain (positive) and space domain (negative) observations with the entangled effects that originated from two physically independent features - absorption and scattering - and

dynamically merged them into an artificial spatio-temporal  $\chi_{ST}^2$  projection on  $\{\mu_a, \mu_s'\}$  space. By applying the isoperimetric inequality theorem on  $\{\mu_a, \mu_s'\}$  space, absorption and scattering can be separated with high accuracy. Monte-Carlo simulations are used to illustrate and validate the concept of the method. A set of tissue-mimicking phantoms have been measured in a spatially-enhanced time domain experiment. By recovering  $\mu_a$  and  $\mu_s'$  of the phantoms with various inverse methods, the improvements on the result quality given in terms of uncertainty, uniqueness and stability are demonstrated through comparison. With fewer measurements and simpler system, the spatially-enhanced TD method could achieve similar level of stability as the global TD method. It is shown that, with the complementarity, Spatially-enhanced TD method can efficiently constrain the time-domain feature of photon migration by its spatially-resolved amplitude patterns. When measuring low photon counts at large source-detector separations, spatially-enhanced TD NIRS has the potential to avoid the influence from superficial tissues and allow the homogenous models to estimate the optical properties of deep regions in heterogeneous layered structures. Although the present work focuses on homogenous media so far, similar principles could be applied in more sophisticated structures such as layered media, where scattering properties in deeper region are difficult to determine. Besides, the effective combination of TD and SD information may indicate the potential of integrating other kinds of data types, such as temporal moments, Mellin-Laplace moments, and various frequency-domain quantities.

#### **4.8 Funding and Acknowledgement**

This project has received funding from the European Union's Horizon 2020 Marie Skłodowska-Curie Innovative Training Networks (ITN-ETN) programme, under grant agreement no 675332, BitMap.

The authors acknowledge Stefan Schieck for preparing the phantoms.

# 5

## Space-enhanced time-domain diffuse optics in layered structures

### **This chapter was previously published in:**

Lin Yang, Heidrun Wabnitz, Thomas Gladysz, Aleh Sudakou, Rainer Macdonald, and Dirk Grosenick, “Space-enhanced time domain diffuse optics for determination of tissue optical properties in layered structures”. In: *Biomedical Optics Express* **11**, 6570-6589 (2020) ©.

### **Contributions to this chapter:**

I initialized the research idea, concretized the concept and methodology, and planned the measurement campaign. I prepared the phantoms, conducted all measurement activities and made data analyses. The original manuscript and the amendments before and after the peer-review are also conducted by me, with the suggestions and reviews from co-authors.

### **These co-authors contributed to this chapter:**

H.W. helped to make the measurement plan, provided the method and cell of phantom preparation, and gave revision suggestions.

T.G. helped to analyze the results of space domain measurements and gave revision suggestions.

A.S. helped to conduct parts of simulations, and gave revision suggestions.

R.M. supervised the project and gave the draft reviews and revision suggestions.

D.G. helped to perform the numerical analysis, contributed to result interpretations and discussions, and gave reviews and revision suggestions.

---

© 2020 *Optical Society of America*. Users may use, reuse, and build upon the article, or use the article for text or data mining, so long as such uses are for non-commercial purposes and appropriate attribution is maintained. All other rights are reserved.

## 5.1 Abstract

A novel methodology for solving the inverse problem of diffuse optics for two-layered structures is proposed to retrieve the absolute quantities of optical absorption and reduced scattering coefficients of the layers simultaneously. A liquid phantom with various optical absorption properties in the deep layer is prepared and experimentally investigated using the space-enhanced time domain method. Monte-Carlo simulations are applied to analyze the different measurements in time domain, space domain, and by the new methodology. The deviations of retrieved values from nominal values of both layers' optical properties are simultaneously reduced to very low extent compared to the single-domain methods. The reliability and uncertainty of retrieval performance are also considerably improved by the new methodology. It is observed in time-domain analyses that for the deep layer the retrieval of absorption coefficient is almost not affected by the scattering properties and this kind of "deep scattering neutrality" is investigated and overcome as well.

## 5.2 Introduction

Quantifying the optical properties through biological tissues is especially important for clinical diagnosis [121], owing to the pathological and physiological indicative values that the optical properties can reflect and represent for many essential biomarkers such as oxy-/deoxy-hemoglobin and cytochrome-c-oxidase in tissues (e.g., brain, kidney, and breast [22,100,101]). However, the measurement of the optical properties is also difficult due to the structurally complex random and optically diffusive nature that tissues have in the near-infrared therapeutic window ( $600 \text{ nm} < \lambda < 1000 \text{ nm}$ ) [18]. Diffuse optics, namely the implementation of near-infrared light propagation through highly diffuse media to probe the optical properties of the media in depth [102], has been studied through the years for its special advantages compared with other techniques regarding to the chromophore-selectivity and the non-invasiveness when retrieving the optical properties in tissues.

The optical properties in diffuse optics, which primarily affect the light propagation and interaction within tissues, are optical absorption and scattering. Absorption is of particular biomedical interest since it carries information about tissue chromophores. However, the transport of near-infrared light in tissues is strongly dominated by scattering, and thus the reconstruction of absorption is heavily hampered by the diffuse propagation of photons. The presence of unknown scatter would cause undesirable artefacts for the recovery of absorbers [10]. Moreover, similar scattered optical fields can be generated from different

combinations of optical absorption and scattering properties. In other words, retrieving absorption in diffuse media is an ill-conditioned inverse problem [66]. Therefore, it is crucial but difficult in diffuse optics to simultaneously retrieve absorption and scattering with sufficient accuracy.

Many studies have been devoted to this field following various approaches. In typical diffuse optics measurements, light illuminating the surface of diffuse media and propagating through the media would be collected by a detector or detector array. The variants of such basic scenario are abundant. The light source could be pulsed [34] or continuous [21], spatially structured [122] or multispectral [123]. Also, the detected light signal could be in time domain, in frequency domain [84] or continuous wave. However, regarding the data analysis process, most of these techniques quantify absorption and scattering in similar indirect procedures. By fitting a certain appropriate forward model (e.g., Monte-Carlo method [40], diffusion theory with approximations [49,51]) to the measured data, the inverse problem is considered as solved. These techniques would provide different data types which have intrinsically different level of information content. The choice of techniques and of the corresponding data types profoundly influences the accuracy of the retrieved optical properties. Nevertheless, for measurands in all these data types, such as space resolved (SR) amplitude in space domain (SD), time resolved photon distribution in time domain (TD), or demodulation and phase shift in frequency domain (FD), the effects originating from absorption and scattering of the diffuse media are always heavily entangled and cause crosstalk and ambiguity [88,116] in general. Thus, the simultaneous retrieval of absorption and scattering coefficients with high accuracy remains to be a tricky challenge today, especially for the circumstances of high noise and perturbations when measuring *in-vivo* tissues.

On the other hand, the structural complexity of many biological tissues sets the limitation of applying homogenous models despite their success in infant and small animal studies [124,125]. The assumption of tissue homogeneity would impede robust and reproducible reconstruction of optical properties in the human tissues, and the non-negligible depth dependence of the tissue composition has also been reported [126]. Nevertheless, using real detailed anatomical structures for forward models may also not be necessary since it was shown not to improve retrieval performance than slab-based layered models during the fitting of measurements [12]. Therefore, layered models may be a reasonable choice. This is also motivated by the fact that structures of many tissues are layered, for instance muscle tissue underneath superficial fat or the layered structure of the human head. Many studies have already developed the techniques such as TD single distance [127], TD multi-distance [12], FD multi-

distance [11], and improved diffusion model for TD and FD dual-distance [128], and have shown good retrieval performance for the absolute quantification of optical properties based on layered models. Another study [129] considered both TD and SD information to fast calculate optical absorption in layered models with optical scattering as prior knowledge. In a previous work [130], we have introduced the first attempt of applying the Space-enhanced Time Domain (SeTD) method in homogenous cases and demonstrated its good performance. The aim of the present paper is to evolve the SeTD method and investigate its feasibility for more practical and clinically relevant layered structures.

In this study, we propose a novel methodology that merges the information acquired from different domains to obtain an optimal estimate of the optical properties in both layers, by applying the SeTD method in two-layered structures. Investigations on two-layered liquid phantoms and analyses by TD, SD, and SeTD methods demonstrate the retrieval performance of these methods regarding accuracy, stability and linearity of optical properties. According to a finding in TD, we introduce the term of “deep scattering neutrality”, which is briefly discussed regarding the reason why it is nearly impossible to recover scattering in the deep layer by TD alone and how the SeTD method can accurately determine it.

### **5.3 Concept of space-enhanced time domain method**

With the combination of the information acquired in time and space domains, optical absorption and reduced scattering coefficients ( $\mu_a$  and  $\mu_s'$ ) can be quantified more accurately by using the intrinsic independence of the two properties. A comprehensive explanation of the SeTD approach and its advantages have already been given in a previous article [27] that considered homogenous media. In layered structures the general principle remains the same. Namely, the effects from optical absorption and scattering of diffuse media on the diffuse reflectance are entangled and correlated in time domain (TD) and space domain (SD) in different ways. By the effective mutual combination of TD and SD information, the simultaneous retrieval of absorption and scattering properties can be achieved with improved accuracy, compared to single-domain methods.

In TD, the effects of absorption and scattering on the temporal profiles of distributions of times of flight (DTOF) of photons are opposite to each other, i.e., increasing scattering broadens a DTOF, and increasing absorption narrows it. In order to maintain a certain DTOF profile, the changes of  $\mu_a$  and  $\mu_s'$  should occur in the same direction, i.e., there is a positive correlation of them in  $\{\mu_a, \mu_s'\}$  space.

In SD, the shapes of spatially-resolved amplitude curves (SRACs) are mainly determined by the effective attenuation coefficient  $\mu_{\text{eff}}$ , where  $\mu_{\text{eff}} = (3\mu_a\mu_s')^{1/2}$ . To maintain a certain SRAC shape, for  $\mu_s'$  and  $\mu_a$  any increase of one coefficient should be compensated by a decrease of the other, by keeping  $\mu_{\text{eff}}$  constant [119]. Thus,  $\mu_s'$  and  $\mu_a$  follow an approximately reciprocal function under constant  $\mu_{\text{eff}}$ , i.e., a negative correlation in  $\{\mu_a, \mu_s'\}$  space.

For layered structures, if one focuses on the optical properties in the deep layer and their correlations in TD and SD, the aforementioned general trends and correlations would not change, but only vary to slight extent. For illustration, Monte-Carlo simulations in turbid media of two-layered slab geometry were performed to demonstrate the correlations of scattering and absorption in the second layer and validate the SeTD method. Following the well-known concepts of MC simulations in diffuse optics [55,71,131], a GPU-based implementation [76] was applied with time-resolved recording of the simulated photons in reflectance. To generate DTOFs, 42.9 billion photons were launched into the two-layered slab where the 1st layer was 10 mm thick and the 2nd layer was 47.8 mm thick. For the 1st layer the optical properties are constant at  $(\mu_{a1}, \mu_{s1}') = (0.10, 10.65) \text{ cm}^{-1}$ , while for the 2nd layer the optical properties cover the ranges of  $\mu_{a2} \in [0.05, 0.25] \text{ cm}^{-1}$ ,  $\mu_{s2}' \in [6, 14] \text{ cm}^{-1}$ .

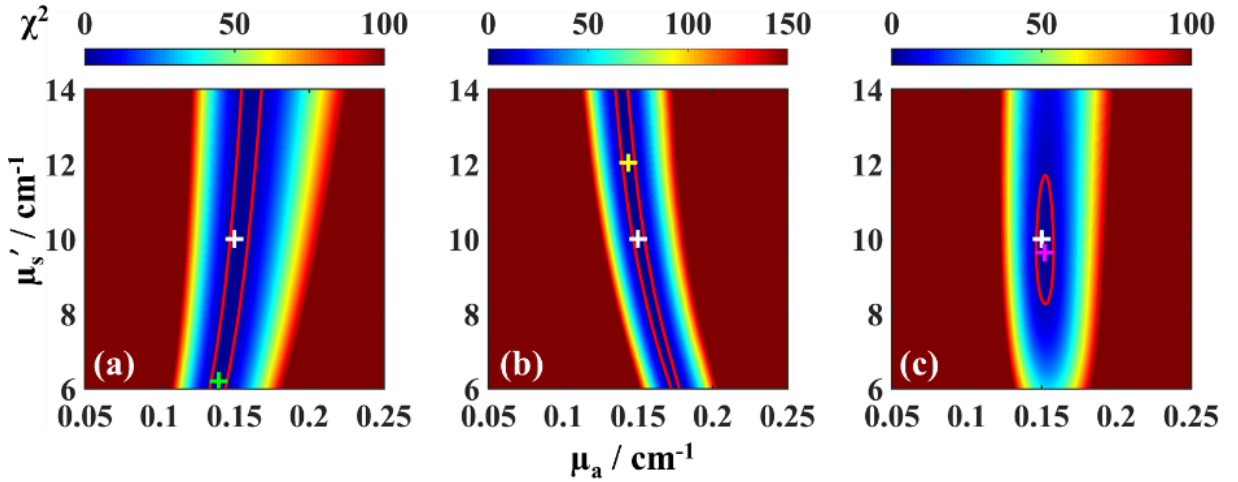


Fig. 5.1. Determining  $(\mu_a, \mu_s')$  of the 2nd layer based on MC simulations. The  $\chi^2$  distributions are plotted for (a) TD, (b) SD, and (c) SeTD methods in  $\{\mu_a, \mu_s'\}$  space. White crosses mark the true values. Results from the methods are marked by green, yellow and magenta crosses, i.e., where the  $\chi^2$  reach the minimum. Red lines are contours where  $\chi^2$  are 3 times of the minimum. The step sizes of the maps are  $0.0005 \text{ cm}^{-1}$  for  $\mu_a$  axis and  $0.02 \text{ cm}^{-1}$  for  $\mu_s'$  axis (Reprinted with permission from [II] © Optica Publishing Group).

The MC simulations of a combination  $(\mu_{a2}, \mu_{s2}') = (0.15, 10) \text{ cm}^{-1}$  were selected as virtual measurements. Poisson noise was added to the DTOFs at selected detector positions  $\rho$  to imitate TD and SD measurements. The total photon count and time bin width were set to 10 million

and 2.056 ps, respectively. To derive the optical properties by fitting measurements with simulations, the error norm was applied in  $\chi^2$  form as the universal objective function:

$$\chi^2 = \frac{1}{n-2} \sum_{i=1}^n \left( \frac{m_i - s_i}{\sigma_i} \right)^2 \quad (5.1)$$

where  $m_i$  and  $s_i$  denote the measurement and the simulation, respectively, with  $i = (1 \dots n)$  representing the effective time channels for TD or  $\rho$  channels for SD, of the fitting ranges.  $\sigma_i$  is the standard deviation of  $m_i$ . The denominator  $(n-2)$  denotes the degrees of freedom of the inverse model applied, given the two fit parameters  $\mu_a, \mu_s'$ . For TD as shown in Fig. 5.1(a), the noise-added DTOF at  $\rho = 25$  mm was selected as measurement, and Eq. (5.1) was used to compare it with the simulated DTOFs for the entire set of  $(\mu_{a2}, \mu_{s2}')$  combinations in the MC database by calculating  $\chi_T^2$ . For SD as shown in Fig. 5.1(b), a SRAC was prepared in the range  $\rho \in [20, 25]$  mm with step size 1 mm by calculating the integrals of the corresponding noise-added DTOFs, and then compared with its counterparts of all  $(\mu_{a2}, \mu_{s2}')$  combinations in the MC database by calculating  $\chi_S^2$  as well. It is evident that in Fig. 5.1(a) and 5.1(b) the  $\chi^2$  distributions exhibit different orientations, i.e., the low- $\chi^2$  regions surrounded by the red contour lines lean towards different directions. These two figures indicate that the opposite correlations of absorption and scattering in TD and SD known from homogeneous cases also exist in the two-layer situation, despite being less prominent. The optimal solutions, where the  $\chi^2$  values reach the minimum, under the given level of noise, are plotted as green  $(0.1395, 6.2)$   $\text{cm}^{-1}$  and yellow  $(0.1435, 12.04)$   $\text{cm}^{-1}$  crosses for TD and SD fits and could not be improved by repeating, while the true value  $(0.15, 10)$   $\text{cm}^{-1}$  is plotted as white cross.

From Fig. 5.1(a) and 5.1(b) it can be also seen that the discrepancies between the results from TD and SD methods and the true values are remarkable, indicating that neither the TD nor the SD method alone are sufficient to accurately retrieve the deep layer's optical properties. In contrast, their effective combination could be promising to improve the retrieval accuracy. The SeTD method is to decouple absorption and scattering and reduce the ambiguous area among them in a new artificial spatio-temporal domain (ST). In the ST domain, one optical parameter's artefacts which are introduced by errors in the estimation of the other parameter, can be minimized.  $\chi_{ST}^2$ , the ST error norm distribution in the  $\{\mu_a, \mu_s'\}$  space, is introduced as:

$$\chi_{ST}^2 = \chi_T^2 + \lambda \chi_S^2 \quad (5.2)$$

where  $\lambda$  is a Generalized Lagrange multiplier to be optimized by iteration.  $\chi_{ST}^2$  combines all characteristics of second layer's optical properties from TD and SD to the ST domain.

During the process of iteration, the correlation coefficient of the two parameters ( $\mu_{a2}$  and  $\mu_{s2}'$ ) taken at the group of points located on the contour line of  $\chi_{ST}^2$  is considered as the objective target criterion. And the iteration optimizes and reduces it as close as possible to zero. If the correlation is almost zero, the retrieved  $\mu_{a2}$  and  $\mu_{s2}'$  are then nearly independent. By adjusting  $\lambda$  along with iteration, the method is balancing the weight of the information from TD and SD to find the optimal  $\lambda$  for the artificial spatio-temporal domain, whereupon the two unknown parameters can be decoupled. As presented in Fig. 5.1(c), the effective integration of TD and SD information leads to a more well-defined minimum, i.e., the optimal convergence in  $\{\mu_a, \mu_s'\}$  space. For the case shown in the figure, the retrieved values from SeTD method are  $(\mu_{a2}, \mu_{s2}') = (0.152, 9.64) \text{ cm}^{-1}$ , which are rather close to the true values.

The orthogonality of both coordinates on the optimized contours implies that the crosstalk among  $\mu_{a2}$  and  $\mu_{s2}'$  is reduced. The smoothness within the TD contour is overcome by the steepness of the SD contour, indicating that the ambiguity of solutions is reduced. Under the same noise level, the shrinking contour reveals a more confined and stable solution of the inverse problem.

## 5.4 Methods and materials

### 5.4.1 Experimental setup

The experiments in this study were performed with a laboratory setup, as schematically depicted in Fig. 5.2. The light source was a supercontinuum laser (SuperK Fianium FIU-15 PP, NKT Photonics, Germany), providing picosecond light pulses with a repetition rate of 39 MHz. A wavelength band centered at 830 nm was selected from the broadband beam by a variable bandpass filter (Varia, NKT Photonics, Germany) with a bandwidth of 10 nm. The near-infrared beam was then collimated into and guided by a 1.6 m multimode graded index fiber (GI-Fiber 1; core diameter 400  $\mu\text{m}$ , NA 0.27, Leoni Fiber Optics, Germany) to the phantom. The photons were scattered and partially absorbed in the phantom. To collect diffusely re-emitted light, another 1.6 m multimode graded index fiber (GI-Fiber 2; core diameter 600  $\mu\text{m}$ , NA 0.22, Leoni Fiber Optics, Germany) was used. The measurements were carried out in reflection geometry, i.e., both fibers' ends equipped with SMA ferrules were plugged into the holder and vertical to the surface of the phantom cell. The source-detector distance  $\rho$  was precisely defined by the positions of cylindrical holes in the NC-machined holders. Both fibers' ends were carefully positioned in contact with the phantom's surfaces.

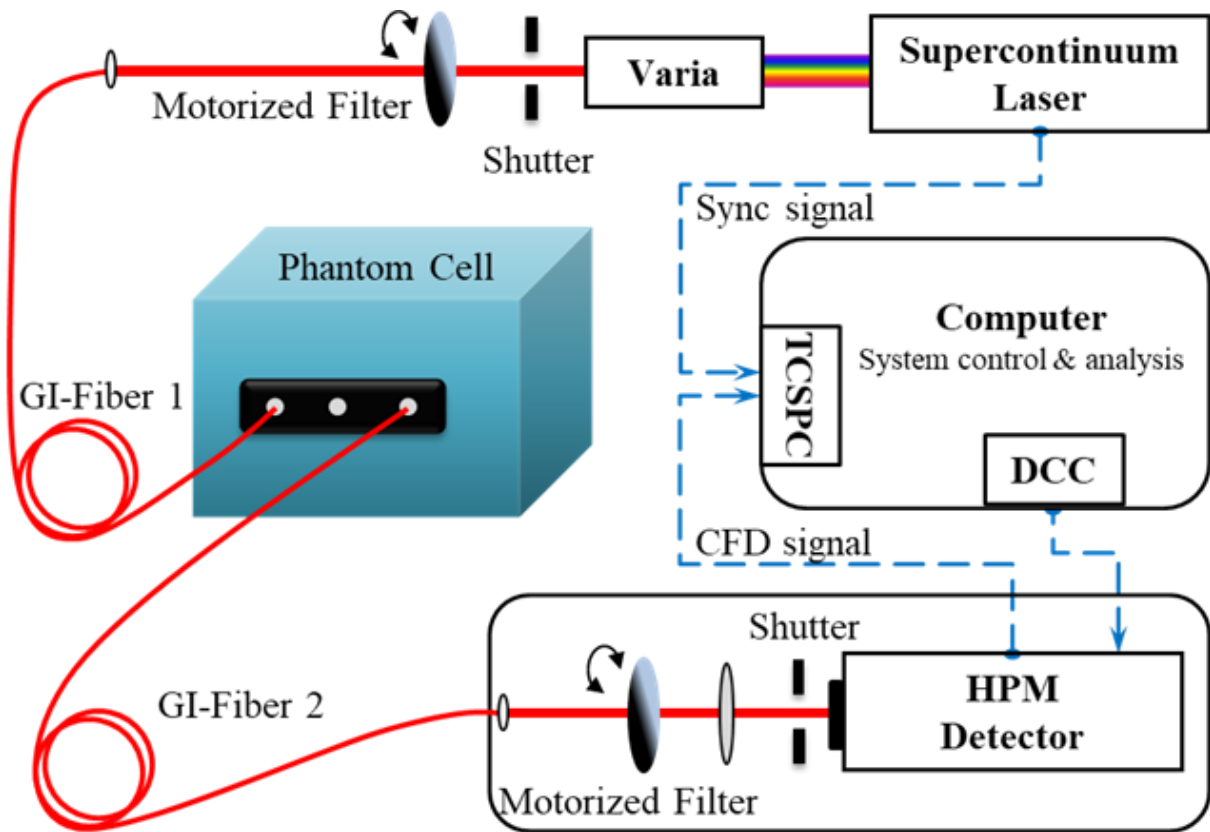


Fig. 5.2. Schematic diagram of the experimental setup. The solid red lines are optical paths and the dotted blue lines are electric signal paths (Reprinted with permission from [II] © Optica Publishing Group).

The detection components were installed in a black metal box to avoid ambient light. The light from GI-Fiber 2 was first collimated; then the free space beam was reshaped by a focusing lens and hit the photocathode of the detector, a hybrid photomultiplier module (HPM-100-50, Becker&Hickl, Germany) operated by a detector control card (DCC-100, Becker&Hickl, Germany). Two shutters (Melles Griot, Germany) and continuously variable neutral-density filters (NDC-100C-4, optical density 0 to 4.0, Thorlabs) were placed in the free space beams at laser and detector, to adapt the light intensity to the appropriate level for detection. Filters were motorized and controlled by a dedicated LabVIEW program.

The photon pulses collected by the detector were recorded by a time-correlated single photon counting (TCSPC) module (SPC-150, Becker&Hickl). The Sync signal from the laser system was transferred to the TCSPC module to provide the timing for the CFD (constant-fraction discriminator) signal from the detector. In this work, DTOFs were recorded with 1 s collection time and 20 repetitions. The dead time compensation mode of TCSPC was activated to prevent potential counting loss due to dead time effects, in case of higher photon exposure which could be inevitable for the measurements at short source-detector distances. Pulse shape distortions due to dead time effects were avoided by limiting the maximum count rate to  $<10^6/s$ .

TCSPC control, and real-time display of DTOFs and raw analysis of several characteristics were all performed by another dedicated LabVIEW program.

In addition to DTOF measurements on phantoms, it is crucial to have an independent and accurate instrument response function (IRF) measurement for TD analysis. A cage-system based “response box” was prepared, in which both fibers’ ends are mounted to face each other with a distance of 54 mm. In front of each fiber’s end a sheet of paper is inserted to engage the full numerical aperture of both fibers and to mimic a similar temporal dispersion in the fibers as in the DTOF measurements on phantoms. The optical pathlengths between both fiber’s ends is precisely evaluated to determine  $t_0$ , i.e., the time shift between DTOF and IRF measurements. For this laboratory setup, the overall time resolution, represented by the full width at half maximum (FWHM) of the IRF, is about 105 ps at 830 nm.

#### **5.4.2 Preparation and characterization of the layered phantom**

Liquid mixtures of intralipid, ink and water are used as phantom material. Intralipid-20% (Fresenius, Austria) served as diffusive medium for its stability over long time, optical similarity with tissues after proper dilution, and minor variation among batches [132]. Indian ink (Higgins ink #44201, Chartpak, USA) served as absorber, since it is chemically well-dispersible and stable, and practically does not alter the scattering properties of intralipid at the concentrations used [133]. Many research have investigated these two components’ applicability for diffuse optics experiments [99,134]. It has been shown that a phantom with well-defined optical absorption and scattering properties can be gained through carefully weighing of the two components and calculating their concentrations in the mixtures.

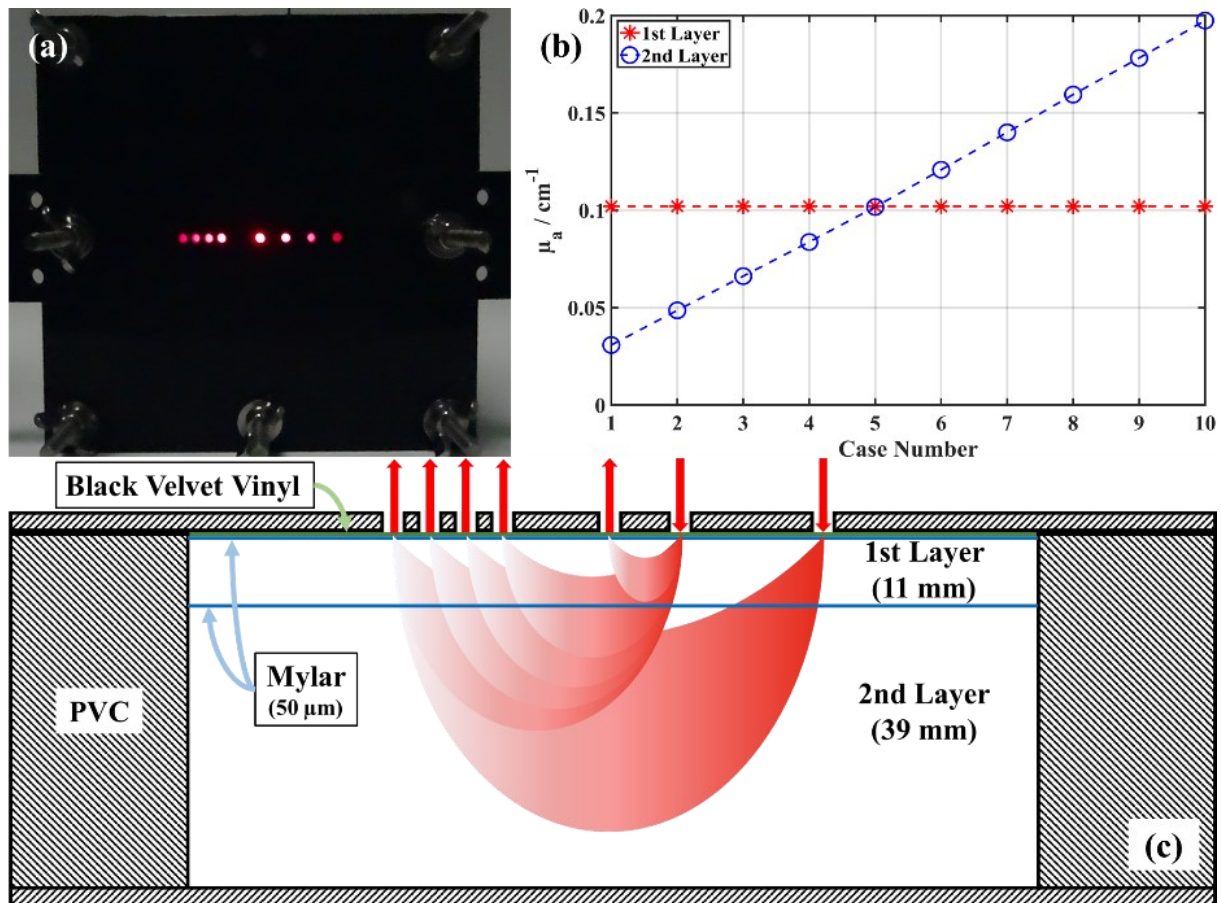


Fig. 5.3. Layered phantom. (a) PVC cell for phantom; (b)  $\mu_a$  nominal values of both layers in ten cases; (c) structure of phantom cell and source/detector positions in the measurements (Reprinted with permission from [II] © Optica Publishing Group).

By a well-accepted methodology [97], the components were first characterized in terms of absorption coefficient for dilute ink's concentration, and of reduced scattering coefficient for intralipid's concentration at the relevant wavelength 830 nm, with independent time-domain measurements. These measurements were performed in transmission and reflection geometries on a homogeneous phantom, i.e. a 3 cm thick black PVC cuboidal cell with small (diameter: 3 mm) transparent circular plexiglass windows [134], containing known concentrations of intralipid and ink. By this characterization, linear relations between concentrations and optical properties are established. Hence, the nominal values of  $\mu_a$ , and  $\mu_s'$  of the layered phantom can be estimated from the concentrations during the preparation procedure. In this work, for the layered phantom, the nominal values of first layer's optical properties ( $\mu_{a1}$ ,  $\mu_{s1}'$ ) are fixed at about  $(0.1, 9.3) \text{ cm}^{-1}$ , whereas the second layer's  $\mu_{a2}$  is varied and investigated in 10 cases in the range  $[0.03 \text{ } 0.2] \text{ cm}^{-1}$  while  $\mu_{s2}'$  is approximately constant at  $9.2\sim 9.3 \text{ cm}^{-1}$ . The slight change on  $\mu_{s2}'$  value is due to the intralipid's concentration change induced by adding small amount of dilute ink during the measurements. The relative uncertainty of the nominal values is evaluated

as approximately 1%. The values for optical properties were chosen to be in a range relevant to brain imaging [31]. Fig. 5.3(b) shows the nominal values of absorption in both layers for the 10 investigated cases. The detailed values are also listed in Table 5.1 in Section 5.5.

As demonstrated in Fig. 3(c), for two-layered measurements, a 50 mm-thick black PVC cell was prepared as the container of the liquid mixture, where the first layer was separated from the second layer and the PVC front wall by two 50  $\mu\text{m}$  Mylar membranes (DuPont, marked by 2 blue lines). The inner width and height of the entire cell are 120 mm and 135 mm. It has been found that the effect of thin Mylar layers in diffuse reflectance measurements can be considered negligible [135]. On the other hand, due to the flexibility of Mylar membranes, the actual thicknesses of the two layers are influenced by the liquid levels of both layers and must be precisely measured for its importance in the correct forward model. For this purpose, an independent experiment was carried out to assess the time difference of perpendicular light echoes from a laser beam hitting both Mylar membranes when the layers were filled with clear water to certain levels. From these measurements, the actual thicknesses in the two-layer configuration were found to be 11.05 mm for the first and 38.95 mm for the second layer.

A slice of black velvet vinyl is glued on the entire inner surface of the PVC front wall (top in Fig. 5.3c, marked by the green line) to prevent stray light travelling along the Mylar surface between injection and collection fibers. The front wall has holes with the same diameter as the fiber ferrules to hold the fibers. Six source-detector distances (10, 25, 30, 35, 40, 60 mm) are included in the diffuse reflectance measurements, for which the assignments are presented in Fig. 5.3(c). The 10 mm measurements are used for determining the first layer's properties, while the other measurements are used for determining the second layer's properties.

### 5.4.3 Monte-Carlo simulations and forward model

To analyze the measurements on the two-layered phantoms, the GPU-based MC program introduced in Section 4.3 was applied for forward simulations of the DTOFs remitted at the  $\rho$  values used in the experiments. To account for side effects caused by the Mylar foils, a four-layer slab geometry was used in the simulations. Hereby, the first and third layer are the Mylar membranes while the second and fourth layer are the compartments containing dilute intralipid and ink. The thicknesses of the layers are  $S_1 = 0.05$  mm,  $S_2 = 11.05$  mm,  $S_3 = 0.05$  mm, and  $S_4 = 38.95$  mm. The refractive indices of Mylar and intralipid are set as  $n_m = 1.65$  and  $n_i = 1.33$  according to literature [99,135]. The ambient refractive indices are  $n_a = 1$  for air and  $n_b = 1.54$  for the bottom PVC wall. The scattering coefficient of Mylar is assumed as  $6 \text{ cm}^{-1}$ . The anisotropy factors of Mylar and intralipid are set as  $g_m = 0.5$  and  $g_i = 0.7$ . It is worth to note that

the  $g$  value does not significantly affect the simulated photons' trajectories for the source-detector distances of interest in this work, whereas the refractive index needs to be assigned correctly since the mismatch at interfaces between different media substantially influences the re-emitted photon's distributions in both time and space domain. Fresnel reflections are taken into account at all the  $n$ -mismatching interfaces. The lateral edges of the phantom cells can be neglected since the measurements were always carried out in the central part of the cell's frontal surface. The high absorption of PVC and the black velvet vinyl also prevented any uncontrolled light guiding propagations along the surface that can hardly be modelled.

To calculate the DTOFs for a single set of the layered optical properties, 300 billion photons are launched into the medium. Simulated photons re-emerging from the slab's surface are recorded on concentric rings surrounding the initial light injection point with a step size of 0.1 mm and a time resolution of 4.07 ps (the time channel width in the TCSPC measurements). Then the simulated DTOFs are convolved with the typical Gaussian beam profile according to the diameter of GI-Fiber 1. The cross section and diameter of GI-Fiber 2 are considered as well by overlaying a circular detection area on the simulation output.

A MC simulation database was created in the form of a look-up table (LUT) of regularly chosen  $(\mu_{a2}, \mu_{s2}')$  combinations for the second layer. Hereby, the parameters  $(\mu_{a1}, \mu_{s1}')$  of the first layer were fixed to the values obtained from the measurement at  $\rho_1 = 10$  mm as described below. The range of  $\mu_{a2}$  was  $[0.02 \ 0.22] \text{ cm}^{-1}$  with a step size of  $0.005 \text{ cm}^{-1}$ , and the range of  $\mu_{s2}'$  was  $[4.5 \ 14.5] \text{ cm}^{-1}$  with a step size of  $0.25 \text{ cm}^{-1}$ . Other possible combinations can be obtained by 2D linear interpolation among the simulated DTOFs of adjacent  $(\mu_a, \mu_s')$  pairs. To separately analyze the measurements for  $\rho_1 = 10$  mm and retrieve the optical properties of the first layer, another MC simulation database was generated by using the geometry of a 50 mm-thick homogeneous slab. These simulations were performed by white MC calculations as described in [69], i.e., with setting  $\mu_a$  of the slab to 0. The desired absorption values would be calculated outside of the MC simulations then. Convolution for finite laser beam and detector size were also done as described above for the layered situation.

#### 5.4.4 Measurement method and inverse procedure

In this work a sequential protocol is designed to retrieve the optical properties of the first and the second layers one after the other. The involved steps are as following:

- (1) Measuring DTOFs at  $\rho_1 = 10$  mm;
- (2) Measuring DTOFs at  $\rho_2 = 25, 30, 35, 40$  and 60 mm and obtaining SRACs in this range;

- (3) Fitting measured DTOFs at  $\rho_1$  with the white MC simulations of homogenous forward model (5 cm-thick slab), to retrieve the optical properties of the first layer;
- (4) Comparing the MC simulations of layered forward model with the measured DTOFs at a selected  $\rho_2$  to calculate the  $\chi^2$  objective function and obtain the  $\chi^2$  distributions for TD, and with the measured SRACs to calculate and obtain the  $\chi^2$  distributions for SD;
- (5) Applying the SeTD method on  $\chi_{ST}^2$  to obtain the optimal  $(\mu_a, \mu_s')$  for the second layer.

The inverse models for TD and SD were applied by using the  $\chi^2$  objective function in Eq. (5.1) whereas for the SeTD method the model was based on Eq. (5.2), to retrieve the optical properties in the second layer. The traversals of all combinations of  $\mu_{a2}$  and  $\mu_{s2}'$  were carried out to evaluate the discrepancy between measurements and forward models and to draw  $\chi^2$  error norm distributions in  $\{\mu_a, \mu_s'\}$  space. The optimal solutions of all the three models are determined at the place where the objective function becomes minimal.

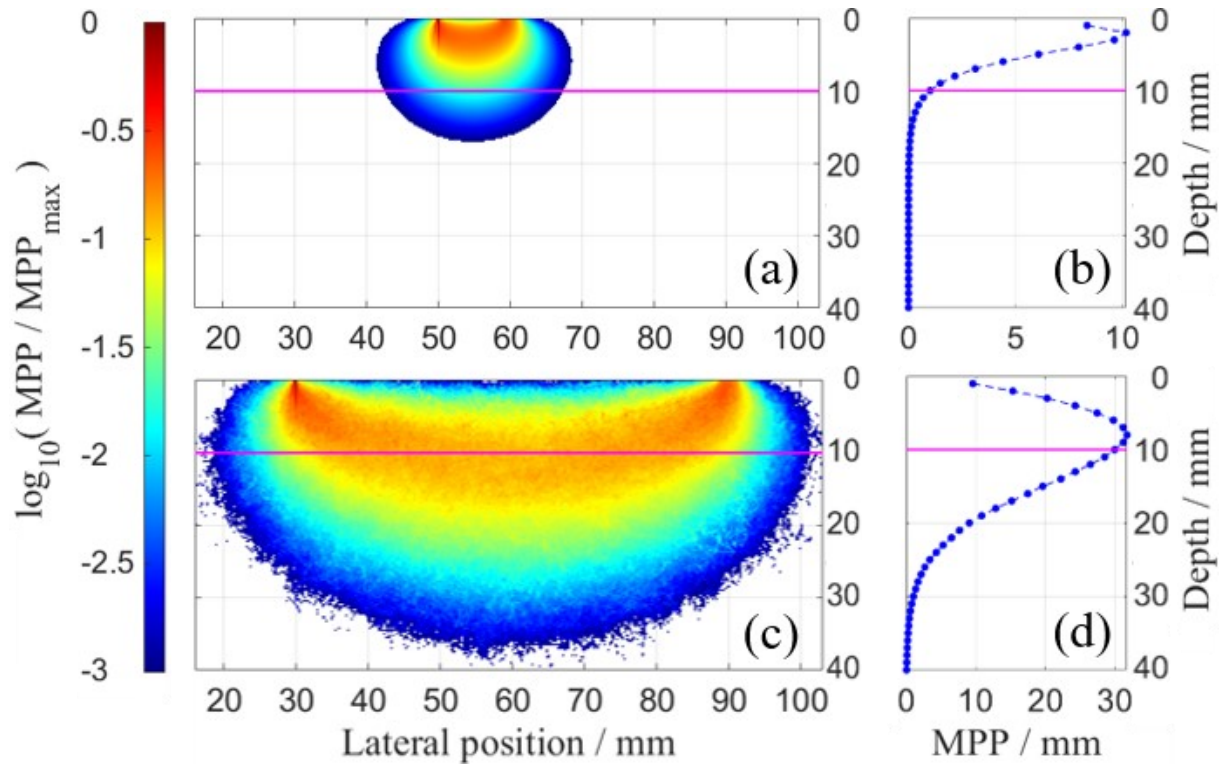


Fig. 5.4. Mean partial pathlength (MPP) for  $\rho_1 = 10$  mm (top row) and  $\rho_2 = 60$  mm (bottom row) of the simulated photons for the layered structure with homogeneous optical properties. (a, c) 2D: MPP values summed along the direction perpendicular to the plane locating the source and detector. (b, d) 1D: Depth profiles of MPP values summed for each 1 mm steps. The purple line highlights the boundary between the first and second layers (Reprinted with permission from [II] © Optica Publishing Group).

Measurements at short ( $\rho_1$ ) and long ( $\rho_2$ ) distances can be used to distinguish and estimate the optical properties of superficial and deep layers, respectively. This prerequisite was proven

by considering the density of the photon trajectories for the different  $\rho$  values. It is well-known that this density follows the so-called “banana shape” [74]. The mean trajectories of detected photons can be visually presented as the spatial distribution of the mean partial pathlength (MPP) values. MPP is the mean length that a photon travels inside a defined volume on its way from the source to the detector. Another type of MC simulation [73], which was modeled in accordance with the phantom structure in section 5.4.2, was applied to illustrate the trajectories of detected photons at various  $\rho$ . This MC simulation in a voxel-based model allows to obtain MPP values for any complex 3D structures with varying optical properties. 5 billion photons were launched for the homogeneous optical properties:  $\mu_a = 0.01 \text{ cm}^{-1}$ ,  $\mu_s' = 1 \text{ cm}^{-1}$ , and  $n = 1.33$ . The voxel size was 0.25 mm in each direction. The results for  $\rho = 10$  and 60 mm are presented in Fig. 5.4. The 2D spatial distribution of MPP values was obtained by summing all voxels perpendicular to the plane locating the source and detector. The distributions demonstrate the expected “banana shape” for short and long distances, i.e., the longer the distance is, the more likely that the detected photons have traveled through the deep region of diffuse media. The 1D depth profiles, obtained by further summing all voxels along the other lateral direction, quantitatively show the depth profiles of MPP values for each 1 mm steps. Almost all photons collected at  $\rho_1 = 10$  mm have travelled in the superficial layer, whereas for  $\rho_2 = 60$  mm a considerable fraction of the collected photons has experienced the region deeper than 10 mm. Therefore, step 1 of the protocol can reliably use the homogenous MC simulations to retrieve the optical properties of the superficial layer, and measurements at step 2 can be used to retrieve the deep layer’s optical properties by using the two-layered MC simulations.

## 5.5 Results

Based on the measurements at  $\rho_2 = 60$  mm as an example, Nominal and retrieved quantities of  $\mu_a$  and  $\mu_s$  of the phantom’s second layer together with their relative errors are summarized in Table 5.1 for all ten cases where  $\mu_{a2}$  increases gradually with a step of about  $0.0185 \text{ cm}^{-1}$ . The procedures for determining the nominal values and their uncertainties were presented in section 5.4.2. More detailed interpretations are subsequently expatiated in subsection 5.5.1 and 5.5.2. The more general analysis of results for the measurements at all  $\rho_2$  are given in subsection 5.5.3.

**Table 5.1. Comparison of nominal values and retrieved values from three approaches (TD: Time Domain, SD: Space Domain, SeTD: Space-enhanced Time Domain) of the second layer's optical properties in ten absorption-incremental cases. The best matches to the nominal values are marked in bold. (unit: cm<sup>-1</sup>).**

**Error denotes the percentage deviation of the retrieved results from the nominal values.**

Case		Nominal		TD (60 mm)		SD		SeTD	
		$\mu_{a2}$	$\mu_{s2}'$	$\mu_{a2}$	$\mu_{s2}'$	$\mu_{a2}$	$\mu_{s2}'$	$\mu_{a2}$	$\mu_{s2}'$
1	value	0.0308	9.39	0.0345	11.15	0.0455	7.75	<b>0.0335</b>	<b>10.20</b>
	error	\	\	12.0%	18.7%	47.7%	-17.5%	<b>8.8%</b>	<b>8.6%</b>
2	value	0.0486	9.38	0.0525	11.15	0.0615	8.28	<b>0.0515</b>	<b>10.10</b>
	error	\	\	8.0%	18.9%	26.5%	-11.7%	<b>6.0%</b>	<b>7.7%</b>
3	value	0.0662	9.38	0.0700	11.85	0.0795	8.30	<b>0.0690</b>	<b>9.88</b>
	error	\	\	5.7%	26.3%	20.1%	-11.5%	<b>4.2%</b>	<b>5.3%</b>
4	value	0.0837	9.35	0.0875	11.33	0.0970	8.25	<b>0.0870</b>	<b>9.65</b>
	error	\	\	4.5%	21.2%	15.9%	-11.8%	<b>3.9%</b>	<b>3.2%</b>
5	value	0.1017	9.34	0.0940	6.10	0.1130	8.25	<b>0.1045</b>	<b>9.15</b>
	error	\	\	-7.6%	-34.7%	11.1%	-11.7%	<b>2.8%</b>	<b>-2.0%</b>
6	value	0.1208	9.33	0.1245	10.60	0.1330	7.85	<b>0.1235</b>	<b>9.10</b>
	error	\	\	3.1%	13.6%	10.1%	-15.9%	<b>2.2%</b>	<b>-2.5%</b>
7	value	0.1400	9.31	0.1360	7.15	0.1485	7.93	<b>0.1415</b>	<b>8.63</b>
	error	\	\	-2.9%	-23.2%	6.1%	-14.8%	<b>1.1%</b>	<b>-7.3%</b>
8	value	0.1594	9.31	0.1640	10.33	0.1645	7.98	<b>0.159</b>	<b>8.35</b>
	error	\	\	2.9%	11.0%	3.2%	-14.3%	<b>-0.3%</b>	<b>-10.3%</b>
9	value	0.1782	9.29	0.1920	13.83	<b>0.1765</b>	7.93	0.175	<b>7.93</b>
	error	\	\	7.7%	48.9%	<b>-1.0%</b>	-14.6%	-1.8%	<b>-14.6%</b>
10	value	0.1974	9.28	0.2190	14.55	<b>0.1975</b>	7.25	0.1895	<b>8.08</b>
	error	\	\	10.9%	56.8%	<b>0.1%</b>	-21.9%	-4.0%	<b>-12.9%</b>

### 5.5.1 Measured data and results of the first layer

As an example of raw data and the inverse analysis procedures, Fig. 5.5 shows some measured DTOFs and their corresponding fitting model counterparts from MC simulations. In Fig. 5.5(a), DTOFs measured at  $\rho_1 = 10$  mm from all 10 cases and the IRF are shown after background subtraction. The DTOFs indicate that an appreciable influence from the second layer on DTOFs only appears in very late time ranges; thus retrieving first layer's properties by fitting the DTOFs at  $\rho_1$  with the MC homogenous forward model is feasible. Fig. 5.5(b) shows an example of the measured DTOF of case 5 at  $\rho_1 = 10$  mm and its optimal MC homogenous fit (Fit performed from 50% of the peak at left, to 0.1% at right of the DTOFs. Time 0 is defined as onset of the IRF), and the flat fitting residuals represent high fit quality. By analyzing DTOFs at  $\rho_1$ , the optical properties of the first layer are retrieved as  $(\mu_{a1}, \mu_{s1}') = (0.100, 9.71)$  cm<sup>-1</sup>, with the deviations (-2.0%, +4.0%) from the nominal values (0.102, 9.34) cm<sup>-1</sup>.

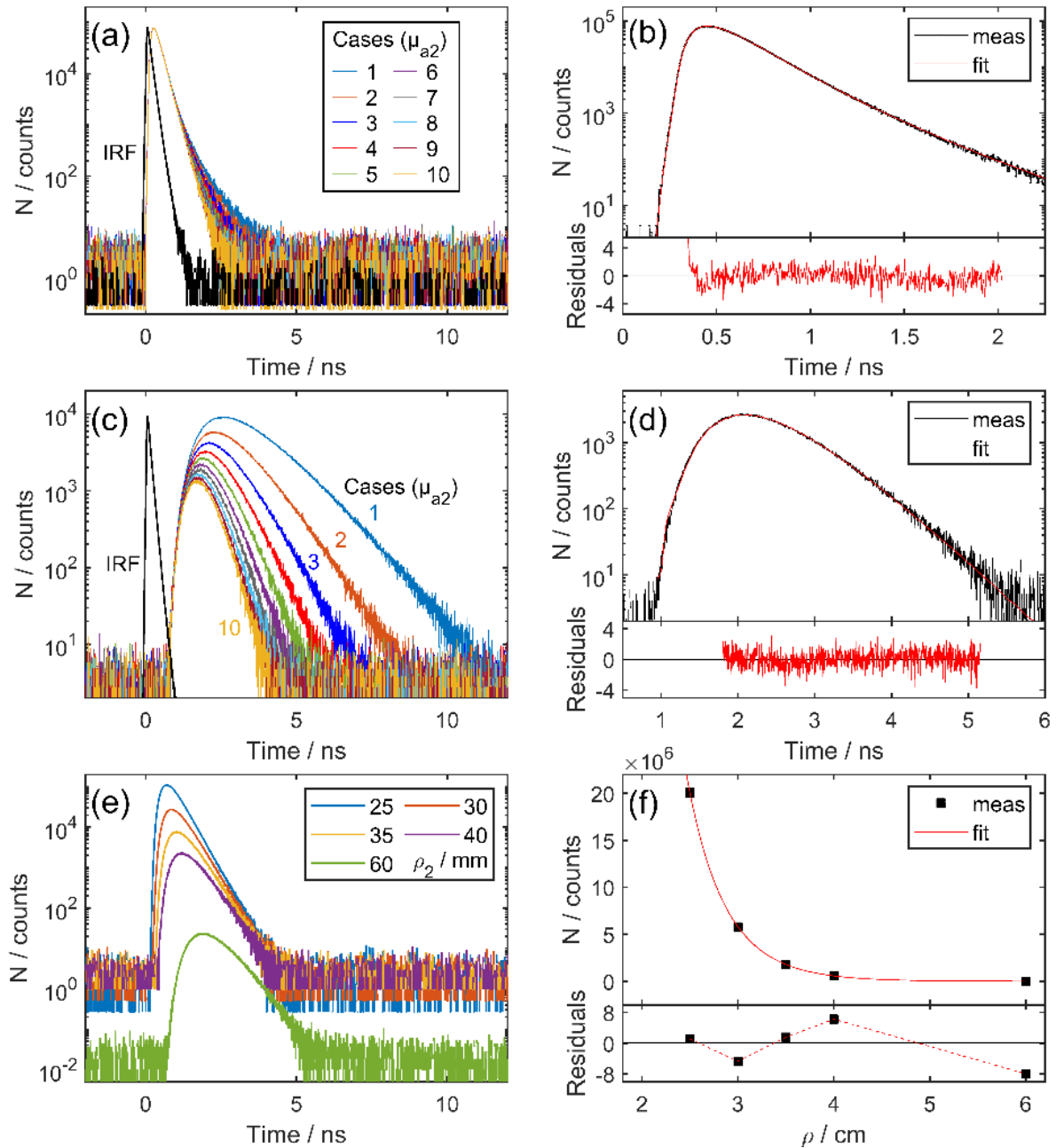


Fig. 5.5. (a) DTOFs measured at  $\rho_1 = 10$  mm for the 10 cases of  $\mu_{a2}$ . (b) Fit for case 5: DTOFs at  $\rho_1 = 10$  mm, the optimal fit from homogenous MC and the weighted residuals. (c) DTOFs measured at  $\rho_2 = 60$  mm for the 10 cases. (d) Fit for case 5: DTOFs at  $\rho_1 = 60$  mm, the optimal fit with layered MC and the weighted residuals. (e) DTOFs measured at  $\rho_2 = 25, 30, 35, 40,$  and  $60$  mm (after attenuation filter correction) for case 5, to calculate the SRAC. (f) SRAC for case 5 in selected  $\rho_2$  range, the optimal fit with layered MC and the weighted residuals (Reprinted with permission from [II] © Optica Publishing Group).

Contrarily as depicted in Fig. 5.5(c), the prominent effects from the second layer on DTOFs measured at  $\rho_2 = 60$  mm, show that the changes of  $\mu_{a2}$  alter DTOFs throughout their profiles from early time ranges. As one example for the TD inverse process using the MC layered forward model to retrieve optical properties of the second layer, Fig. 5.5(d) shows the

measured and the simulated DTOF for case 5 at  $\rho_2 = 60$  mm. The flat residuals vs. time indicate a very good agreement between both curves. A small (for the case of Fig. 5.5(d) the minimal)  $\chi^2$  value is obtained, representing the optimal TD solution in  $\{\mu_a, \mu_s'\}$  space. In the analysis here, the TD fits are all performed from 80% of the peak at left, to 0.1% at right of the DTOFs, i.e., almost the whole DTOFs; so all time-resolved information from both layers is considered.

In this work the integrals of photon counts over all time channels, after background subtraction, are used as the SD light intensity information (SRACs). Regions after pulses could be included here thanks to the clean tails of the DTOFs. Fig. 5.5(e) shows DTOFs at all  $\rho_2$  (25, 30, 35, 40, and 60 mm) for case 5. All DTOFs at first 4  $\rho_2$  are measured with same filter setting while the DTOF at 60 mm is rescaled based on the ratio of filter settings. Note that it is not mandatory to measure all DTOFs with the same filter settings. In practice, appropriate filter ratios and corrections can improve the dynamic range for photon counts. The integrals of DTOFs at all  $\rho_2$  formed the SRAC in Fig. 5.5(f). After applying the SD inverse model, the optimal layered MC fit can be obtained when the  $\chi^2$  value is minimal.

### 5.5.2 Results of the second layer based on different methods

Table 5.1 provided the overview of the final quantitative results by all three methods, but the comparison of the methods and the trend of the results deserve more attention. In Fig. 5.6 we present the complete knowledge of the detailed  $\chi^2$  error norm distributions in the  $\{\mu_a, \mu_s'\}$  space under TD, SD, and SeTD method for representative cases 1, 3, 5, 6, 8, and 10. Such error norm surfaces, containing information from TD or SD observations of photon propagation in diffuse media, can be regarded as the temporal or spatial projection of the optical absorption and scattering features on the  $\{\mu_a, \mu_s'\}$  space. To illustrate the relative deviations despite the large span of  $\mu_{a2}$  for the different cases, the horizontal axis ( $\mu_{a2}$ ) is always given in relative units with respect to the nominal values. While the vertical axis ( $\mu_{s2}$ ) is accordingly given in absolute units such that it has the same number of pixels as the horizontal axis. The ratio of  $\mu_{s2}$  range and  $\mu_{a2}$  range keeps the same for all cases so that details in all the subplots are visible and comparable.

Like the results of the simulations in Fig. 5.1, it can be clearly noticed that the effects from  $(\mu_{a2}, \mu_{s2}')$  properties of the measured phantoms are complementary and symmetric with respect to the  $\chi^2$  error norm surface on TD and SD. As for TD shown in the first column of Fig. 5.6,  $\mu_{a2}$  and  $\mu_{s2}'$  generally exhibit a positive correlation, whereas for SD shown in the second column, they are negatively correlated. Such opposite correlations lead to different profiles and orientations of the low- $\chi^2$  region in the  $\{\mu_a, \mu_s'\}$  space. Although one can still get an optimal solution by both TD and SD methods, i.e. a  $\chi^2$  minimum at one  $(\mu_{a2}, \mu_{s2}')$  combination marked

as yellow and green crosses in Fig. 5.6, they are always quite unstable and sensitive to noise. A small perturbation on measurements may lead to a big deviation from the true values, as implied by the elongated dark red regions (enclosed by yellow contour lines) on the  $\chi^2$  error norm surface of TD and SD.

In the third column of Fig. 5.6, the above-mentioned complementarity is utilized to carry out the SeTD method by combining TD and SD information, Thereby, more well-defined  $\chi^2$  minima, as the consequence of the better convergence of  $\chi^2$  error norm surface, can always be obtained by the SeTD method to get optimal solutions of the inverse problem. As explained before, effective mutual complementation is crucial to achieving the convergent results.

Based on Fig. 5.6 and Table 5.1, several important points should be noted:

- (1) The yellow contour lines in the 1st column of Fig. 5.6 enclose the dark red region where  $\chi^2$  values are smaller than 2 times the minimal  $\chi^2$  on the entire error norm surface of the TD method. Although the nominal values (white X crosses) always fall into these regions, the retrieved results (yellow crosses) appear in distance from them due to the error norm's resemblance within low  $\chi^2$  region during the inverse process. The flatness within the low  $\chi^2$  region indicates that these  $(\mu_{a2}, \mu_{s2}')$  combinations in the region are practically identical for the solver and implies the non-uniqueness of the TD solutions.
- (2) The SD  $\chi^2$  error norm surface in the 2nd column of Fig. 5.6 is comparably much steeper. And consequently, the yellow contour lines enclose a smaller and more confined region with convergent low  $\chi^2$ . However, the nominal values hardly fall into these regions, which makes the simultaneous recovery of absorption and scattering nearly impossible. The retrieved results (green crosses) still appear in some distance from nominal values. At the cost of the underestimating  $\mu_{s2}'$ , the retrieval performance of  $\mu_{a2}$  is quite unstable among the cases, which is shown in the third column of Table 5.1 as well.
- (3) The TD low  $\chi^2$  regions, i.e. the red flat strips of the error norm surface in Fig. 5.6, are roughly parallel to the  $\mu_{s2}'$  axis, which denotes that  $\mu_{s2}'$  has very little influence on the DTOF shape of the diffuse reflectance. Namely, it is nearly impossible to determine  $\mu_{s2}'$  through TD information alone. Such uncertainty also manifests itself as the big deviation of the TD retrieved  $\mu_{s2}'$  from nominal values shown in the second column of Table 5.1. For the cases which  $\mu_{a2}$  values are not far from  $\mu_{a1}$  values, it is particularly apparent that even if the retrieved  $\mu_{s2}'$  is inaccurate, it is nonetheless still possible to obtain  $\mu_{a2}$  with reasonable accuracy by the TD method. While for the cases with stronger contrast between layers, this " $\mu_{s2}'$  neutrality" declines to a certain extent and the ambiguity of  $\mu_{a2}$  and  $\mu_{s2}'$  increases again.

(4) The SD low  $\chi^2$  regions, i.e. the elongated “valley” enclosed by yellow contour lines, are turning towards the vertical direction with increasing  $\mu_{a2}$ . The trend of retrieval error  $\mu_{a2}$  in Table 5.1 indicates that the SD method is more sensitive to high absorption in the second layer. However, it is important to note here that the  $\chi^2$  minimum cannot be well allocated due to the occurrence of several local minima along the valley center line caused by noise. Furthermore, the results for the SD method in Table 5.1 and Fig. 5.6 are based on the assumption of Poisson noise. Repeated measurements show that the noise of the SD intensities is larger and amounts to about 1% , most likely due to fluctuations of the laser intensity. Taking the increased noise into account we observe a shift of the  $\chi^2$  minimum along the valley center line towards the upper left direction. Overall, the stable information from the SD method is that all combinations of  $\mu_a$  and  $\mu_s'$  along the valley center line are consistent with the experimental data. This line can be interpreted, at least qualitatively, as an effective attenuation, defined as  $\mu_{\text{eff}} = (3\mu_a \mu_s')^{1/2}$ . Generally, the non-uniqueness of the SD method discussed in [88] takes effect here as well.

(5) Likewise to the SD method, along with increasing absorption in the second layer, the low- $\chi^2$  regions become broader for TD method, too. This is due to the relatively fewer collected photons in the later time ranges, which have experienced the second layer and then survived to the exit surface. In general, lower signal-to-noise ratio (SNR) will always cause a higher uncertainty. Under lower SNR conditions (low photon counts or high noise), the retrieval accuracy for both absorption and scattering would be reduced, since an error in one unknown would manifest itself as an artefact to the other.

(6) As can be seen from the bold values in Table 5.1, SeTD reached the best performance among the 3 methods for almost all cases. It always derives the  $\mu_{s2}'$  values closest to the nominal values. The accuracy is also improved for  $\mu_{a2}$  when comparing with original results from the TD method. A well-defined convergence in the  $\{\mu_a, \mu_s'\}$  space is obtained for all cases by SeTD. As illustrated in the 3rd column of Fig. 5.6, the SeTD method maintains the “ $\mu_{s2}'$  neutrality” from TD and, at the same time, benefits of the steepness and convergence in the low  $\chi^2$  regions from SD. With the SeTD method, the advantages from both TD and SD are effectively combined through mutual complementation.

By the SeTD method, not only the ambiguity area of low- $\chi^2$  region can be reduced, but also the crosstalk among  $\mu_{a2}$  and  $\mu_{s2}'$  can be restrained. The entangled contributions from scattering and absorption are decoupled in this artificial spatio-temporal projection  $\chi_{ST}^2$  by integrating SD and TD information.

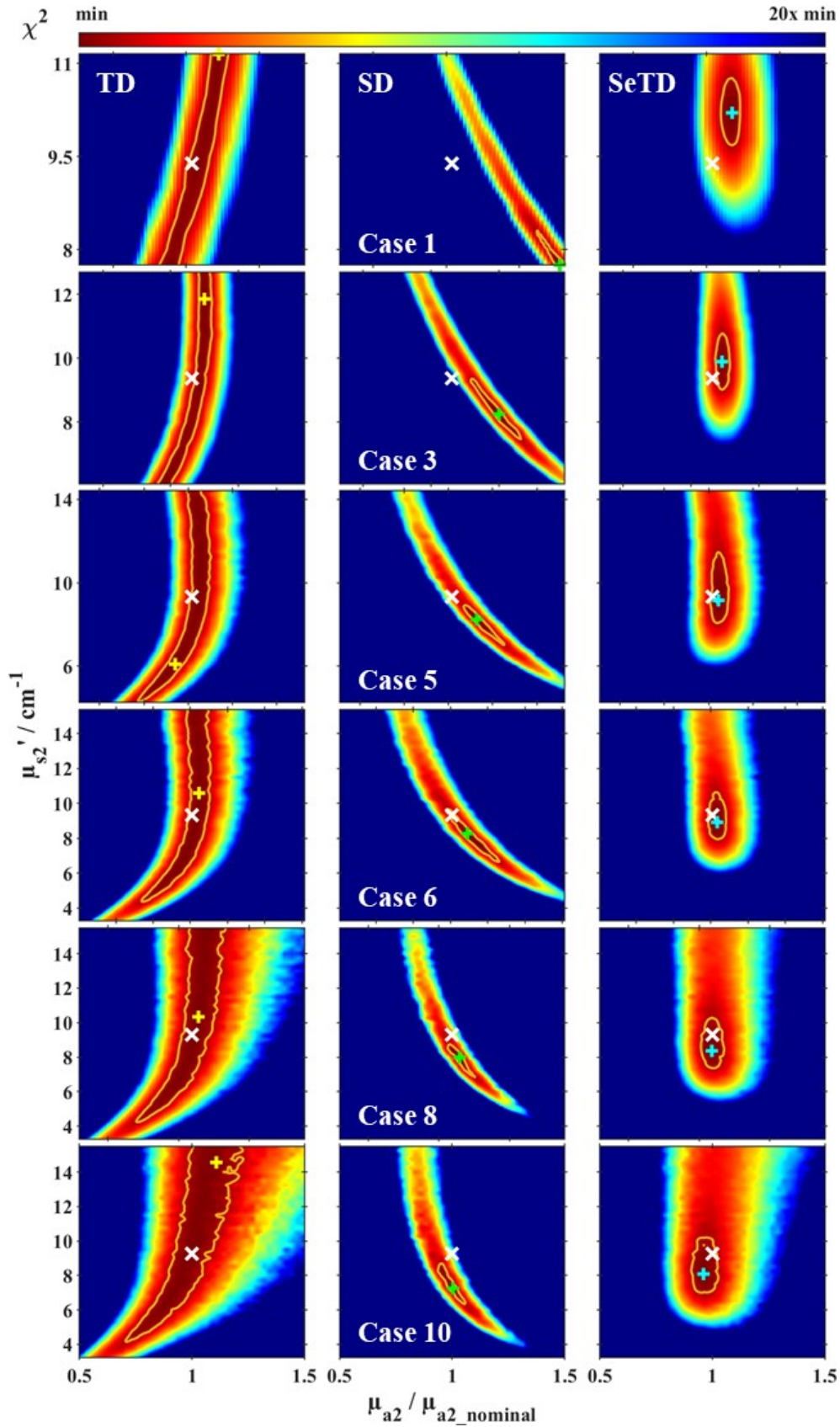


Fig. 5.6.  $\chi^2$  distributions in the  $\{\mu_a, \mu_s'\}$  space. From left to right: TD ( $\rho = 60$  mm), SD, and SeTD; from top to bottom: case 1, 3, 5, 6, 8, and 10. Note that in cases 1 and 3  $\mu_{a1} > \mu_{a2}$ , in case 5  $\mu_{a1} \approx \mu_{a2}$  and in cases 6, 8 and 10  $\mu_{a1} < \mu_{a2}$ . White  $\times$  crosses are the nominal values, yellow, green, and cyan  $+$  crosses are the optimal solutions for TD, SD and SeTD, respectively. Yellow contour lines surround the areas where  $\chi^2$  values are smaller than 2 times minimal  $\chi^2$  (Reprinted with permission from [II] © Optica Publishing Group).

## 5.6 Performance Metrics

In order to compare the performance of the SeTD method with respect to the TD and SD methods more quantitatively, two metrics are used to characterize the retrieval of optical properties: error and linearity.

**Error:** The retrieved values and relative errors, i.e.  $(\text{retrieved } \mu / \text{nominal } \mu) - 1$ , were shown in Table 5.1. However, unlike the SD method which always gains the information from all  $\rho_2$ , the TD results shown are obtained from the measurements at  $\rho_2 = 60$  mm, and the SeTD results shown includes the TD information from  $\rho_2 = 60$  mm as well. According to our analysis, although there is no systematic dependence of the results on  $\rho_2$ , the TD measurements at different  $\rho_2$  would lead to varying results for  $\mu_{a2}$  and  $\mu_{s2}'$ . In other words, the retrieved optical properties from the TD method depend on the location where the measurements took place and thus are unreliable. We considered the retrieved  $\mu_{a2}$  and  $\mu_{s2}'$  values from measurements at  $\rho_2 = 25, 30, 35, 40, 60$  mm for all 10 cases respectively, and then calculated distributions of the TD and SeTD results at those  $\rho_2$  to draw box plots for  $\mu_{a2}$  and  $\mu_{s2}'$  and their corresponding relative error with regard to nominal values.

The distributions of retrieved values of  $\mu_{a2}$  and  $\mu_{s2}'$  from the TD and SeTD methods at different  $\rho_2$  are shown in Fig. 5.7(a) and 5.7(b). Clearly distributions from TD are much broader and hence the variances are bigger. Along with the increase of  $\mu_{a2}$ , the deviation becomes more apparent. In Fig. 5.7(c) and 5.7(d) the relative errors (bias with respect to the nominal values) are presented for the comprehensive investigation between cases of different  $\mu_{a2}$ . For  $\mu_{a2}$ , the SeTD relative errors clearly stand out for cases 4 to 10. Only for low absorption (cases 1 to 3), where small absolute deviations lead to bigger relative errors, relatively broad distributions are visible in SeTD relative errors. However, low absorption in the deep layer is neither realistic nor of practical interest under *in vivo* conditions [31]. On the other hand, for  $\mu_{s2}'$ , the results of all cases show the SeTD can provide more accurate and reliable values than TD at all source-detector distances. In general, the distributions of results from the SeTD method at different  $\rho_2$  are much narrower and the medians of the relative errors are closer to zero, i.e., the SeTD results are largely independent of the source-detector distance at which the TD measurements taken, and have both low variance and low bias with respect to the nominal values.

Another relevant component of uncertainty of the retrieved values for  $\mu_{a2}$  and  $\mu_{s2}'$  is the uncertainty of the determined parameters of the first layer, i.e.  $\mu_{a1}, \mu_{s1}'$  and its thickness. In order to assess this influence we varied the first layer parameters  $\mu_{a1}$  and  $\mu_{s1}'$  retrieved by the TD analysis at  $\rho_1 = 10$  mm sequentially by  $\pm 9\%$ , and  $\pm 5\%$ , respectively. In two further investigations we considered deviations of the first layer thickness by  $\pm 10\%$ . The MC database

was extended accordingly. The analyses of the six deviation situations showed that the relative errors of  $\mu_{a2}$  values from SeTD generally remain within  $\pm 10\%$ , with very few exceptions mostly in the cases of lowest and highest  $\mu_{a2}$ . Comparatively speaking, SeTD performed clearly better than SD and TD in general. SeTD results surpass those of TD and SD methods for most  $\mu_{a2}$  cases. The  $\mu_{a2}$  relative errors from SD are generally the largest, and those of TD are much less stable. For the situation of + 10% thickness., a pattern with negative relative errors for small  $\mu_{a2}$  cases and positive relative errors for large  $\mu_{a2}$  cases was observed, with a nearly linear trend in between. The pattern was inverted for the situation of - 10% thickness.

For  $\mu_{s2}'$ , the relative errors for all six situations introduced were enlarged for all methods (SD, TD, SeTD). However, the errors from SeTD are smaller than those from TD and SD and are at the same level as the values shown in Fig. 5.7d. Having in mind that the most relevant parameter in physiological context is  $\mu_{a2}$ , the SeTD method is sufficiently stable with respect to errors in the first layer parameters.

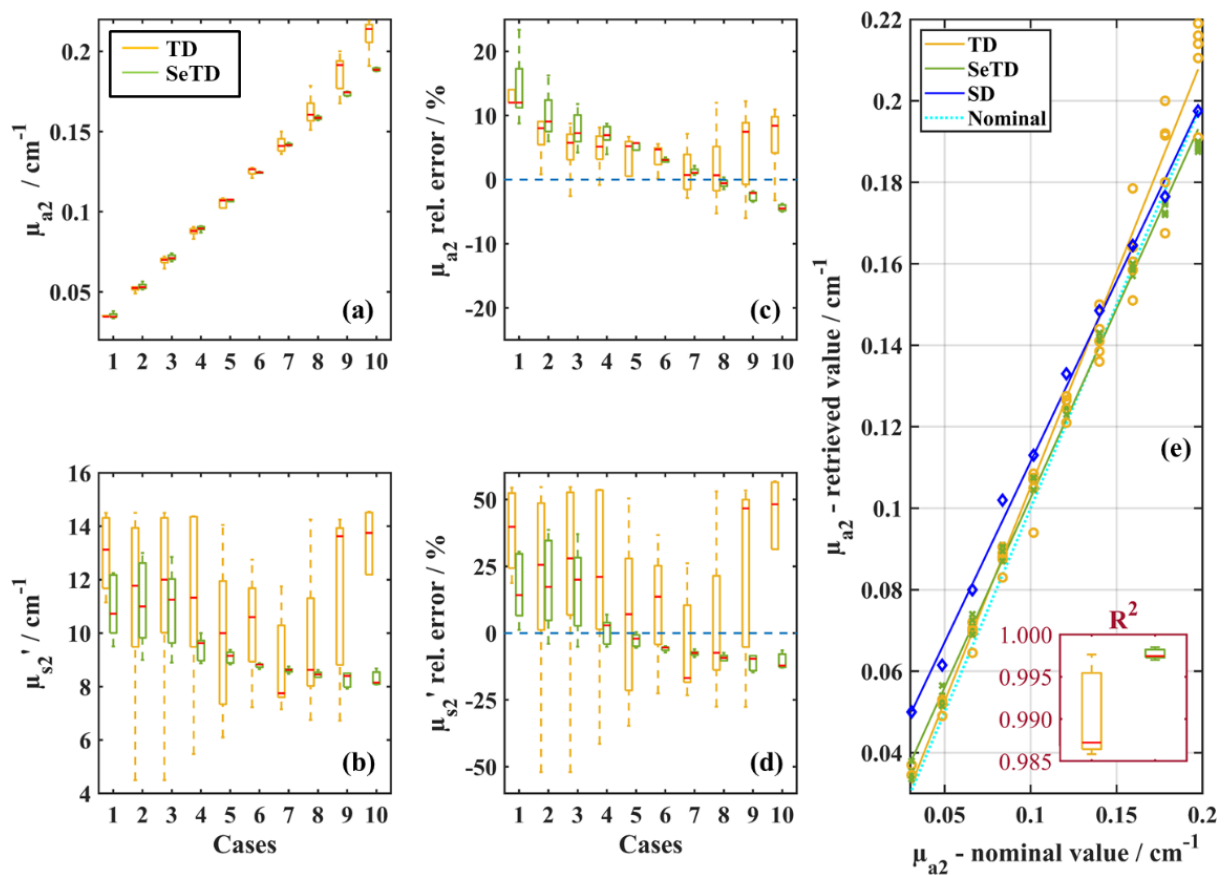


Fig. 5.7. TD and SeTD comparison of distributions of the results from measurements at different  $\rho_2$  for (a)  $\mu_{a2}$  and (b)  $\mu_{s2}'$ . The corresponding relative error distributions for (c)  $\mu_{a2}$  and (d)  $\mu_{s2}'$ . (e) Linearity of the TD, SD, and SeTD methods and  $R^2$  distribution over different  $\rho_2$  for TD and SeTD methods. Red lines in the boxes indicate the median, bottom and top edges indicate the 25th and 75th percentiles, and whiskers indicate the minimal and maximal values (Reprinted with permission from [II] © Optica Publishing Group).

**Linearity:** Linearity here stands for the linear dependence of retrieved  $\mu$  against the nominal  $\mu$ . This metric could provide an effective way to evaluate how well a method can detect the changes in the deep layer without distortions. Also, even if one method retrieves absolute values of  $\mu$  with an insufficient accuracy, the values of relative changes could still be assessed when the method's linearity is satisfactory.

We performed a linear fit of the retrieved  $\mu_{a2}$  values versus their nominal values for TD, SD, and SeTD methods, and obtained the linearity by the fit slope and the coefficient of determination  $R^2$  for the goodness of fit. The linear fits are plotted in Fig. 5.7(e), in which the  $\mu_{a2}$  results from various  $\rho_2$  are marked as symbols (note that for SD method the symbols represent the results from all  $\rho_2$ ). The lines are the linear regression for the median of these results from various  $\rho_2$ , taking into account uncertainties of  $\mu_{a2}$  derived from the difference of 25th and 75th percentiles for TD and SeTD. Firstly, the slopes of lines from TD, SD, and SeTD methods are  $1.02 \pm 0.01$ ,  $0.89 \pm 0.02$ , and  $0.95 \pm 0.02$ , respectively, indicating that in the sense of linearity the SeTD method shows the combination of TD and SD information as well and can comparably detect and maintain the information about relative changes without distortions over a long dynamic range of  $\mu_{a2}$ . On the other hand, the median  $R^2$  values, as shown as the red lines of boxplot in Fig. 5.7(e), are  $R^2 = 0.9872$  for TD method and  $R^2 = 0.9974$  for the SeTD method, showing the more determined linearity of the SeTD method and its  $\rho_2$ -independence.

Overall, compared to single-domain methods, the SeTD method can always provide the best performance on error and linearity for retrieval of absorption in the deep layer, and can be independent of the source-detector distance of measurements to a substantial degree. In other words, owing to the better fault tolerance of many conditions during practical measurements, e.g., noise, precise source-detector distance, and accurate superficial layer's optical properties, the SeTD method can provide more certain and reliable absolute quantity and relative change for deep layer absorption's assessment.

## 5.7 Discussion

The effects of absorption and scattering are entangled in different ways for the measurands in TD and SD. The methodology of the SeTD approach on solving the entanglement, is to integrate the observations from different domains by considering the intrinsic independence nature of absorption and scattering, so as to give the most optimal solution of the ill-conditioned inverse problem.

The SeTD method was experimentally validated by using a two-layered liquid phantom with constant optical properties in the first layer and ten different values of optical properties

(primarily absorption) in the second layer. Measurements were carried out at one short source-detector distance and five long distances to distinguish the influences from the first and second layer on diffuse reflectance. The analyses were carried out by TD, SD and the SeTD methods, with Monte-Carlo simulations as the forward model. The retrieved values and error norm distributions on  $\{\mu_a, \mu_s'\}$  space showed that:

- (1) For TD method, the error norm is sensitive to the change of absorption in the second layer, while it is virtually insensitive to scattering in the second layer, i.e., the temporal profiles of diffuse reflectance are practically insensitive to  $\mu_{s2}'$ . As introduced above by the term of “deep scattering neutrality”, it is nearly impossible to simultaneously recover  $\mu_{a2}$  and  $\mu_{s2}'$  through TD alone, if no *prior* knowledge is provided.
- (2) For SD method, under the presence of complex noise, the retrieval performance is bad and the uncertainty is high. Due to the limited information one can acquire from SD, the solutions of  $\mu_{a2}$  and  $\mu_{s2}'$  with the most confidence, i.e. the low- $\chi^2$  region on the error norm distribution, always appear at some distance from the nominal values, indicating that it is hard to retrieve absorption and scattering in the second layer through the SD method alone.
- (3) For both TD and SD methods, there is no clear convergence on the error norm distribution for the second layer’s properties, indicating that the ambiguity within the low- $\chi^2$  region of error norm distributions would make the retrieval unstable. Conversely, for the SeTD method, better convergence of the error norm can be achieved, which yields a well-defined and reliable solution. In all measured cases, the  $\mu_{a2}$  accuracy is improved in comparison to the results from conventional TD, and the most accurate  $\mu_{s2}'$  values are always from the SeTD method as well.

If polarization is not considered, in diffuse optics the space-resolved distributions of times of flight of photons represent the maximal information that can be gained from the reflectance scattered field at a single optical wavelength, but also sufficient information for deducing the knowledge of an object’s interior optical absorption and scattering properties when its layered structure is known. In the present work, by taking advantage of the fact that the error norm distributions of TD and SD information are complementary, we combined these information in an artificial spatio-temporal  $\chi_{ST}^2$  on  $\{\mu_a, \mu_s'\}$  space, to give the optimal quantitative estimate of optical properties in both layers. Instead of measurements requiring a lot of time-domain measurement channels covering a large dynamic range and at various source-detector distances, the SeTD method would only require a short and a long-distance TD measurement combined with a multi-distance SD measurement. It is also worth to note that although in this study

DTOFs were recorded at all  $\rho$ , it is not a necessary condition for the feasibility of the method. In practice, time-resolved measurements are necessary only at one short and one long distances, while space-resolved amplitude information for the intermediate distances can be accurately obtained by any CW multi-distance detection system. Moreover, rather than isolated fittings between measurements and forward models as single-domain methods focus on, the SeTD method concerns more about the complementary correlations in different domains. The SeTD method takes advantages from and restrains the disadvantages among the domains, to ensure the accuracy and uniqueness of the inverse solution.

In short, for the measured cases, the SeTD method has presented its ability to roughly restrain the retrieval error within 5% for  $\mu_{a2}$  and 10% for  $\mu_{s2}'$ , under the condition that the ratio  $\mu_{a2}/\mu_{a1}$  ranges from 0.3 to 2. In previous studies, other researchers have reached similar levels of accuracy on  $\mu_{a2}$  with different approaches, e.g., TD multi-distance measurements with MC simulations [12], TD single distance measurements with optimal estimation algorithm [127], FD multi-distance with diffusion forward model [11], and two-distance TD and SD measurements with an improved diffusion model [128]. In these studies,  $\mu_{s2}'$  was always estimated with large uncertainty due to the aforementioned “ $\mu_{s2}'$  neutrality” phenomenon. To the best of our knowledge, the accuracy level of  $\mu_{s2}'$  achieved here sets a cutting-edge benchmark. Moreover, the SeTD method overcomes some practical problems of single-domain methods, for instance the high uncertainty when measuring at different source-detector distances with the TD method, and the high cross-talk between unknown absorption and scattering with the SD method. The retrieved values by SeTD are independent of the location of the TD detection, and exhibit strong resistance against the cross-talk and the influence of noise owing to the convergence of the error norm. Linearity of SeTD also surpasses single-domain methods, which is crucial for representing changes even if the absolute estimates of optical properties are insufficiently accurate. The SeTD method was also found to be less sensitive for errors in the first layer parameters than the TD and SD methods.

If DTOFs at all relevant  $\rho_2$  have been recorded, a TD global fit could be performed as an alternative to the SeTD method. Such fit contains the SD information in a different manner than SeTD, since it takes the positions of the different DTOFs on the time axis into account. In this way, systematic deviations between experimental and theoretical maxima of the DTOFs could occur. Furthermore, the IRF plays a stronger role than in the SeTD method. The accurate measurement of the IRF is challenging, for it should reflect the illumination of the detection fiber exactly in the same manner as with diffusely reflecting phantoms. The SD information

utilized as part of the SeTD method does not depend on the IRF. Hence, the SeTD method overcomes some difficulties related to TD global fit.

There are also limitations of the present study. Firstly, the physical structure of the phantom investigated here is still simplified, although closer to reality than homogeneous ones. It consists of a slab with only 2 layers, and the thickness of the first layer is assumed to be known. Secondly, the optical properties of the first layer have not been changed during the measurements, since we mainly focus on the retrieval performance of the optical properties of the second layer. Finally, despite the absorption in the second layer is investigated for 10 different cases, the scattering is assumed as being homogenous for both layers during the measurements although the values of scattering are considered as unknown. These simplifications may limit the ability of SeTD method to reflect the reality. Further studies will require investigations on complex structures with heterogeneous optical properties.

## **5.8 Conclusion**

In this study we have developed a new multi-domain approach, namely Space-enhanced Time Domain (SeTD) method, to simultaneously retrieve the absolute quantities of optical absorption and scattering properties in two-layered turbid media. The new methodology of the SeTD method integrates the TD and SD information to give the most optimal estimate of the ill-conditioned inverse problem, rather than isolated fittings of various data types from individual domains. The “deep scattering neutrality” is investigated and summarized in the form of error norm surface. The accuracy, reliability and linearity of the SeTD method are demonstrated to be better than those of the single-domain methods. While the present study was carried out in the near- infrared spectrum, similar methodology and principle could be applied in other spectral ranges so that the method may be used for other general scenarios besides tissues. For the case of measuring at low photon counts, the method also has the potential to obtain more reliable results under the condition of substantial noise. Besides, the concept of merging data from different domains may indicate a new way of solving inverse problems in diffuse optics, namely the integration of different kinds of data types and measurands, such as temporal and central moments of DTOFs, time windows, and frequency domain quantities.

# 6

## Current Limitations

As the methodology integrating and optimizing information from multiple domains in diffuse optics is still developing, inevitably, there are still several limitations in the perspectives of theory and implementation. The currently existing limitations are summarized in this chapter, as well as the potential limitations envisaged.

### 6.1 Methodological limitations

Although most of tissue structures can be well simplified as layered, they are much more complex in reality. The first methodological limitation of the present method is that the results with high space-resolution will require numerous Monte-Carlo computations in advance so that the simulations can fit with measurements. With more complex anatomical structures to be included in the consideration, the permutation and combination of optical properties in different tissue compartments would be much more and thus the degree of freedom in Monte-Carlo computations would also increase exponentially. For the further development of this method, a mesh-based Monte-Carlo solution with the principle of finite element method shall be considered to reduce the computation volume raised by structural complexity.

The second methodological limitation involved is the diversity and individual variations of optical properties of inter- and intra-subject. The chromophores and their concentrations in different regions of tissues constitute the total quantities of optical properties. For different parts of tissue investigated, as well as for different groups of people (e.g. infant and adult), the dynamical ranges of optical absorption and optical scattering can be in different orders of magnitude. And the optical complexity and heterogeneity would also sometimes cause a large volume of unnecessary simulations. A more comprehensive investigation on the approximate optical properties of different tissue compartments and different object groups is needed as the *prior* knowledge for the method in this thesis.

The last methodological limitation arises from the cross-talk of the retrieved results from different compartments of studied tissues. Theoretically, any error of the Monte-Carlo model's parameters, such as thickness of layers, refractive index, and optical properties of another

compartments of tissues, could propagate to the optical properties to be investigated and therefore causes inaccuracy. According to the present study, the SeTD method shows a much stronger resistance to the error arisen from thickness of layers and optical properties of superficial layers, compared with TD and SD method. But the error from refractive index could lead to a so-called “ $\rho$ -dependency”, i.e., the retrieved optical absorption and scattering coefficients are dependent on the source-detector distance of measurements. It is also shown that the correct refractive index set in the Monte-Carlo model is even decisive to the accuracy of final results on optical absorption and scattering coefficients. For the effective implementation of the method in this thesis, the knowledge on the precise refractive indices of tissues is well necessary.

## 6.2 Instrumental limitations

The method developed in this thesis requires photon detecting in time domain and space domain. Thereupon there are instrumental limitations from both TD and CW modalities.

The main instrumental limitation is about the applicability in practice. Since the detectors used are mainly Hybrid PMT detectors, the application of the method can hardly be exposed in the environment of high ambient light. Deployment of SPAD or other detectors may relief this limitation, but could also introduce undesirable features on IRF.

The second instrumental limitation concerns about the tradeoff between accuracy and portability, which involve all components of instrumentation. The bulky light sources, detectors, and timing electronics generally provide better time resolution and accuracy, whereas the diode-based lasers and detectors have much better compactness and integrability in the sacrifice of accuracy. Further developments on integrated optoelectronics are looked forward.

The last instrumental limitation is about the computation ability and the temporal resolution influenced by the step-by-step measurement protocol. High computation volume of Monte-Carlo simulations is required in advance of the measurements and during the online measurements. Therefore, the prompt in-vivo monitoring is *de facto* bottlenecked by the computation capacity. If the high computing power is not realistic, algorithms that can circumvent unnecessary simulations should be designed in the future.

# 7

## Conclusion and Prospect

Committed to the improvement of the quantification of the absolute values of optical absorption and optical scattering in random media, this work focused on the investigation of the fundamental features of diffuse light propagation, and developed an innovative methodology to combine the information from various domains and hereupon increased the accuracy to the level of 5% and reduced the uncertainty by half for both optical absorption and scattering coefficients.

This thesis started with the attempt of solving the most difficult kind of inverse problems in diffuse optics: the absolute imaging and estimating absolute optical properties from external measurements. This inverse problem is nonlinear, ill-posed and, under some specific conditions even non-solvable. To solve the inverse problem, this work first reviewed all the forward models in diffuse optics based on distinguishably different theory background, and adopted Monte-Carlo method, the computational modelling of radiative transport equation in diffuse optics, as the forward simulation & prediction method.

Unlike most of the previous studies on solving the inverse problem which constrained themselves in single domains, this thesis investigated the origins and fundamentals of the optical absorption and scattering in multiple dimensions. The phenomena of optical absorption and scattering, to the very basic nature of them, are independent, while their effects on the measurements (or in other word, the observations towards absorption and scattering) are always highly entangled in every domain (time, space, frequency, etc.). In this thesis, for the first time the complementarity of the effects of optical absorption and scattering in time domain and space domain are discovered and exploited. It has been found, that by establishing a hybrid domain that dynamically integrating information from the measurements in time and space, it is possible to effectively decouple optical absorption and scattering and subsequently retrieve the absolute quantities of them with high accuracy.

The Space-enhanced Time Domain (SeTD) method for diffuse optics is proposed under this concept of integrating information of multiple domains. Hereby, the SeTD method resolves the forward modelling and inverse retrieving into three levels: data-level, feature-level, and decision-level. To this sense, the SeTD method turns the primal problem which minimizes the

discrepancy between measurements and forward models, into the dual problem which minimize the correlation of effects originated from absorption and scattering. The generalized *Lagrangian* function is applied on the objective function in spatio-temporal space.

The method purposed was then applied to experiments by combining Continuous-wave modality and time domain modality. The light source, detector, and other components in the experimental setup were selected to achieve the best performance of the single photon detection. The instrumentation was adjusted to realize a TD NIRS system with an SD extension, in which the IRF (instrument response function) was obtained as a narrow and clean pulse shape. Both homogenous phantoms and layered phantoms with very similar optical properties as human brain tissues were investigated by this instrumentation under the concept of time domain, continuous-wave, and SeTD modalities.

In the study on homogenous phantoms, solid resin cylinders were tested as the first demonstration and validation of the proof-of-principle of the SeTD concept. The non-uniqueness of space domain diffuse optics was overcome, and the stability and uncertainty associated with the inverse problem on simultaneously retrieving optical absorption and scattering quantities are improved three times and reduced by half, respectively. A better convergence to the optimal solution was always obtained.

In the study on layered phantoms, 2-layered liquid intralipid phantoms were designed and investigated as the more practical validation of the SeTD concept as for the brain's layered structures. The optical properties can be adjusted in this phantom system. The "deep-scattering neutrality" is summarized in the form of an error norm surface and overcome by the SeTD method. The superior performances on accuracy, reliability, and linearity of the SeTD method compared to other methods were demonstrated. The error for simultaneous retrieval of absolute absorption and scattering coefficients in 2-layered structures were restrained within 5% for absorption and 10% for scattering in a large dynamic range. Several practical problems arisen from single domain approaches such as cross-talk and the result dependency on source-detector separation were to a large extent solved by the SeTD method as well.

The prospect of the work can be elaborated in theory, method, and application fields. The present study only considers the integration of information ingested from time and space domain. In future, the work presented here may pave the path to merge different kinds of data types, such as moments of DTOF with time windows, quantities in different frequency domains with central moments, etc. As a general methodology, the concept shown here could also be applied to another spectrum. Since one of the most outstanding advantages of the method in this thesis is its high accuracy, it may be applied to many scenarios where the application is

sensitive to the error of results, for instance the dynamic monitoring of deep brain hemodynamics and the emergent diagnosis of acute cerebral hypoxia. On the other hand, the method proposed here also has the potential in the future to be applied to the circumstances where the conventional methods cannot obtain reliable results such as in the extreme-low light condition.



# List of Publications

---

---

This dissertation consists of the following papers, which are referred to by their Roman numerals in the text.

**I. Space-enhanced time domain diffuse optics for determination of tissue optical properties in layered structures**

Lin Yang, Heidrun Wabnitz, Thomas Gladytz, Aleh Sudakou, Rainer Macdonald, and Dirk Grosenick

Biomedical Optics Express **11**, 6570-6589 (2020).

**II. Spatially-enhanced time-domain NIRS for accurate determination of tissue optical properties**

Lin Yang, Heidrun Wabnitz, Thomas Gladytz, Rainer Macdonald, and Dirk Grosenick

Optics Express **27**, 26415-26431 (2019).

Other peer-reviewed publications that are not included or reprinted in this dissertation:

**III. Depth selectivity in time-domain fNIRS by analyzing moments and time windows**

Aleh Sudakou, Heidrun Wabnitz, Lin Yang, Davide Contini, Lorenzo Spinelli, Alessandro Torricelli, and Adam Liebert

Proc. SPIE 11639, Optical Tomography and Spectroscopy of Tissue XIV, **116390Q** (2021).

**IV. A multi-laboratory comparison of photon migration instruments and their performances: the BitMap exercise**

Sri Rama Pranav Kumar Lanka, Lin Yang, David Orive-Miguel, Joshua Deepak Veesa, Susanna Tagliabue, Aleh Sudakou, Saeed Samaei, Mario Forcione, Zuzana Kovacsova, Anurag Behera, Thomas Gladytz, Dirk Grosenick, Lionel Hervé, Giuseppe Lo Presti, Lorenzo Cortese, Turgut Durduran, Karolina Bejm, Magdalena Morawiec, Piotr Sawosz, Michal Kacprzak, Anna Gerega, Adam Liebert, Antonio Belli, Ilias Tachtsidis, Frédéric Lange, Gemma Bale, Luca Baratelli, Sylvain Gioux, Alexander Kalyanov, Martin Wolf, Sanathana Konugolu Venkata Sekar, Marta Zanoletti, Ileana Pirovano, Michele Lacerenza, Lina Qiu, Edoardo Ferocino, Giulia Maffeis, Caterina Amendola, Lorenzo Colombo, Mauro Buttafava, Marco Renna, Laura Di Sieno, Rebecca Re, Andrea Farina, Lorenzo Spinelli, Alberto Dalla Mora, Davide Contini, Alessandro

Torricelli, Alberto Tosi, Paola Taroni, Hamid Dehghani, Heidrun Wabnitz, and Antonio Pifferi

Proc. SPIE 11639, Optical Tomography and Spectroscopy of Tissue XIV, **116390F** (2021).

**V. Performance of measurands in time-domain optical brain imaging: depth selectivity versus contrast-to-noise ratio**

Aleh Sudakou, Lin Yang, Heidrun Wabnitz, Stanislaw Wojtkiewicz, and Adam Liebert  
Biomedical Optics Express **11**, 4348-4365 (2020)

**VI. Multi-laboratory efforts for the standardization of performance assessment of diffuse optics instruments – the BitMap Exercise**

Pranav Lanka, Lin Yang, David Orive-Miguel, Joshua Deepak Veesa, Susanna Tagliabue, Aleh Sudakou, Saeed Samaei, Mario Forcione, Zuzana Kovacsova, Anurag Behera, Thomas Gladytz, Dirk Grosenick, Lionel Hervé, Giuseppe LoPresti, Lorenzo Cortese, Turgut Durduran, Karolina Bejm, Magdalena Morawiec, Michał Kacprzak, Piotr Sawosz, Anna Grega, Adam Liebert, Antonio Belli, Ilias Tachtsidis, Frederic Lange, Gemma Bale, Luca Baratelli, Sylvain Gioux, Kalyanov Alexander, Martin Wolf, Sanathana Konugolu Venkata Sekar, Marta Zanoletti, Ileana Pirovano, Michele Lacerenza, Lina Qiu, Edoardo Ferocino, Giulia Maffeis, Caterina Amendola, Lorenzo Colombo, Mauro Buttafava, Marco Renna, Laura Di Sieno, Rebecca Re, Andrea Farina, Lorenzo Spinelli, Alberto Dalla Mora, Davide Contini, Paola Taroni, Alberto Tosi, Alessandro Torricelli, Hamid Dehghani, Heidrun Wabnitz, and Antonio Pifferi  
Biophotonics Congress: Biomedical Optics 2020, **STu1D.6** (2020)

**VII. Spatially-enhanced time-domain NIRS for determination of optical properties in layered structures**

Lin Yang, Pranav Lanka, Heidrun Wabnitz, Rinaldo Cubeddu, Thomas Gladytz, Sanathana Konugolu Venkata Sekar, Dirk Grosenick, Antonio Pifferi, and Rainer Macdonald

Proc. SPIE 11074, Diffuse Optical Spectroscopy and Imaging VII, **110740A** (2019)

**VIII. The BITMAP exercise: a multi-laboratory performance assessment campaign of diffuse optical instrumentation**

Pranav Lanka, Lin Yang, David Orive-Miguel, Joshua Deepak Veesa, Susanna Tagliabue, Aleh Sudakou, Saeed Samaei, Mario Forcione, Zuzana Kovacsova, Anurag

Behera, Lionel Hervé, Turgut Durduran, Adam Liebert, Piotr Sawosz, Antonio Belli, Ilias Tachtsidis, Alberto Dalla Mora, Hamid Dehghani, Heidrun Wabnitz, and Antonio Pifferi

Proc. SPIE 11074, Diffuse Optical Spectroscopy and Imaging VII, **110741A** (2019)

**IX. The BitMap dataset: an open dataset on performance assessment of diffuse optics instruments**

David Orive-Miguel, Pranav Lanka, Lin Yang, Susanna Tagliabue, Aleh Sudakou, Saeed Samaei, Joshua Deepak Veesa, Mario Forcione, Zuzana Kovacsova, Anurag Behera, Lionel Hervé, Turgut Durduran, Adam Liebert, Piotr Sawosz, Antonio Belli, Ilias Tachtsidis, Alberto Dalla Mora, Jérôme Mars, Laurent Condat, Alessandro Torricelli, Hamid Dehghani, Heidrun Wabnitz, and Antonio Pifferi

Proc. SPIE 11074, Diffuse Optical Spectroscopy and Imaging VII, **110741B** (2019)

**X. Digital phantom for time-domain near-infrared spectroscopy of tissue: concept and proof-of-principle experiments**

Heidrun Wabnitz, Lin Yang, Rainer Macdonald, and Jeeseong Hwang

Proc. SPIE 10870, Design and Quality for Biomedical Technologies XII, **108700K** (2019)

**XI. Noise reduction and compression of Monte-Carlo lookup tables by singular value decomposition**

Thomas Gladytz, Heidrun Wabnitz, Lin Yang, and Dirk Grosenick

Proc. SPIE 10870, Design and Quality for Biomedical Technologies XII, **1087005** (2019)

**XII. Spatially-enhanced Data Analysis Method for Time-resolved NIRS to Determine Tissue Optical Properties**

Lin Yang, Heidrun Wabnitz, Dirk Grosenick, Thomas Gladytz, and Rainer Macdonald  
Biophotonics Congress: Biomedical Optics Congress 2018, **JW3A.31** (2018)

**XIII. Correction of an adding-doubling inversion algorithm for the measurement of the optical parameters of turbid media**

Paul Lemaillet, Catherine C. Cooksey, Jeeseong Hwang, Heidrun Wabnitz, Dirk Grosenick, Lin Yang, and David W. Allen

Biomedical Optics Express **9**, 55-71 (2018)

**XIV. Polydimethylsiloxane tissue-mimicking phantoms for quantitative optical medical imaging standards**

Jeeseong Hwang, Hyun-Jin Kim, Paul Lemailet, Heidrun Wabnitz, Dirk Grosenick, Lin Yang, Thomas Gladytz, David McClatchy III, David Allen, Kimberly Briggman, and Brian Pogue

Proc. SPIE 10056, Design and Quality for Biomedical Technologies X, **1005603** (2017)

**XV. Broadband spectral measurements of diffuse optical properties by an integrating sphere instrument at the National Institute of Standards and Technology**

Paul Lemailet, Jeeseong Hwang, Heidrun Wabnitz, Dirk Grosenick, Lin Yang, and David W. Allen

Proc. SPIE 10056, Design and Quality for Biomedical Technologies X, **1005604** (2017)

## Reference

---

---

1. D. Huang, E. Swanson, C. Lin, J. Schuman, W. Stinson, W. Chang, M. Hee, T. Flotte, K. Gregory, C. Puliafito, and al. et, "Optical coherence tomography," *Science* **254**, (1991).
2. M. Xu and L. v. Wang, "Photoacoustic imaging in biomedicine," *Review of Scientific Instruments* **77**, (2006).
3. T. Durduran and A. G. Yodh, "Diffuse correlation spectroscopy for non-invasive, micro-vascular cerebral blood flow measurement," *NeuroImage* **85**, (2014).
4. K. Carlsson, P. E. Danielsson, A. Liljeborg, L. Majlöf, R. Lenz, and N. Åslund, "Three-dimensional microscopy using a confocal laser scanning microscope," *Optics Letters* **10**, (1985).
5. A. H. Hielscher, A. Y. Bluestone, G. S. Abdoulaev, A. D. Klose, J. Lasker, M. Stewart, U. Netz, and J. Beuthan, "Near-Infrared Diffuse Optical Tomography," *Disease Markers* **18**, (2002).
6. B. Chance, Z. Zhuang, C. UnAh, C. Alter, and L. Lipton, "Cognition-activated low-frequency modulation of light absorption in human brain.," *Proceedings of the National Academy of Sciences* **90**, (1993).
7. S. Fantini, B. Frederick, and A. Sassaroli, "Perspective: Prospects of non-invasive sensing of the human brain with diffuse optical imaging," *APL Photonics* **3**, (2018).
8. N. Naseer and K.-S. Hong, "fNIRS-based brain-computer interfaces: a review," *Frontiers in Human Neuroscience* **9**, (2015).
9. S. L. Jacques and B. W. Pogue, "Tutorial on diffuse light transport," *Journal of Biomedical Optics* **13**, (2008).
10. S. R. Arridge, "Optical tomography in medical imaging," *Inverse Problems* **15**, (1999).
11. B. Hallacoglu, A. Sassaroli, and S. Fantini, "Optical Characterization of Two-Layered Turbid Media for Non-Invasive, Absolute Oximetry in Cerebral and Extracerebral Tissue," *PLoS ONE* **8**, (2013).

12. J. Selb, T. M. Ogden, J. Dubb, Q. Fang, and D. A. Boas, "Comparison of a layered slab and an atlas head model for Monte Carlo fitting of time-domain near-infrared spectroscopy data of the adult head," *Journal of Biomedical Optics* **19**, (2014).
13. Y. Hoshi and Y. Yamada, "Overview of diffuse optical tomography and its clinical applications," *Journal of Biomedical Optics* **21**, (2016).
14. D. T. Delpy, M. Cope, P. van der Zee, S. Arridge, S. Wray, and J. Wyatt, "Estimation of optical pathlength through tissue from direct time of flight measurement," *Physics in Medicine and Biology* **33**, (1988).
15. L. Kocsis, P. Herman, and A. Eke, "The modified Beer–Lambert law revisited," *Physics in Medicine and Biology* **51**, (2006).
16. L. C. Henyey and J. L. Greenstein, "Diffuse radiation in the Galaxy," *The Astrophysical Journal* **93**, (1941).
17. M. Bassani, F. Martelli, G. Zaccanti, and D. Contini, "Independence of the diffusion coefficient from absorption: experimental and numerical evidence," *Optics Letters* **22**, (1997).
18. F. Jobsis, "Noninvasive, infrared monitoring of cerebral and myocardial oxygen sufficiency and circulatory parameters," *Science* **198**, (1977).
19. S. L. Jacques, "Optical properties of biological tissues: a review," *Physics in Medicine and Biology* **58**, (2013).
20. W. F. Cheong, S. A. Prahl, and A. J. Welch, "A review of the optical properties of biological tissues," *IEEE Journal of Quantum Electronics* **26**, (1990).
21. F. Scholkmann, S. Kleiser, A. J. Metz, R. Zimmermann, J. Mata Pavia, U. Wolf, and M. Wolf, "A review on continuous wave functional near-infrared spectroscopy and imaging instrumentation and methodology," *NeuroImage* **85**, (2014).
22. A. M. Smith, M. C. Mancini, and S. Nie, "Second window for in vivo imaging," *Nature Nanotechnology* **4**, (2009).

23. L. A. Sordillo, Y. Pu, S. Pratavieira, Y. Budansky, and R. R. Alfano, "Deep optical imaging of tissue using the second and third near-infrared spectral windows," *Journal of Biomedical Optics* **19**, (2014).
24. J. A. Wahr, K. K. Tremper, S. Samra, and D. T. Delpy, "Near-Infrared spectroscopy: Theory and applications," *Journal of Cardiothoracic and Vascular Anesthesia* **10**, (1996).
25. T. Marin and J. Moore, "Understanding Near-Infrared Spectroscopy," *Advances in Neonatal Care* **11**, (2011).
26. M. Ferrari and V. Quaresima, "A brief review on the history of human functional near-infrared spectroscopy (fNIRS) development and fields of application," *NeuroImage* **63**, (2012).
27. F. Gaillard, "Illustration depicting the layers of the scalp and meninges," [https://upload.wikimedia.org/wikipedia/commons/5/55/Layers\\_of\\_the\\_scalp\\_and\\_meninges.png](https://upload.wikimedia.org/wikipedia/commons/5/55/Layers_of_the_scalp_and_meninges.png).
28. A. Jelzow, "In vivo quantification of absorption changes in the human brain by time-domain diffuse near-infrared spectroscopy," *Doctoral Thesis* (2013).
29. S. Fantini, D. Hueber, M. A. Franceschini, E. Gratton, W. Rosenfeld, P. G. Stubblefield, D. Maulik, and M. R. Stankovic, "Non-invasive optical monitoring of the newborn piglet brain using continuous-wave and frequency-domain spectroscopy," *Physics in Medicine and Biology* **44**, (1999).
30. M. Dehaes, P. E. Grant, D. D. Sliva, N. Roche-Labarbe, R. Pienaar, D. A. Boas, M. A. Franceschini, and J. Selb, "Assessment of the frequency-domain multi-distance method to evaluate the brain optical properties: Monte Carlo simulations from neonate to adult," *Biomedical Optics Express* **2**, (2011).
31. A. Farina, A. Torricelli, I. Bargigia, L. Spinelli, R. Cubeddu, F. Foschum, M. Jäger, E. Simon, O. Fugger, A. Kienle, F. Martelli, P. di Ninni, G. Zaccanti, D. Milej, P. Sawosz, M. Kacprzak, A. Liebert, and A. Pifferi, "In-vivo multilaboratory investigation of the optical properties of the human head," *Biomedical Optics Express* **6**, (2015).

32. A. N. Sen, S. P. Gopinath, and C. S. Robertson, "Clinical application of near-infrared spectroscopy in patients with traumatic brain injury: a review of the progress of the field," *Neurophotonics* **3**, (2016).
33. A. Kienle, "Determination of Light Absorption and Scattering in Biological Tissue. Experiments, Modeling and Applications," Habilitation (1999).
34. M. S. Patterson, B. Chance, and B. C. Wilson, "Time resolved reflectance and transmittance for the noninvasive measurement of tissue optical properties," *Applied Optics* **28**, (1989).
35. A. Liemert and A. Kienle, "Explicit solutions of the radiative transport equation in the P<sub>3</sub> approximation," *Medical Physics* **41**, (2014).
36. K. G. Phillips and S. L. Jacques, "Solution of transport equations in layered media with refractive index mismatch using the P<sub>N</sub>-method," *Journal of the Optical Society of America A* **26**, (2009).
37. C. Sandoval and A. D. Kim, "Deriving Kubelka–Munk theory from radiative transport," *Journal of the Optical Society of America A* **31**, (2014).
38. S. A. Prahl, M. J. C. van Gemert, and A. J. Welch, "Determining the optical properties of turbid media by using the adding–doubling method," *Applied Optics* **32**, (1993).
39. A. D. Klose and A. H. Hielscher, "Iterative reconstruction scheme for optical tomography based on the equation of radiative transfer," *Medical Physics* **26**, (1999).
40. L. Wang, S. L. Jacques, and L. Zheng, "MCML—Monte Carlo modeling of light transport in multi-layered tissues," *Computer Methods and Programs in Biomedicine* **47**, (1995).
41. D. A. Boas, J. P. Culver, J. J. Stott, and A. K. Dunn, "Three dimensional Monte Carlo code for photon migration through complex heterogeneous media including the adult human head," *Optics Express* **10**, (2002).
42. Q. Fang, "Mesh-based Monte Carlo method using fast ray-tracing in Plücker coordinates," *Biomedical Optics Express* **1**, (2010).

43. G. S. Abdoulaev, K. Ren, and A. H. Hielscher, "Optical tomography as a PDE-constrained optimization problem," *Inverse Problems* **21**, (2005).
44. S. R. Arridge, M. Schweiger, M. Hiraoka, and D. T. Delpy, "A finite element approach for modeling photon transport in tissue," *Medical Physics* **20**, (1993).
45. S. Srinivasan, B. W. Pogue, C. Carpenter, P. K. Yalavarthy, and K. Paulsen, "A boundary element approach for image-guided near-infrared absorption and scatter estimation," *Medical Physics* **34**, (2007).
46. R. H. Wilson, M. Chandra, J. Scheiman, D. Simeone, B. McKenna, J. Purdy, and M.-A. Mycek, "Optical spectroscopy detects histological hallmarks of pancreatic cancer," *Optics Express* **17**, (2009).
47. J.-M. Tualle, H. L. Nghiem, D. Ettore, R. Sablong, E. Tinet, and S. Avrillier, "Asymptotic behavior and inverse problem in layered scattering media," *Journal of the Optical Society of America A* **21**, (2004).
48. J. C. J. Paasschens, "Solution of the time-dependent Boltzmann equation," *Physical Review E* **56**, (1997).
49. A. Liemert and A. Kienle, "Infinite space Green's function of the time-dependent radiative transfer equation," *Biomedical Optics Express* **3**, (2012).
50. A. Liemert and A. Kienle, "Exact and efficient solution of the radiative transport equation for the semi-infinite medium," *Scientific Reports* **3**, (2013).
51. A. Liemert, D. Reitzle, and A. Kienle, "Analytical solutions of the radiative transport equation for turbid and fluorescent layered media," *Scientific Reports* **7**, (2017).
52. A. Sassaroli, A. Pifferi, D. Contini, A. Torricelli, L. Spinelli, H. Wabnitz, P. di Ninni, G. Zaccanti, and F. Martelli, "Forward solvers for photon migration in the presence of highly and totally absorbing objects embedded inside diffusive media," *Journal of the Optical Society of America A* **31**, (2014).
53. M. Schweiger and S. Arridge, "The Toast++ software suite for forward and inverse modeling in optical tomography," *Journal of Biomedical Optics* **19**, (2014).

54. H. Dehghani, M. E. Eames, P. K. Yalavarthy, S. C. Davis, S. Srinivasan, C. M. Carpenter, B. W. Pogue, and K. D. Paulsen, "Near infrared optical tomography using NIRFAST: Algorithm for numerical model and image reconstruction," *Communications in Numerical Methods in Engineering* **25**, (2009).
55. Q. Fang and D. A. Boas, "Monte Carlo Simulation of Photon Migration in 3D Turbid Media Accelerated by Graphics Processing Units," *Optics Express* **17**, (2009).
56. R. Nossal, J. Kiefer, G. H. Weiss, R. Bonner, H. Taitelbaum, and S. Havlin, "Photon migration in layered media," *Applied Optics* **27**, (1988).
57. S. Havlin and D. Ben-Avraham, "Diffusion in disordered media," *Advances in Physics* **36**, (1987).
58. F. A. Grunbaum, "Diffuse tomography: the isotropic case," *Inverse Problems* **8**, (1992).
59. R. C. Haskell, L. O. Svaasand, T.-T. Tsay, T.-C. Feng, B. J. Tromberg, and M. S. McAdams, "Boundary conditions for the diffusion equation in radiative transfer," *Journal of the Optical Society of America A* **11**, (1994).
60. D. Contini, F. Martelli, and G. Zaccanti, "Photon migration through a turbid slab described by a model based on diffusion approximation I Theory," *Applied Optics* **36**, (1997).
61. A. H. Hielscher, S. L. Jacques, L. Wang, and F. K. Tittel, "The influence of boundary conditions on the accuracy of diffusion theory in time-resolved reflectance spectroscopy of biological tissues," *Physics in Medicine and Biology* **40**, (1995).
62. K. M. Yoo, F. Liu, and R. R. Alfano, "When does the diffusion approximation fail to describe photon transport in random media?," *Physical Review Letters* **64**, (1990).
63. A. Kienle and M. S. Patterson, "Improved solutions of the steady-state and the time-resolved diffusion equations for reflectance from a semi-infinite turbid medium," *Journal of the Optical Society of America A* **14**, (1997).
64. R. K. Wang and Y. A. Wickramasinghe, "Fast algorithm to determine optical properties of a turbid medium from time-resolved measurements," *Applied Optics* **37**, (1998).

65. J. Hadamard, *Lectures on Cauchy's Problem in Linear Partial Differential Equations* (Dover Publications Inc., 1952).
66. S. R. Arridge and J. C. Schotland, "Optical tomography: forward and inverse problems," *Inverse Problems* **25**, (2009).
67. J. J. Duderstadt and W. R. Martin, *Transport Theory* (Wiley, 1976).
68. B. Farina, S. Saponaro, E. Pignoli, S. Tomatis, and R. Marchesini, "Monte Carlo simulation of light fluence in tissue in a cylindrical diffusing fibre geometry," *Physics in Medicine and Biology* **44**, (1999).
69. E. Alerstam, S. Andersson-Engels, and T. Svensson, "White Monte Carlo for time-resolved photon migration," *Journal of Biomedical Optics* **13**, (2008).
70. S. Arridge, P. Maass, O. Öktem, and C.-B. Schönlieb, "Solving inverse problems using data-driven models," *Acta Numerica* **28**, (2019).
71. A. Sassaroli and F. Martelli, "Equivalence of four Monte Carlo methods for photon migration in turbid media," *Journal of the Optical Society of America A* **29**, (2012).
72. L. v. Wang and H.-I. Wu, *Biomedical Optics: Principles and Imaging* (Wiley, 2012).
73. A. Liebert, H. Wabnitz, N. Zolek, and R. Macdonald, "Monte Carlo algorithm for efficient simulation of time-resolved fluorescence in layered turbid media," *Optics Express* **16**, (2008).
74. S. Feng, F.-A. Zeng, and B. Chance, "Photon migration in the presence of a single defect: a perturbation analysis," *Applied Optics* **34**, (1995).
75. P. Sawosz, M. Kacprzak, W. Weigl, A. Borowska-Solonyanko, P. Krajewski, N. Zolek, B. Ciszek, R. Maniewski, and A. Liebert, "Experimental estimation of the photons visiting probability profiles in time-resolved diffuse reflectance measurement," *Physics in Medicine and Biology* **57**, (2012).
76. E. Alerstam, T. Svensson, and S. Andersson-Engels, "Parallel computing with graphics processing units for high-speed Monte Carlo simulation of photon migration," *Journal of Biomedical Optics* **13**, (2008).

77. M. Ferrari, "Progress of near-infrared spectroscopy and topography for brain and muscle clinical applications," *Journal of Biomedical Optics* **12**, (2007).
78. D. J. Davies, Z. Su, M. T. Clancy, S. J. E. Lucas, H. Dehghani, A. Logan, and A. Belli, "Near-Infrared Spectroscopy in the Monitoring of Adult Traumatic Brain Injury: A Review," *Journal of Neurotrauma* **32**, (2015).
79. W. Weigl, D. Milej, D. Janusek, S. Wojtkiewicz, P. Sawosz, M. Kacprzak, A. Gerega, R. Maniewski, and A. Liebert, "Application of optical methods in the monitoring of traumatic brain injury: A review," *Journal of Cerebral Blood Flow & Metabolism* **36**, (2016).
80. J. Gervain, J. Mehler, J. F. Werker, C. A. Nelson, G. Csibra, S. Lloyd-Fox, M. Shukla, and R. N. Aslin, "Near-infrared spectroscopy: A report from the McDonnell infant methodology consortium," *Developmental Cognitive Neuroscience* **1**, (2011).
81. A. Torricelli, D. Contini, A. Pifferi, M. Caffini, R. Re, L. Zucchelli, and L. Spinelli, "Time domain functional NIRS imaging for human brain mapping," *NeuroImage* **85**, (2014).
82. A. Dalla Mora, L. di Sieno, R. Re, A. Pifferi, and D. Contini, "Time-Gated Single-Photon Detection in Time-Domain Diffuse Optics: A Review," *Applied Sciences* **10**, (2020).
83. A. Liebert, H. Wabnitz, D. Grosenick, M. Möller, R. Macdonald, and H. Rinneberg, "Evaluation of optical properties of highly scattering media by moments of distributions of times of flight of photons," *Applied Optics* **42**, (2003).
84. J. B. Fishkin and E. Gratton, "Propagation of photon-density waves in strongly scattering media containing an absorbing semi-infinite plane bounded by a straight edge," *Journal of the Optical Society of America A* **10**, (1993).
85. A. Pifferi, D. Contini, A. D. Mora, A. Farina, L. Spinelli, and A. Torricelli, "New frontiers in time-domain diffuse optics, a review," *Journal of Biomedical Optics* **21**, (2016).
86. F. Martelli, T. Binzoni, A. Pifferi, L. Spinelli, A. Farina, and A. Torricelli, "There's plenty of light at the bottom: statistics of photon penetration depth in random media," *Scientific Reports* **6**, (2016).

87. R. Savo, R. Pierrat, U. Najar, R. Carminati, S. Rotter, and S. Gigan, "Observation of mean path length invariance in light-scattering media," *Science* **358**, (2017).
88. S. R. Arridge and W. R. B. Lionheart, "Nonuniqueness in diffusion-based optical tomography," *Optics Letters* **23**, (1998).
89. A. Dalla Mora, L. di Sieno, A. Behera, P. Taroni, D. Contini, A. Torricelli, and A. Pifferi, "The SiPM revolution in time-domain diffuse optics," *Nuclear Instruments and Methods in Physics Research Section A: Accelerators, Spectrometers, Detectors and Associated Equipment* **978**, (2020).
90. W. Becker, *Advanced Time-Correlated Single Photon Counting Techniques* (Springer, 2005).
91. B. W. Pogue and M. S. Patterson, "Review of tissue simulating phantoms for optical spectroscopy, imaging and dosimetry," *Journal of Biomedical Optics* **11**, (2006).
92. J. Hwang, H.-J. Kim, P. Lemailet, H. Wabnitz, D. Grosenick, L. Yang, T. Gladysz, D. McClatchy, D. Allen, K. Briggman, and B. Pogue, "Polydimethylsiloxane tissue-mimicking phantoms for quantitative optical medical imaging standards," in R. Raghavachari, R. Liang, and T. J. Pfefer, eds. (2017).
93. A. Pifferi, A. Torricelli, A. Bassi, P. Taroni, R. Cubeddu, H. Wabnitz, D. Grosenick, M. Möller, R. Macdonald, J. Swartling, T. Svensson, S. Andersson-Engels, R. L. P. van Veen, H. J. C. M. Sterenborg, J.-M. Tualle, H. L. Nghiem, S. Avrillier, M. Whelan, and H. Stamm, "Performance assessment of photon migration instruments: the MEDPHOT protocol," *Applied Optics* **44**, (2005).
94. H. Wabnitz, D. R. Taubert, M. Mazurenka, O. Steinkellner, A. Jelzow, R. Macdonald, D. Milej, P. Sawosz, M. Kacprzak, A. Liebert, R. Cooper, J. Hebden, A. Pifferi, A. Farina, I. Bargigia, D. Contini, M. Caffini, L. Zucchelli, L. Spinelli, R. Cubeddu, and A. Torricelli, "Performance assessment of time-domain optical brain imagers, part 1: basic instrumental performance protocol," *Journal of Biomedical Optics* **19**, (2014).
95. M. Firbank and D. T. Delpy, "A design for a stable and reproducible phantom for use in near infra-red imaging and spectroscopy," *Physics in Medicine and Biology* **38**, (1993).

96. J. Swartling, J. S. Dam, and S. Andersson-Engels, "Comparison of spatially and temporally resolved diffuse-reflectance measurement systems for determination of biomedical optical properties," *Applied Optics* **42**, (2003).
97. L. Spinelli, F. Martelli, A. Farina, A. Pifferi, A. Torricelli, R. Cubeddu, and G. Zaccanti, "Calibration of scattering and absorption properties of a liquid diffusive medium at NIR wavelengths. Time-resolved method," *Optics Express* **15**, (2007).
98. S. Kleiser, N. Nasser, B. Andresen, G. Greisen, and M. Wolf, "Comparison of tissue oximeters on a liquid phantom with adjustable optical properties," *Biomedical Optics Express* **7**, (2016).
99. L. Spinelli, M. Botwicz, N. Zolek, M. Kacprzak, D. Milej, P. Sawosz, A. Liebert, U. Weigel, T. Durduran, F. Foschum, A. Kienle, F. Baribeau, S. Leclair, J.-P. Bouchard, I. Noiseux, P. Gallant, O. Mermut, A. Farina, A. Pifferi, A. Torricelli, R. Cubeddu, H.-C. Ho, M. Mazurenka, H. Wabnitz, K. Klauenberg, O. Bodnar, C. Elster, M. Bénazech-Lavoué, Y. Bérubé-Lauzière, F. Lesage, D. Khoptyar, A. A. Subash, S. Andersson-Engels, P. di Ninni, F. Martelli, and G. Zaccanti, "Determination of reference values for optical properties of liquid phantoms based on Intralipid and India ink," *Biomedical Optics Express* **5**, (2014).
100. F. F. Jöbsis-vanderVliet, "Discovery of the Near-Infrared Window into the Body and the Early Development of Near-Infrared Spectroscopy," *Journal of Biomedical Optics* **4**, (1999).
101. G. Bale, C. E. Elwell, and I. Tachtsidis, "From Jöbsis to the present day: a review of clinical near-infrared spectroscopy measurements of cerebral cytochrome-c-oxidase," *Journal of Biomedical Optics* **21**, (2016).
102. T. Durduran, R. Choe, W. B. Baker, and A. G. Yodh, "Diffuse optics for tissue monitoring and tomography," *Reports on Progress in Physics* **73**, (2010).
103. J. R. Mourant, J. P. Freyer, A. H. Hielscher, A. A. Eick, D. Shen, and T. M. Johnson, "Mechanisms of light scattering from biological cells relevant to noninvasive optical-tissue diagnostics," *Applied Optics* **37**, (1998).

104. A. El-Hamid El-Desoky, D. T. Delpy, B. R. Davidson, and A. M. Seifalian, "Assessment of hepatic ischaemia reperfusion injury by measuring intracellular tissue oxygenation using near infrared spectroscopy," *Liver* **21**, (2001).
105. M. Ferrari and V. Quaresima, "A brief review on the history of human functional near-infrared spectroscopy (fNIRS) development and fields of application," *NeuroImage* **63**, (2012).
106. A. Torricelli, D. Contini, A. D. Mora, A. Pifferi, R. Re, L. Zucchelli, M. Caffini, A. Farina, and L. Spinelli, "Neurophotonics: Non-invasive optical techniques for monitoring brain functions," *Functional Neurology* **29**, (2014).
107. M. Calderon-Arnulphi, A. Alaraj, and K. v. Slavin, "Near infrared technology in neuroscience: Past, present and future," *Neurological Research* **31**, (2009).
108. D. Grosenick, H. Rinneberg, R. Cubeddu, and P. Taroni, "Review of optical breast imaging and spectroscopy," *Journal of Biomedical Optics* **21**, (2016).
109. C. Lindner, M. Mora, P. Farzam, M. Squarcia, J. Johansson, U. M. Weigel, I. Halperin, F. A. Hanzu, and T. Durduran, "Diffuse optical characterization of the healthy human thyroid tissue and two pathological case studies," *PLoS ONE* **11**, (2016).
110. N. Petitdidier, A. Koenig, R. Gerbelot, H. Gateau, S. Gioux, and P. Jallon, "Contact, high-resolution spatial diffuse reflectance imaging system for skin condition diagnosis," *Journal of Biomedical Optics* **23**, 1 (2018).
111. V. R. Kondepoti, H. M. Heise, and J. Backhaus, "Recent applications of near-infrared spectroscopy in cancer diagnosis and therapy," *Analytical and Bioanalytical Chemistry* **390**, (2008).
112. D. Borycki, O. Kholiqov, and V. J. Srinivasan, "Reflectance-mode interferometric near-infrared spectroscopy quantifies brain absorption, scattering, and blood flow index in vivo," *Optics Letters* **42**, (2017).
113. D. Borycki, O. Kholiqov, and V. J. Srinivasan, "Correlation gating quantifies the optical properties of dynamic media in transmission," *Optics Letters* **43**, (2018).

114. D. Milej, A. Abdalmalak, D. Janusek, M. Diop, A. Liebert, and K. st. Lawrence, "Time-resolved subtraction method for measuring optical properties of turbid media," *Applied Optics* **55**, (2016).
115. D. Milej, A. Abdalmalak, P. McLachlan, M. Diop, A. Liebert, and Keith. st. Lawrence, "Subtraction-based approach for enhancing the depth sensitivity of time-resolved NIRS," *Biomedical Optics Express* **7**, (2016).
116. M. Schweiger and S. R. Arridge, "Application of temporal filters to time resolved data in optical tomography," *Physics in Medicine and Biology* **44**, (1999).
117. A. E. Cerussi, R. Warren, B. Hill, D. Roblyer, A. Leproux, A. F. Durkin, T. D. O'Sullivan, S. Keene, H. Haghany, T. Quang, W. M. Mantulin, and B. J. Tromberg, "Tissue phantoms in multicenter clinical trials for diffuse optical technologies," *Biomedical Optics Express* **3**, (2012).
118. H. Wabnitz and H. Rinneberg, "Imaging in turbid media by photon density waves: spatial resolution and scaling relations," *Applied Optics* **36**, (1997).
119. S. Suzuki, S. Takasaki, T. Ozaki, and Y. Kobayashi, "Tissue oxygenation monitor using NIR spatially resolved spectroscopy," in *Optical Tomography and Spectroscopy of Tissue III* (1999), Vol. 3597.
120. A. Liebert, H. Wabnitz, D. Grosenick, and R. Macdonald, "Fiber dispersion in time domain measurements compromising the accuracy of determination of optical properties of strongly scattering media," *Journal of Biomedical Optics* **8**, (2003).
121. Z. A. Steelman, D. S. Ho, K. K. Chu, and A. Wax, "Light-scattering methods for tissue diagnosis," *Optica* **6**, (2019).
122. D. J. Cuccia, F. Bevilacqua, A. J. Durkin, and B. J. Tromberg, "Modulated imaging: quantitative analysis and tomography of turbid media in the spatial-frequency domain," *Optics Letters* **30**, (2005).
123. D. Lighter, J. Hughes, I. Styles, A. Filer, and H. Dehghani, "Multispectral, non-contact diffuse optical tomography of healthy human finger joints," *Biomedical Optics Express* **9**, (2018).

124. M. Wolf, G. Naulaers, F. van Bel, S. Kleiser, and G. Greisen, "Review: A review of near infrared spectroscopy for term and preterm newborns," *Journal of Near Infrared Spectroscopy* **20**, (2012).
125. B. Hallacoglu, A. Sassaroli, S. Fantini, and A. M. Troen, "Cerebral perfusion and oxygenation are impaired by folate deficiency in rat: Absolute measurements with noninvasive near-infrared spectroscopy," *Journal of Cerebral Blood Flow and Metabolism* **31**, (2011).
126. B. Hallacoglu, "Absolute measurement of cerebral optical coefficients, hemoglobin concentration and oxygen saturation in old and young adults with near-infrared spectroscopy," *Journal of Biomedical Optics* **17**, (2012).
127. F. Martelli, S. del Bianco, L. Spinelli, S. Cavalieri, P. di Ninni, T. Binzoni, A. Jelzow, R. Macdonald, and H. Wabnitz, "Optimal estimation reconstruction of the optical properties of a two-layered tissue phantom from time-resolved single-distance measurements," *Journal of Biomedical Optics* **20**, (2015).
128. A. Kienle, T. Glanzmann, G. Wagnières, and H. van den Bergh, "Investigation of two-layered turbid media with time-resolved reflectance," *Applied Optics* **37**, (1998).
129. M. Shimada, C. Sato, Y. Hoshi, and Y. Yamada, "Estimation of the absorption coefficients of two-layered media by a simple method using spatially and time-resolved reflectances," *Physics in Medicine and Biology* **54**, (2009).
130. L. Yang, H. Wabnitz, T. Gladysz, R. Macdonald, and D. Grosenick, "Spatially-enhanced time-domain NIRS for accurate determination of tissue optical properties," *Optics Express* **27**, (2019).
131. C. Zhu and Q. Liu, "Review of Monte Carlo modeling of light transport in tissues," *Journal of Biomedical Optics* **18**, (2013).
132. P. di Ninni, F. Martelli, and G. Zaccanti, "Intralipid: Towards a diffusive reference standard for optical," *Physics in Medicine and Biology* **56**, (2011).
133. P. di Ninni, F. Martelli, and G. Zaccanti, "The use of India ink in tissue-simulating phantoms," *Optics Express* **18**, (2010).

134. F. Martelli, P. di Ninni, G. Zaccanti, D. Contini, L. Spinelli, A. Torricelli, R. Cubeddu, H. Wabnitz, M. Mazurenka, R. Macdonald, A. Sassaroli, and A. Pifferi, "Phantoms for diffuse optical imaging based on totally absorbing objects, part 2: experimental implementation," *Journal of Biomedical Optics* **19**, (2014).
135. S. del Bianco, F. Martelli, F. Cignini, G. Zaccanti, A. Pifferi, A. Torricelli, A. Bassi, P. Taroni, and R. Cubeddu, "Liquid phantom for investigating light propagation through layered diffusive media," *Optics Express* **12**, (2004).





**Herausgeber:**

Physikalisch-Technische Bundesanstalt  
ISNI: 0000 0001 2186 1887

Presse und Öffentlichkeitsarbeit

Bundesallee 100  
38116 Braunschweig

Telefon: (05 31) 592-93 21  
Telefax: (05 31) 592-92 92  
[www.ptb.de](http://www.ptb.de)

**Vertrieb:**

Fachverlag NW in der  
Carl Schünemann Verlag GmbH

Zweite Schlachtpforte 7  
28195 Bremen

Telefon: (04 21) 369 03-0  
Telefax: (04 21) 369 03-63  
[www.schuenemann-verlag.de](http://www.schuenemann-verlag.de)